A Millimetre Wave Quasi-Optical Spatial Interferometer for Passive Ranging and Direction Finding

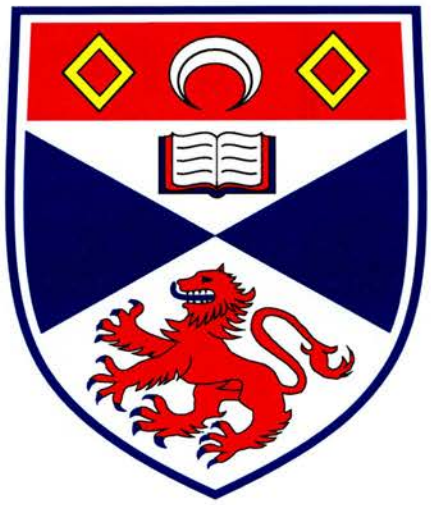

A thesis presented by
Duncan M. Pryde
to the
University of St Andrews
in application for the degree of
Doctor of Philosophy

September 2001

Declarations

(i) I, Duncan M. Pryde, hereby certify that this thesis, which is approximately 27000 words in length, has been written by me, that it is the record of work carried out by me and that it has not been submitted in any previous application for a higher degree.

Duncan M. Pryde

September 2001

(ii) I was admitted as a research student in October 1997 and as a candidate for the degree of Ph.D. in October 1998; the higher study for which this is a record was carried out in the University of St Andrews between 1997 and 2000.

Duncan M. Pryde

September 2001

(iii) I hereby certify that the candidate has fulfilled the conditions of the Resolution and Regulations appropriate for the degree of Ph.D. in the University of St Andrews and that the candidate is qualified to submit this thesis in application for that degree.

Jim C. G. Lesurf

September 2001

In submitting this thesis to the University of St Andrews I understand that I am giving permission for it to be made available for use in accordance with the regulations of the University Library for the time being in force, subject to any copyright vested in the work not being affected thereby. I also understand that the title and abstract will be published, and that a copy of the work may be made and supplied to any *bona fide* library or research worker.

Duncan M. Pryde

September 2001

Acknowledgements

I WOULD first like to thank my supervisor, Jim Lesurf for all his advice and guidance. His help has been invaluable to me. I would also like to extend my gratitude to the other members of the Millimetre Wave Group, past and present, and in particular to Duncan Robertson who has consistently gone beyond the call of duty in providing assistance.

Thanks must also go to the Mechanical Workshop in the Physics Department, and in particular to Andy Barman and George Radley. Thanks too, to the Electronic Workshop.

A special thanks must go to Andy Ray of Intelligent Interfaces, who provided hours of support and programming advice regarding the data acquisition card.

An acknowledgement must be made to the Engineering and Physical Sciences Research Council for providing my funding during the three years.

Finally, I would like to thank my family, and Sally, who have all provided much needed support and encouragement. This is dedicated to you all.

Abstract

PASSIVE RANGING is a technique whereby we can obtain range and direction information on a source without illuminating it as with conventional radar. In this thesis, a system is presented which can perform passive ranging at millimetre wave frequencies using the technique of quasi-optical spatial interferometry.

A system had already been built prior to this work which performed passive ranging by measurement of phase front curvature. The theory of operation of this device was subsequently investigated more thoroughly and equations were derived to describe the expected behaviour. Data taken with this system agreed with the new theory, providing a calibration factor was introduced to correct for small mechanical misalignments within the system. However, to provide greater stability for possible longer term measurements, I have redesigned and rebuilt the receiver to be more rigid and less prone to day to day variations in mechanical alignment.

The new system has been thoroughly tested with a 95GHz source at short ranges (less than 100m), and exhibits much improved stability and accuracy in its agreement with the theory.

Contents

Chapter 3 Introduction to Passive Ranging

Chapter 4 Theory and Experiment I

Chapter 5 Experimental Setup

Chapter 10 A Final Review

Appendix 1 Proofs from Chapter 3

Appendix 2 Program Code

Chapter 1
Introduction

In this chapter I will present the background to the general area of study contained in the rest of this thesis.

1.1 General introduction and overview

Passive ranging is a technique which has grown from, and therefore has much in common with, both conventional radar and also passive direction finding. I will therefore look briefly at both these techniques in this introductory chapter. I will also introduce the technique of interferometry and its particular use for this application.

1.1.1 Outline of the rest of this thesis

In Chapter 2, I will describe some of the background work to the main part of the thesis, while in Chapter 3 I will move onto passive ranging, specifically the system deployed at St Andrews, for which I will provide a theoretical analysis of its operation. In Chapter 4, I compare the analysis with real data and introduce a necessary modification to the theory. Chapter 5 covers a redesign of the system, while in Chapter 6 I justify the approximations made in the theory. Chapter 7 consists of a full analysis of the working system, with results and an assessment of its accuracy. Finally, Chapters 8 and 9 deal with the use of the system in the study of atmospheric turbulence.

1.2 Background to direction finding and ranging

THE PRIMARY interest in range and direction finding has always been military. Passive direction finding was the first type of target location system developed, which was based on radio techniques. Radio detection and ranging (radar) followed some fifteen years later.

The first radar was CW and operated at about 60MHz, using wave-interference to detect the presence of a target. However, CW radars only provided limited positional information. The next step, in the 1930's, was the introduction of pulsed radar, the first of which operated in the frequency range 20 to 30MHz. This presented problems however, in that it required large transmitters and provided low resolution. Also, at low angles of elevation, targets were difficult to detect because energy coming directly from them interfered destructively with that arriving by reflection from the Earth's surface. By moving to smaller wavelengths, these problems could be overcome. The next move was to a metric band (around 200MHz), but the relatively wide beamwidths and the continued presence of ground effects meant systems operating at still higher frequencies were required.

In 1940, this need was met with the invention of the cavity magnetron by Randell and Boot. It was able to produce microwave radiation at frequencies of up to 3GHz, which meant long-range radars could be built which gave high accuracy and resolution in both horizontal and vertical planes.

Further developments, such as the klystron and the microwave travelling wave tube, enabled still higher frequencies to be used, and radar moved to the millimetre wave area of the spectrum. As knowledge of the atmospheric absorption effects with frequency increased (see for example [REED87]), certain frequencies were exploited. Specifically, the millimetre wave window frequencies of 35GHz, 95GHz, 140GHz and 220GHz, where there is lower

clear air attenuation, are used to achieve as long a detection range as possible. Conversely, there are frequency regions corresponding to the absorption of radiation by water and oxygen molecules which lie between these windows at frequencies of 60GHz, 120GHz and 180GHz. Radars and communications have also been developed at these frequencies in order to capitalise on the covertness provided by the high atmospheric absorption.

1.2.1 Radar ranging

I HAVE already mentioned radar as the principal method used in range finding. All radars operate on the principle of illuminating a target by sending out a signal towards it and extracting information from the reflected signal that returns. They can therefore be called active systems as they rely on providing the signal themselves. The first radar had a very simple basic operating principle: it shone pulsed r.f. energy into a volume of sky and then used a set of crossed dipoles to receive the back-scattered pulses from any aircraft within this volume. The range was simply calculated from a precise measurement of the elapsed time, τ, between the transmitted pulse and the echo,

$$R = \frac{c\tau}{2}. \tag{1.1}$$

However, it must be ensured that enough time elapses to allow the return of the transmitted pulse before the next pulse is emitted. Otherwise, some echo signals may arrive after the next pulse has been transmitted, leading to possible ambiguities in the measurement of the range. Such second-time-around echos would lead to the target appearing to be at a much shorter range than it actually was. This gives us the *maximum unambiguous range* [SKOL80], beyond which targets appear as second-time-around echos:

$$R_{unamb} = \frac{c}{2f_p}, \tag{1.2}$$

where f_p is the pulse frequency. R_{unamb} can be thought of as the range to which the first *range cell* extends. Beyond it there are an infinite number of range cells of the same size. If you know which one the echo is coming from, it is possible to accurately determine its range, otherwise the actual range can be given by

$$R_{actual} = R_{measured} + nR_{cell}, \tag{1.3}$$

where n is an integer greater than or equal to zero.

1.2.2 Radar direction finding

ORIGINALLY, RADARS were monostatic (collocated transmitter and receiver), using the same antenna to transmit and receive the signals. In order to gain information on the direction of the target, the radars would perform a conical scan around the mechanical boresight of the antenna [RAMS85]. The variation in the target signal as the beam scans gave a measure of the angular error in the pointing of the dish, which was then fed back to drive the antenna servo to keep the antenna on target. This method required a minimum number of pulses in order to extract the angle error signal, and during the time in which the scan was made there had to be no variation in the amplitude of the echo pulses other than that produced by scanning. Otherwise, if there was any variation in the pulse-to-pulse amplitude not due to the scanning process, there were errors. These could be caused by movement of the target or by scintillation. A new direction finding (DF) technique was developed to combat this problem. It is called monopulse radar, because the angular measurement is made using one pulse instead of many. This is done by using more than one receiver antenna beam simultaneously. The angle of arrival is determined by measuring the relative phase or amplitude of the echo pulse received in each beam. Because the direction finding data is held in the ratio of the two receiver beams, it is not affected by intrapulse variations. This technique proved

instrumental in the development of passive direction finding techniques, as outlined below.

1.3 Passive techniques

UNLIKE RADAR systems which use an active technique, passive alternatives do not send out their own signal. This has an obvious advantage for military applications in that there is nothing to betray one's position to the enemy.

Initially passive direction finding (PDF) techniques were employed in the shortwave frequency range (0.5 - 30MHz). This was because of the fact that most communications were done at these frequencies. However, later direction finding systems were developed in the microwave frequency range, following the development of radar and microwave communications. The transition to microwaves was made relatively easily, since they had a couple of advantages over high frequency radio waves. Microwave wavelengths were smaller and so better resolution could be obtained with smaller antennas. Also, they propagated along line-of-sight paths and not by reflection from the ionosphere as with HF, thus eliminating problems due to multipath propagation.

Passive microwave direction finding grew out of the monopulse radar technique described above. Since it was not necessary to collocate the transmitter and receiver, the separated or bistatic radar was developed, where the radar illuminated the target from one location while the receiver detected the angle of arrival of the return from another. With improvements in the sensitivity of receivers, it became possible to detect signals transmitted by the target itself, such as its own radar, and use these to calculate its direction. Since there was no need for any emissions at the receive point, the technique became known as passive direction finding.

There are two main types of monopulse-based PDF: amplitude and phase sensing. Amplitude sensing is widely used because of its lower cost and complexity, but phase sensing has the advantage of providing greater accuracy.

1.3.1 Amplitude sensing

AMPLITUDE COMPARISON techniques are most widely used in radar warning receiving (RWR) systems, which pick up radar signals from other sources and process these to get a measurement of the direction from which the source is coming. A simple comparative direction finding receiver consists of two dipole antennas arranged orthogonally to produce the crossed figure-of-eight antenna patterns shown in figure 1.1.

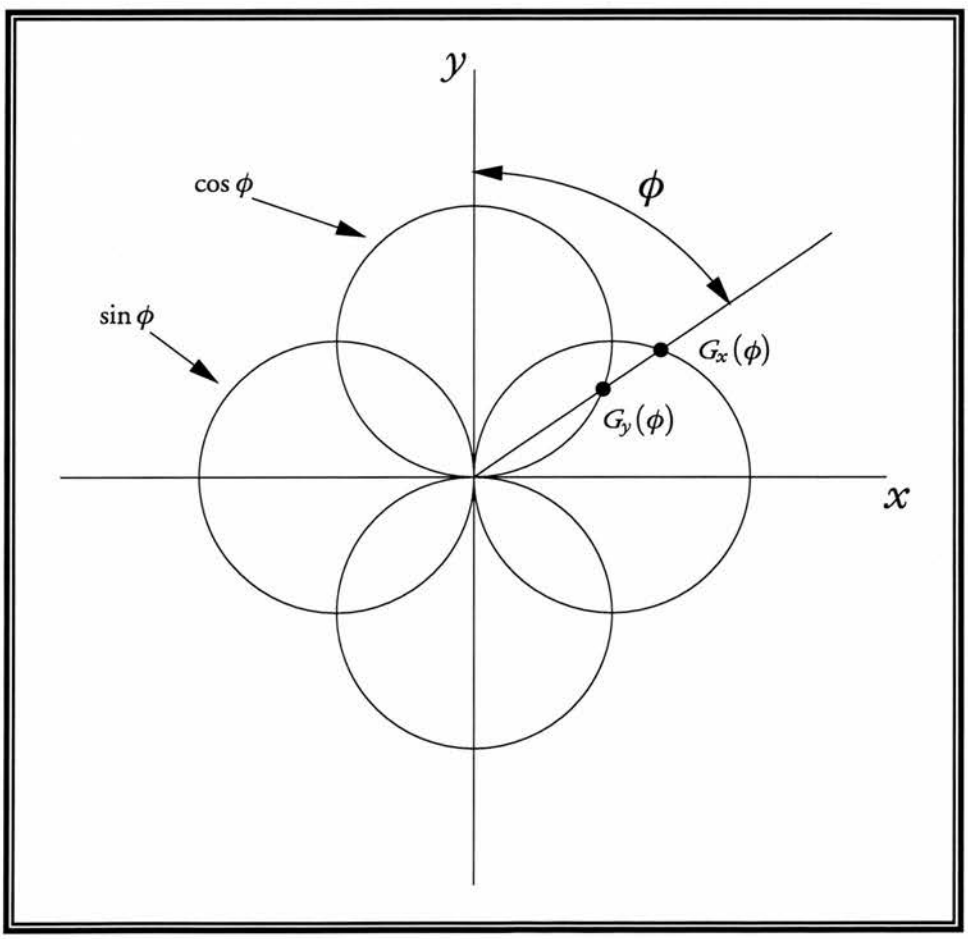

Figure 1.1 Amplitude comparison technique

Bearing information is obtained from the ratio of the amplitudes of the two patterns, with the bearing angle given as [JENK91]

$$\phi = f(G_x(\phi)/G_y(\phi)), \tag{1.4}$$

where $G_x(\phi)$ and $G_y(\phi)$ are the responses of the two antennas. Comparative DF techniques such as this provide instantaneous bearing measurements, and are further useful because the normalisation applied to the signal in the ratio process reduces the effect of signal fluctuations.

Other amplitude sensing arrays use more directional antennas, with overlapping beam patterns to perform essentially the same sort of comparison technique [LIPS87].

It is also possible for amplitude sensing systems to use single antenna elements, usually of the Archimidean spiral type [MA98], although it is more usual to use arrays of antennas.

1.3.2 Phase sensing and interferometry

INTERFEROMETRY HAS been widely used in radio astronomy for some time, in what is called aperture synthesis [THOM86], because of its ability to provide high sensitivity and very good angular resolution. An example of such an interferometer at millimetre wavelengths is described in [WELC77].

The basic geometry of a two-antenna phase comparison system for direction finding is shown below in figure 1.2.

A plane wave arriving at a given angle is received by one antenna earlier than the other because of the difference in path length. This time difference can be

expressed as a phase difference

$$\phi = \frac{2\pi d \sin\theta}{\lambda}, \tag{1.5}$$

where θ is the angle of arrival, d is the antenna separation and λ the wavelength of the incoming radiation. We can define a maximum unambiguous field of view (FOV)

$$\theta_{unamb} = 2 \sin^{-1}\left(\frac{\lambda}{2d}\right), \tag{1.6}$$

which for $\lambda / 2$ antenna spacing will give full 180° coverage.

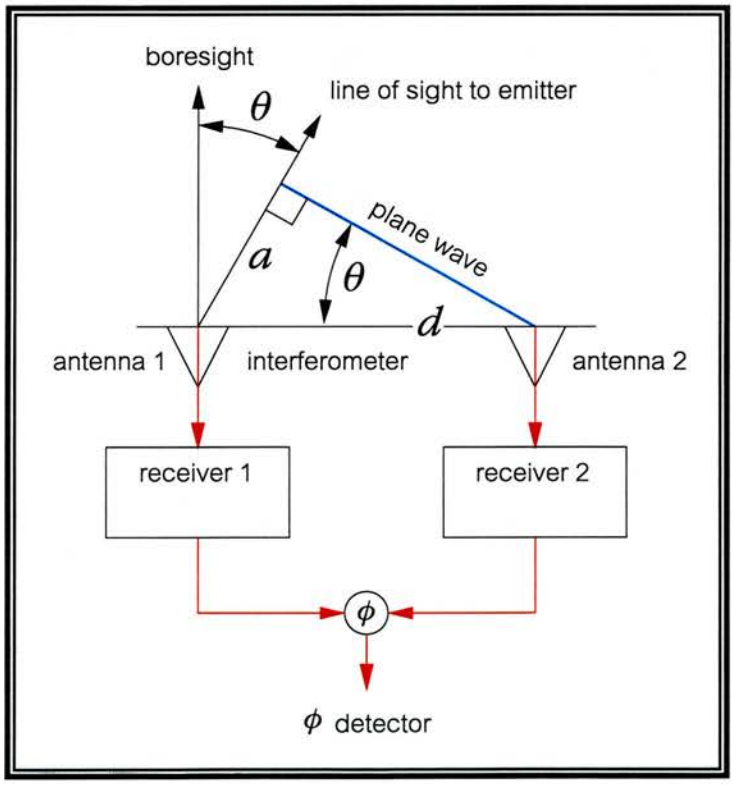

Figure 1.2 A schematic diagram of a phase comparison DF system

At millimetre wave frequencies however, this sort of spacing is impractical, as wavelengths are only of the order of 3-10mm. A larger spacing will give rise to a grating lobe structure, the number of lobes depending on the antenna spacing. For example, antennas placed 30cm apart receiving radiation of 3mm wavelength will give rise to 31 grating lobes, each covering about 5.7° of the field of view. Such a system would therefore be of most practical use up to a couple of degrees either side of boresight.

The advantage of having a larger antenna spacing is that although there is a smaller unambiguous field of view, within this area greater angular resolution can be achieved [BARO82]. This is because there will be a finite error $\delta\phi$ in the measurement of the phase. That this translates to an error in the resolution of the angle of arrival can be seen by differentiating equation (1.5)

$$\frac{\delta\phi}{\delta\theta} = \frac{2\pi d \cos\theta}{\lambda}, \tag{1.7}$$

which can be rearranged to give an expression for the spatial angular error

$$\delta\theta = \frac{\lambda\delta\phi}{2\pi d \cos\theta}. \tag{1.8}$$

From this we can see that angular error decreases with antenna separation and increases with wavelength, so for the best possible resolution we want a large antenna spacing and a small wavelength. Because of the problem that this produces with the unambiguous FOV, interferometers often employ multiple antenna elements with different spacings between them, the smaller spacings to get the approximate unambiguous bearing, and successively larger ones to provide more accuracy.

1.4 Summary

IN THIS chapter I have sought to provide an introduction to the field of target location, using both active and passive techniques. I have singled out interferometry as the highest accuracy method of passive direction finding, and briefly introduced the two port interferometer. A much more detailed analysis will be undertaken in Chapter 3, when I look at the theory of operation of a three port interferometer to measure wavefront curvature.

Chapter 2
Background work

In this chapter I will briefly describe some of the background work I undertook prior to the main investigation covered in the rest of this thesis.

2.1 Characterisation of oscillators

The millimetre wave oscillators used in this work are Gunn diodes in a form of resonant cavity. The Gunn diode is a transferred electron device, typically made from GaAs or InP. It exhibits a region of negative differential resistance, caused by a field-induced transfer of electrons from a high-mobility valley to a low-mobility valley. By placing the device in a suitable circuit and biassing it into the negative differential resistance region, it can be made to oscillate, thus converting a D.C. input into an fr. output.

The Gunn oscillators at St Andrews use a resonant circuit designed by [SMIT90], based on work by [CARL85] and by [HAYD83]. It consists of a vertical coaxial cavity which intersects with a waveguide. The diode package is screwed into the floor of the waveguide directly below the cavity. The circuit is closed with a resonant cap and post, whose length can be varied with a choke attached to an external micrometer. The waveguide is chosen to have a cut-off frequency above that of the fundamental mode, which will therefore oscillate entirely within the cavity. The second harmonic, however, passes down the waveguide and out of the device. The second harmonic is preferred to the

fundamental, as it can be tuned in the region around 94GHz, for which there is low atmospheric attenuation. Also in the set-up there is a moveable backshort which controls the termination of the second harmonic therefore controlling the output power coupling. Since the fundamental is oscillating within the cavity only, moving the backshort does not significantly change the frequency of oscillation as it would in a fundamental mode oscillator.

The nature of the Gunn diodes used in the oscillators built at St Andrews is such that no two finished oscillators have exactly the same performance. It is therefore customary that all oscillators are characterised for their frequency and power output across their full tuning range. It is often found that the performance measure is not what is required, and so either the cap and post, or the diode itself, is replaced and the characterisation process repeated. For this purpose, there are a number of spare cap and post arrangements available in the lab already made. While it is imperative for the performance of the oscillator that the post be of the correct diameter for the particular pin, the cap can potentially be of any diameter or thickness. Usually the requirement in any lab experiment is a decent power output (tens of milliwatts) either at a particular frequency, or over a small range of frequencies. Often, in order to do an experiment over the full band from 75 to 110GHz, it is necessary to use two or more oscillators, each optimised at different frequencies.

Characterising an oscillator is done by measuring the variation of frequency and power with cavity height, or choke position. The bias voltage of the oscillator is generally kept constant, and in the characterisations I did was set at 5V. For each measurement, maximum power is obtained by adjusting the backshort. It is vitally important that the measurements are done in one direction, usually outwards, without going back. This is because of the hysteresis in the tuning of the oscillator, due to mechanical backlash in the choke mechanism. If a value is missed, and needs to be filled in, one must wind the choke all the way back in

before winding it out to the required position. A similar procedure must also be followed when using the characterisation results later on, if the frequencies are to be truly reliable.

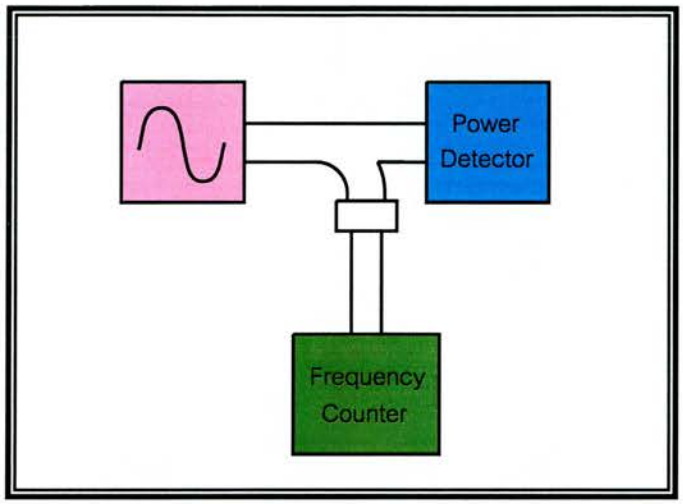

Figure 2.1 Schematic diagram showing the usual setup for making charaterisation measurements

A characteristic setup for making these measurements is shown in figure 2.1. The output from the oscillator is split using a 10dB coupler. To the end of this is attached the power head and meter, usually either an Anritsu ML83A with TC mount MP81B or a Boonton 4220 with the 51047 (4W) head, both of which are suitable for use at W-band frequencies. The frequency is measured by attaching a frequency counter to the 10dB arm of the coupler. The counter used is an EIP 578 Source Locking Microwave Counter.

Initially, a few of the lab oscillators were characterised as they stood. A comparison of two is shown in figure 2.2 on the next page. As can be seen, one (block Z) provides more power at lower frequencies whereas the other (block 2) outputs more power in the upper part of the band. I did in fact use these two oscillators to carry out a full band characterisation of a large panel of dielectric material for Q-Par Angus [PRYD98].

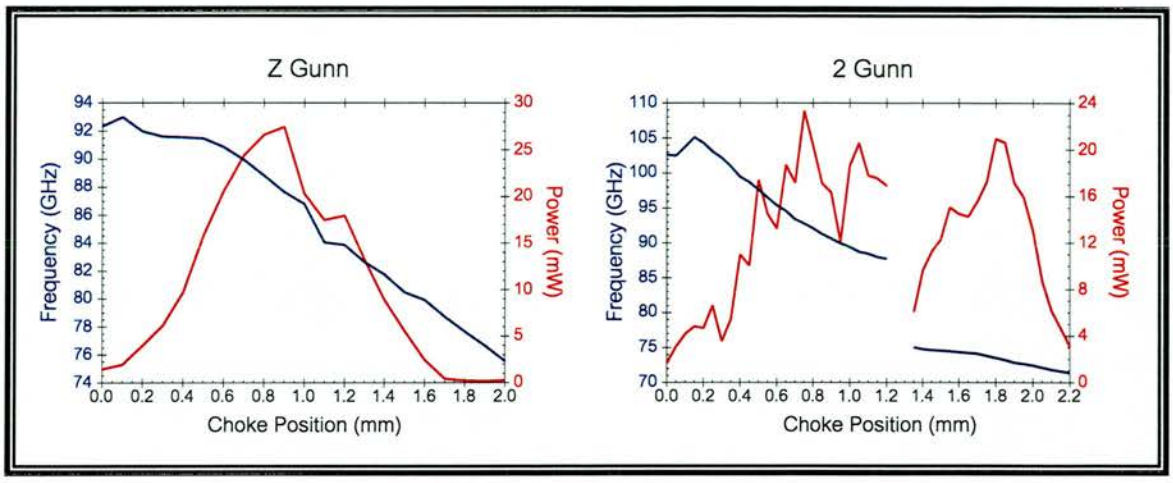

Figure 2.2 Frequency - power characterisations for two oscillators

I also carried out a set of measurements for Milton Harry of Surrey University. These measurements involved using one oscillator block to test various combinations of different Gunn diodes and cap diameters. Four different cap sizes and four different Gunn diodes were analysed in all. A sample of the results is shown below.

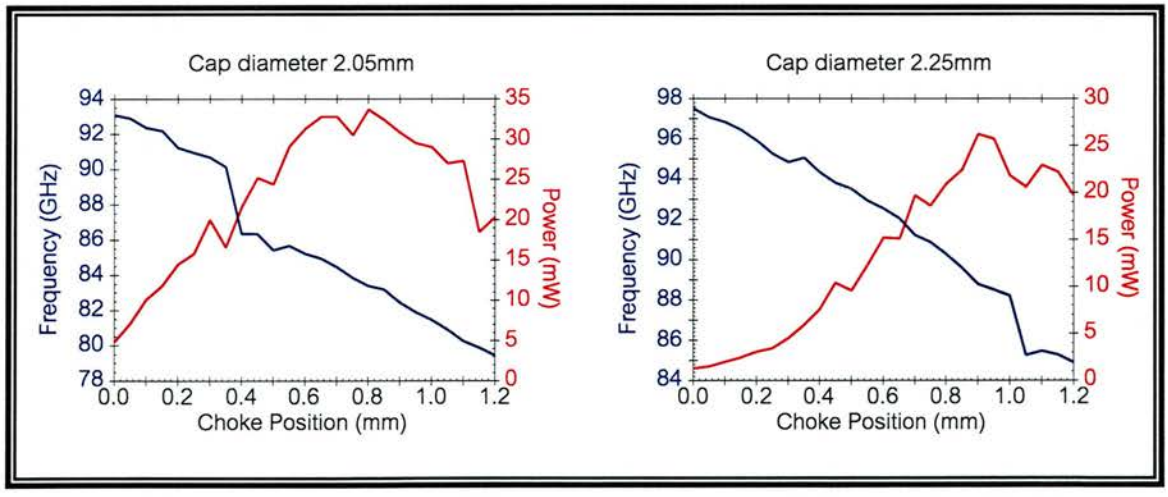

Figure 2.3 Two graphs showing how frequency and power in a Gunn oscillator vary with choke position (or cavity length). As can be seen, the diameter of the cap also has an effect on the frequency and power output

As I mentioned before, all the above measurements were done with a constant bias voltage. I did also carry out some measurements of frequency and power for varying bias, with the choke position held constant. These agreed broadly with the extensive measurements taken by Duncan Robertson and which are discussed at length in his thesis [ROBE94b].

2.2 Schottky diode calibration

Due to competition for lab equipment, the Anritsu and Boonton power meters previously mentioned were sometimes unavailable. I therefore decided to calibrate one of the lab Schottky detectors for use in such circumstances. The experimental setup for doing this was similar to that in figure 2.1 above, but with the Schottky taking the place of the frequency counter. The calibration graph is shown below.

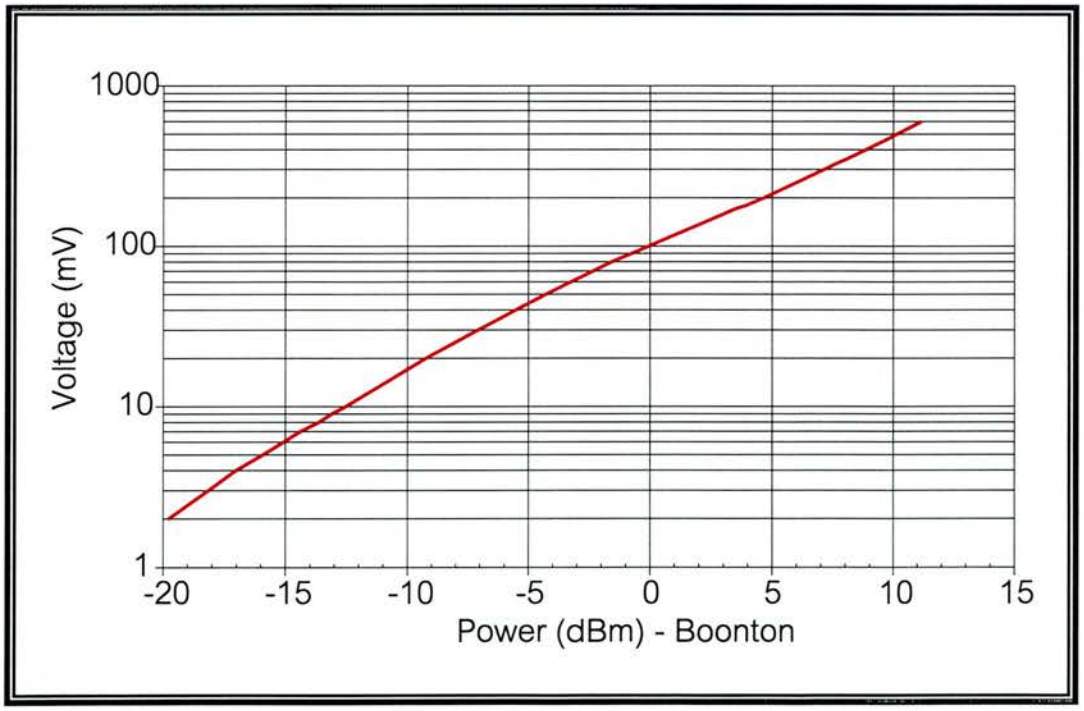

Figure 2.4 Calibration of Schottky power detector SN 7154-03 using Boonton power meter

2.3 Feedhorn antenna pattern measurements

THE SCHOTTKY detector was used to perform a set of measurements to record the antenna pattern of one of the lab corrugated conical feedhorns, the type of feedhorn to be used extensively in later work.

A corrugated feedhorn produces a very good Gaussian beam, with almost all of the power in the fundamental mode [WYLD84]. That this is the case, can be seen from figure 2.4, where I have plotted the received power for angles in the horizontal and vertical planes. The data were obtained by using a turntable to orient the receiver feedhorn in the horizontal plane, rotating the transmitter and receiver 90 degrees to obtain the V-plane data.

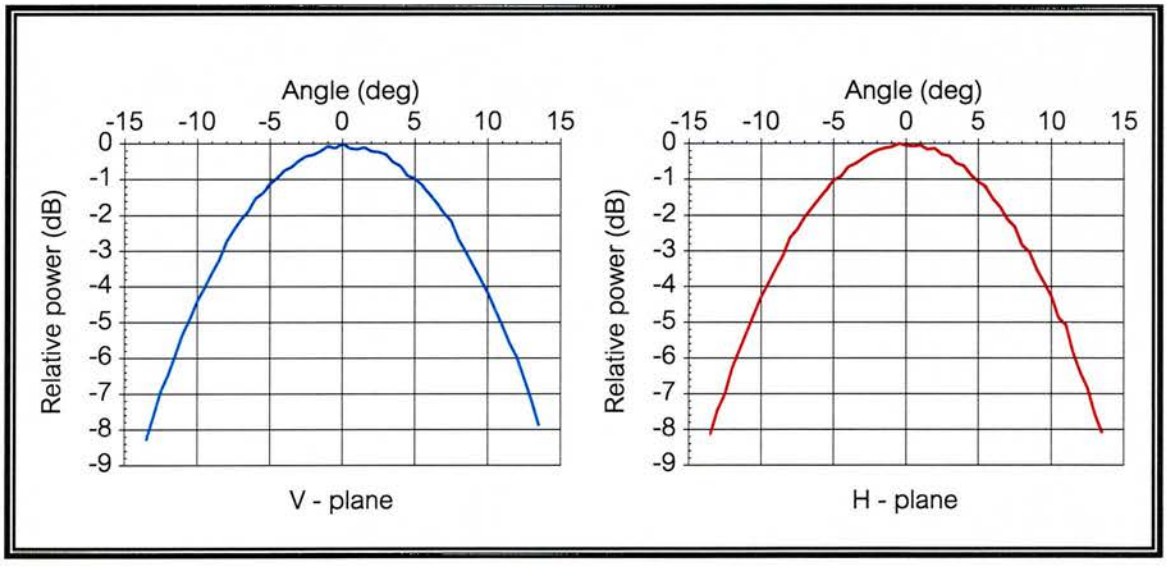

Figure 2.5 Graphs showing normalised far field power with angle for both orientations of a corrugated conical feedhorn of the sort used throughout this work

2.4 Noise generation and correlation techniques

IN ANY real system, the level of noise is a significant factor in receiving and processing a signal. If when designing a data processing routine we can

somehow test the performance of the system under different signal to noise ratios, we can form an accurate picture of its limitations, and hopefully design better processing routines to cope with a wider range of situations.

Originally, the work described in this section was carried out with a view to possibly using the final noise generator circuit in a real situation, to enable us to simulate different signal to noise ratios, and therefore test a given system under different conditions. Although the noise generator was not subsequently used in the rest of this work, it did provide a useful practical introduction to the problem of noise in real situations.

Both Johnson (thermal) noise and shot noise are Gaussian in nature, in other words, their probability density functions can be described by a Normal or Gaussian distribution. Any noise generator should therefore have the same property as far as is possible.

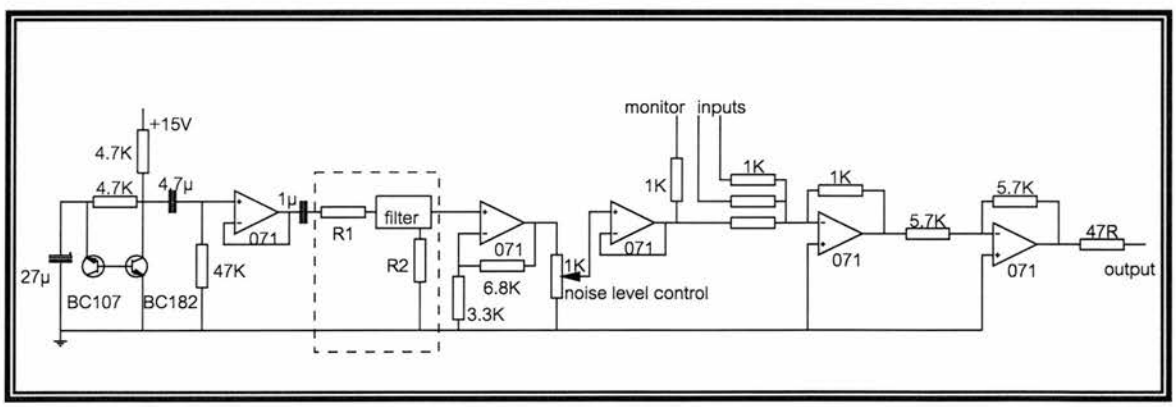

Figure 2.6 A diagram of the noise generating circuit used. The noise produced by the transistor is filter and amplified. A summing amplifier is included to provide a pair of inputs for other signals to which noise is to be added

In order to create as realistic a sample of noise as possible I decided to use an electronic circuit based on a design concept by [MAY96]. The core of the

circuit is a transistor amplifier (a BC182 npn) with a second transistor (a BC107) providing a noise input to the base. Different transistors, even those of the same type, vary greatly in performance, and it was therefore necessary to test several in order to find one with the desired characteristics. A transistor was found which produced a frequency spectrum that had its 3dB point at 240kHz.

Also incorporated in the circuit was a choice of low pass filters, with cut off frequencies at 20kHz, 50kHz and 70kHz. This was to make the generator more versatile by making it able to produce noise with a bandwidth similar to a given signal.

Once a prototype circuit had been fully tested, a printed circuit board was designed and the finished circuit was incorporated into a die-cast box.

Once the circuit was fully working I decided to test the output to verify to my own satisfaction that it was indeed Gaussian noise. The output was sampled using the computer and an Irlam DSP card. I wrote a C routine which sampled the noise at a rate of 333kHz and took 65536 samples in total. I then wrote another routine to form a histogram of these results. This was quite straightforward, as the DSP card converts the voltage of between -5 and +5 to a number between -2047 and +2048. It was therefore a simple matter to associate a frequency with each value. The histogram obtained was then smoothed and graphed using the program EasyPlot on the PC, and thus a Gaussian curve could be fitted to the data. I also wrote a C routine to find the mean and standard deviation of the raw data, and these results agreed very closely with the values for the fitted curve.

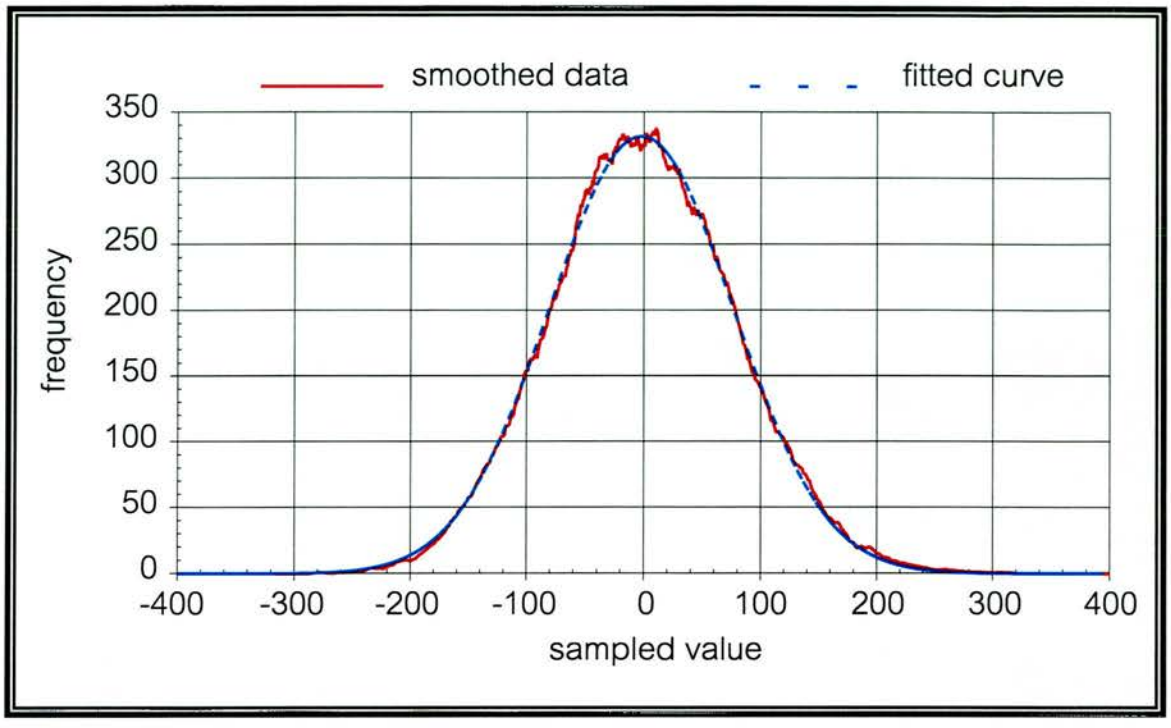

Figure 2.7 Graph showing the distribution associated with the noise generated by the circuit. Also shown is a fitted Gaussian curve

In order to actually separate a signal from the noise travelling with it, we require some method of improving the signal to noise ratio. The technique of correlation, in which a copy of the expected signal is compared with the incoming waveform, is very powerful in this domain. It has the advantages that it is easily adapted to searching for different signals, or for more than one signal in a particular incoming waveform. The comparison can be successfully performed on a computer. It involves sampling the signals at a frequency at least double that of their bandwidth, thus giving two sets of N points in the time domain. The two functions are then compared by directly superimposing them, shifting one either left or right. If the incoming signal is a close copy of the reference signal but lags it in time by some value of t, then the correlation will be large at this t.

Correlation can be performed using various different methods. Bitwise correlation involves simply multiplying each point in one function by the corresponding point in the other and summing together all the results, then repeating this for all N possible offsets. However, the processing time of this method increases with N^2, making it unviable for more than a few thousand data points. Much more useful is the fast Fourier transform method of correlation. In this method, both data sets are FFT'd, the one resulting transform then being multiplied by the complex conjugate of the other. The product is then inverse transformed to obtain the correlation. If the all the points in the inverse transform are divided by N, the correlation will have a peak of between 0 and 1, with 1 indicating a perfect correlation (i.e. two identical data sets). A routine to perform FFT correlation is available as a function, called 'correl' in the book Numerical Recipes in C [PRES88]. This, and the functions it calls, can be incorporated into a C makefile with a 'main' program which provides the data sets for analysis.

Before I built the noise generator I had already done some work with correlations as part of learning programming style, so I decided to conduct a small experiment using the noise-box to demonstrate the possibilities and limitations of using correlation to improve SNR. A random waveform from a sequence generator was used as the signal. The output from the sequence generator is digital, i.e. a random square-wave, but by filtering it, it can be converted into an analogue wave. The sequence used was 65536 bits long and clocked at 87kHz, which roughly corresponded to the frequency at which the DSP card was set to sample. The filter used on the sequence had a sharp cut-off at 20kHz. The noise generator was used with a similar filter, ensuring therefore that the signals were sampled at a frequency four times higher than their bandwidth.

The signal and noise were combined by sending the signal into one of the inputs of the summing amplifier in the noise generator, and the computer was used to take measurements of the signal, the noise and their sum. Samples were taken at different levels of signal and noise, from no signal, full noise power to no noise full signal power. I then wrote a program which calculated the original SNR from the signal and noise, correlated the signal with the signal-plus-noise and calculated a new SNR. This was done for various lengths of data set, from 1024 points to 65536 points.

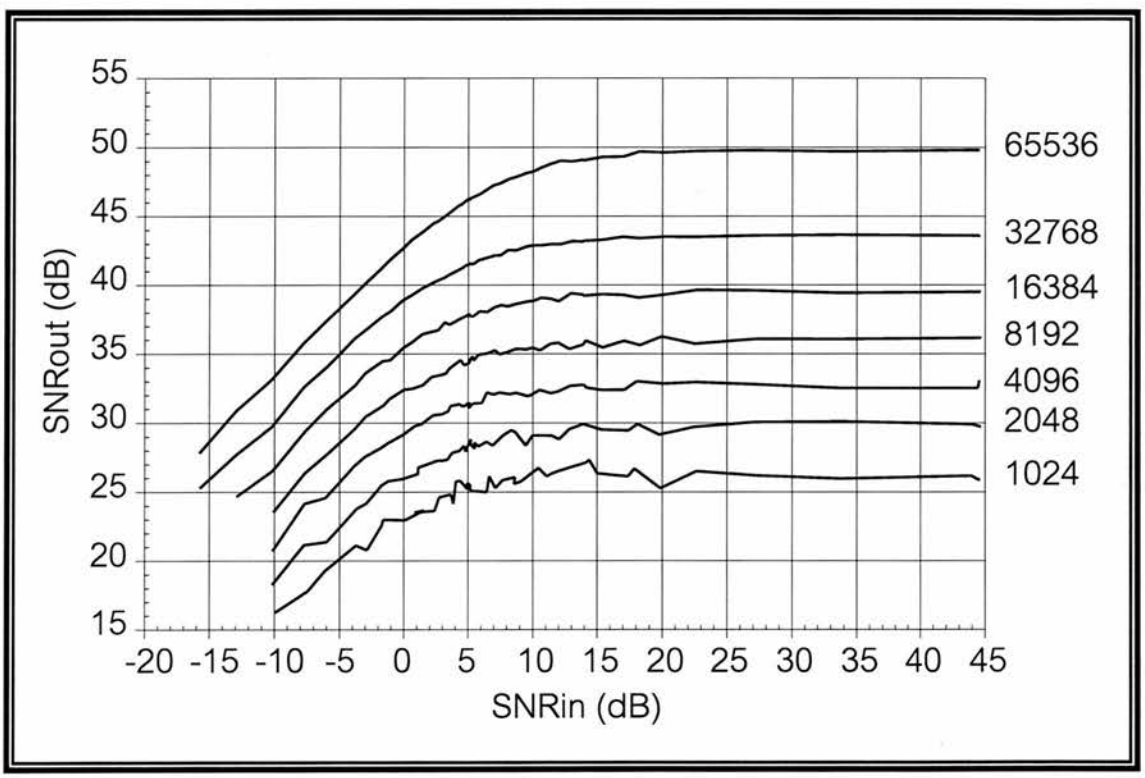

Figure 2.8 This graph shows the signal to noise ratio improvements achieved by correlation using different sizes of data sets. The corresponding sizes are shown on the right

The results show two things. Firstly, the larger the data set we use, the greater the improvement in the SNR after correlation. Secondly, there is a limit to the output SNR, in other words above a certain input SNR, there is no more improvement in the correlation SNR. This is a property of the process of

correlation itself. Even for an auto correlation (in which a signal is correlated with itself) there will be a tiny degree of matching between the signal and itself, even for offsets other than zero, and this creates a residual level of noise in the output of any correlation.

Chapter 3
Introduction to Passive Ranging

In this chapter, I will describe the technique of passive ranging developed at St Andrews, and present a mathematical analysis of the system used.

3.1 Passive ranging

Passive direction finding by interferometric methods uses the comparison of the signal arriving at two antennas in order to calculate bearing. This simple arrangement led us in Chapter 1 to use the approximation of a plane wavefront in our calculations. In reality, however, the wavefront is slightly curved. Two antennas do not allow us to measure this curvature, but with simultaneous measurements at three or more antennas this becomes possible. The curvature of a wavefront is of course directly related to the distance from the source of the wave, therefore by measuring it we can calculate the range of the source, as well as the bearing. If we consider a three antenna system with the source directly on boresight, the signal will arrive at the centre antenna slightly before the two outer ones, the time difference getting smaller with increasing range. By comparing the phase differences between the signal arriving at one antenna and that arriving at the other two, it is possible to calculate the range (and bearing) of the source. This idea is illustrated in figure 3.1 on the next page. It can be clearly seen from the diagram that the time of arrival of a given wavefront (represented by the blue curves) will vary between the three ports.

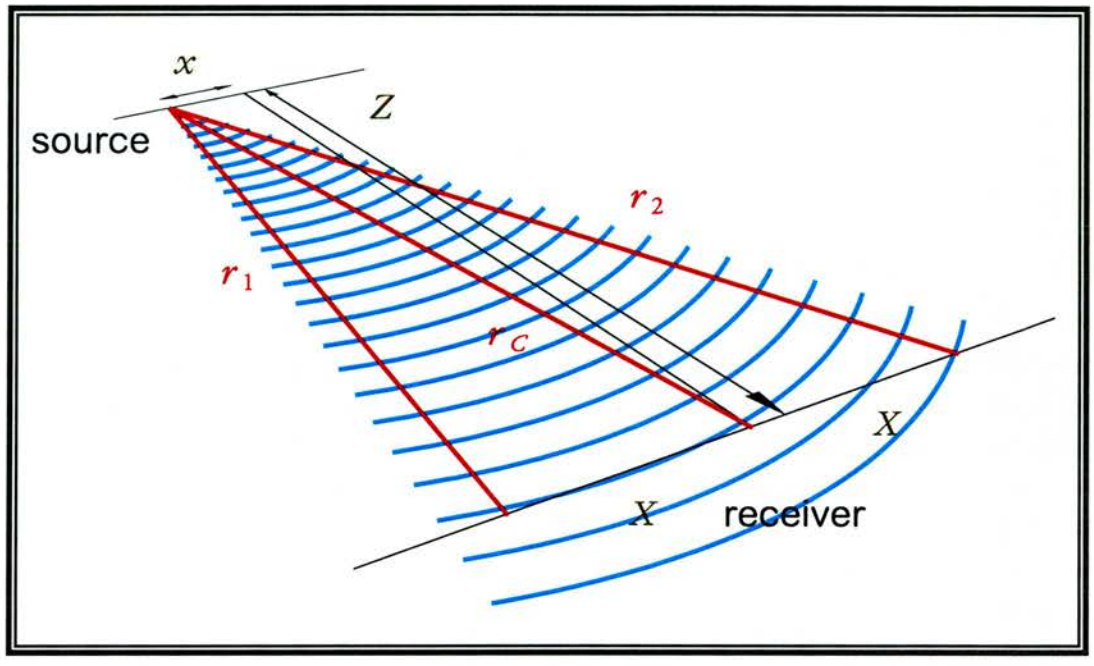

Figure 3.1 The radiation from the source is received at three ports, 1, 2, and C

A system has been developed at St Andrews to perform the necessary interferometry at millimetre wave frequencies, and is described in [LESU94], [ROBE94a], [LESU96], [LESU97a] and [LESU97b]. The system uses three ports and a quasi-optical circuit to extract the necessary phase information. This has the advantage that no downconversion is necessary for the main part of the processing, which can be done at the signal frequency in essentially lossless free space. The main disadvantage of using this approach is that it introduces a restriction on the physical geometry of the system.

3.2 Analysis of theoretical system behaviour

An analysis of the system is best approached from two separate angles. First, in section 3.2.1, we will consider the front of the system, by which I mean the area from the source to the three receiver ports (figure 3.1). Second, in section 3.2.2, we will look at the quasi-optics behind the ports, and how the range and bearing measurements are obtained from this.

3.2.1 Mathematical analysis of front of system

Up to present the geometry has been looked at from the point of view of a source plane and a receiver plane, using an approach similar to that employed by [HANB74]. The source plane is at a distance Z from the receiver plane, with the source at a displacement x from boresight within this plane. The three ports are separated by a distance X.

We can then calculate the absolute phases of the signals arriving at the three ports using simple trigonometry

$$\phi_1 = \frac{2\pi\sqrt{Z^2 + (x - X)^2}}{\lambda} + \phi(t); \tag{3.1}$$

$$\phi_C = \frac{2\pi\sqrt{Z^2 + x^2}}{\lambda} + \phi(t); \tag{3.2}$$

$$\phi_2 = \frac{2\pi\sqrt{Z^2 + (x + X)^2}}{\lambda} + \phi(t), \tag{3.3}$$

and can therefore define the relative phase differences

$$\Theta_1 = \phi_1 - \phi_C; \tag{3.4}$$

$$\Theta_2 = \phi_2 - \phi_C. \tag{3.5}$$

If we assume that $Z^2 \gg (x \pm X)^2$, we can combine the above expressions to give

$$\Theta_1 = \frac{\pi X(X - 2x)}{\lambda Z}; \tag{3.6}$$

$$\Theta_2 = \frac{\pi X(X + 2x)}{\lambda Z}, \tag{3.7}$$

and then rearrange them for the range Z and displacement from boresight x

$$Z = \frac{2\pi X^2}{\lambda(\Theta_1 + \Theta_2)}; \tag{3.8}$$

$$x = \frac{X(\Theta_2 - \Theta_1)}{\lambda(\Theta_1 + \Theta_2)}. \tag{3.9}$$

Therefore if we know the port spacing and can measure the two relative phases, we can obtain values for the range and bearing of the source, providing that we know, or can measure, the radiation wavelength. These expressions only hold, however, when Z is relatively large. In the interest of generality I will therefore derive expressions for the range and bearing that hold down to $Z = 0$.

In order to do this, I will use an analysis based on one used by Dennis in the analysis of acoustic ranging [DENN97], in which we consider the equations for the circle centred on each port. The circles are defined with radii equal to the source-port distances and hence they all intersect at the source. The radii are indicated in figure 3.1 by the red lines marked r_1, r_2, and r_C. By solving the equations of these circles simultaneously, the location of the source can be determined. The location is given by a range r $(= r_C)$ and a bearing φ, measured relative to the position of the centre port.

The range r is defined as the distance from the source to the centre port, and the bearing ϕ is defined as the angle between the source and the normal to the port plane, as measured also from the centre port. We can also define two phase differences, between the field arriving at the centre port and each of the two outer ports

$$\Theta_1 = \frac{|r_1| - |r|}{\lambda\!\!\!^{-}}; \quad \Theta_2 = \frac{|r_2| - |r|}{\lambda\!\!\!^{-}}, \tag{3.10); (3.11}$$

where $\lambda\!\!\!^{-} = \lambda / 2\pi$.

The circle centred on the centre port therefore has radius r, the other two circles being given by the equations

$$(r \sin\phi - X)^2 + (r \cos\phi)^2 = (r + \lambda\Theta_1)^2; \tag{3.12}$$

$$(r \sin\phi + X)^2 + (r \cos\phi)^2 = (r + \lambda\Theta_2)^2. \tag{3.13}$$

By solving them simultaneously (see Appendix 1, section A1.1 for proofs) we can therefore obtain the expressions

$$r = \frac{2X^2 - \lambda^2(\Theta_1^2 + \Theta_2^2)}{2\lambda(\Theta_1 + \Theta_2)}; \tag{3.14}$$

$$\sin\phi = \frac{\lambda\Theta_2(X^2 - \lambda^2\Theta_1^2) - \lambda\Theta_1(X^2 - \lambda^2\Theta_2^2)}{X(2X^2 - \lambda^2(\Theta_1^2 + \Theta_2^2))}. \tag{3.15}$$

We therefore have expressions for the range and bearing in terms of the two phase differences. By examining the behaviour of the quasi-optical circuit we can obtain expressions for the phase differences in terms of the received powers, as described next.

3.2.2 Analysis of the quasi-optical circuit

BEHIND THE ports it is necessary to perform interferometry in order to obtain a measurement of the phase differences between the signal arriving at each port. Various different approaches to this have already been tried, all using quasi-optical circuits. A schematic diagram of the circuit currently being used [LESU97b] is shown in figure 3.2 below. It is built in order that all path lengths from port to detector are essentially equal. This differs from previous versions which included extra components such as Faraday rotators and quarter-wave plates. In the current system a reflective quarter-wave plate is used instead.

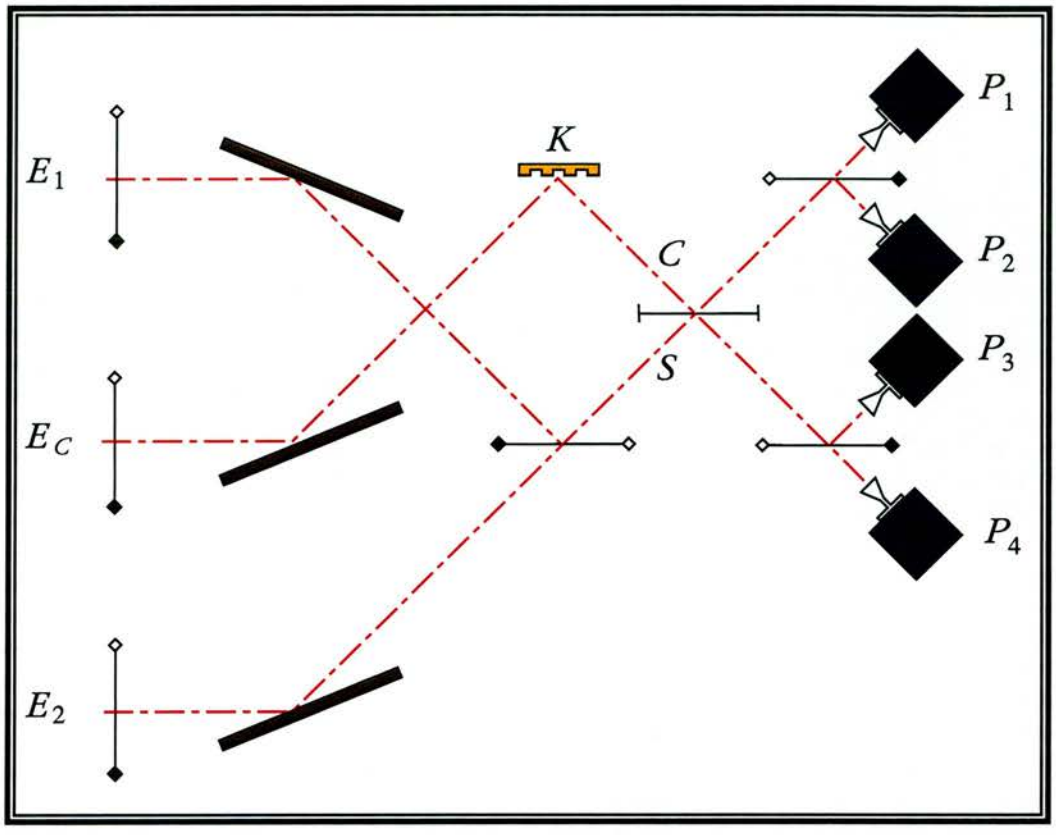

Figure 3.2 The quasi-optical circuit. The field is received at the three ports on the left, and is processed using polarisers and a reflective quarter-wave plate before being detected by the four radiometers on the right.

The reflective quarter wave plate is a plane mirror which has been milled with a regular array of closely spaced vertical grooves, the dimensions of which have been chosen carefully to provide the desired quarter wave delay in one polarisation direction. The principle of operation is fairly simple, provided that we consider only the orientation in which the grooves of the quarter wave plate are perpendicular to the plane containing the incidence and reflection beams. An incident *E*-field component parallel to the grooves will set up a surface current at the tops of these grooves and will therefore be reflected as if from a plane mirror. Conversely, an incident *E*-field component perpendicular to the grooves will be unable to set up such a current and will therefore propagate a field into the grooves as if into an array of rectangular waveguides. This field

will move perpendicular to the surface, and will therefore suffer no sideways displacement relative to the other field component. If we arrange for the grooves to be no wider than a quarter wavelength, and about an eighth of a wavelength deep, we ensure that only the perpendicular component will be delayed, and that this delay will be of a quarter cycle.

The quasi-optical circuit takes the signal in at three equally spaced ports, sums together the signal from the two outer ports and compares that with the signal from the centre port. The reflective quarter-wave plate retards the horizontal polarisation of the centre port signal with respect to the vertical polarisation. The nature of the source being used, and the detector setup, will be described in detail in Chapter 5.

To describe a quasi optical circuit we use the following letters to stand for the various components: V is a polariser with vertical wires, H is a polariser with horizontal wires, P and N are polarisers with the wires at +45° and -45° respectively. These letters are followed by a subscript $_R$ or $_T$ to indicate whether it is transmitting or reflecting. The other symbols used here are M for a mirror and K for a reflective quarter wave plate. Using these conventions, the field arriving at the four power detectors can be expressed in the following way

$$O_1 = N_T H_R C + N_T H_T S; \tag{3.16}$$
$$O_2 = N_R H_R C + N_R H_T S; \tag{3.17}$$
$$O_3 = P_R H_T C + P_R H_R S; \tag{3.18}$$
$$O_4 = P_T H_T C + P_T H_R S; \tag{3.19}$$

where

$$C = KMN_T E_C; \tag{3.20}$$
$$S = P_T M N_T E_2 + N_R M N_T E_1. \tag{3.21}$$

Using the modified Jones matrices [LESU90]

$$M = \begin{pmatrix} -1 & 0 \\ 0 & 1 \end{pmatrix};$$

$$H_R = \begin{pmatrix} 0 & 0 \\ 0 & 1 \end{pmatrix}; \quad H_T = \begin{pmatrix} 1 & 0 \\ 0 & 0 \end{pmatrix};$$

$$P_R = \frac{1}{2}\begin{pmatrix} -1 & -1 \\ 1 & 1 \end{pmatrix}; \quad P_T = \frac{1}{2}\begin{pmatrix} 1 & -1 \\ -1 & 1 \end{pmatrix};$$

$$N_R = \frac{1}{2}\begin{pmatrix} -1 & 1 \\ -1 & 1 \end{pmatrix}; \quad N_T = \frac{1}{2}\begin{pmatrix} 1 & 1 \\ 1 & 1 \end{pmatrix};$$

$$K = \begin{pmatrix} -1 & 0 \\ 0 & -i \end{pmatrix},$$

the four equations (3.16) to (3.19) can be rewritten as (see Appendix 1, section A1.2)

$$O_1 = \frac{1}{4}\begin{pmatrix} 1 & 1 \\ 1 & 1 \end{pmatrix}[E_1 - E_2 - iE_C]; \tag{3.22}$$

$$O_2 = \frac{1}{4}\begin{pmatrix} 1 & 1 \\ 1 & 1 \end{pmatrix}[E_2 - E_1 - iE_C]; \tag{3.23}$$

$$O_3 = \frac{1}{4}\begin{pmatrix} -1 & -1 \\ 1 & 1 \end{pmatrix}[E_1 + E_2 + E_C]; \tag{3.24}$$

$$O_4 = \frac{1}{4}\begin{pmatrix} -1 & -1 \\ 1 & 1 \end{pmatrix}[E_1 + E_2 - E_C]. \tag{3.25}$$

The three fields can be expressed as

$$E_C = \frac{E_0}{\sqrt{2}r_C} \exp\left\{-\left(\frac{\varphi_C}{\theta_0}\right)^2\right\}\begin{pmatrix} 1 \\ 1 \end{pmatrix}; \tag{3.26}$$

$$E_1 = \frac{E_0}{\sqrt{2}r_1} \exp\left\{-\left(\frac{\varphi_1}{\theta_0}\right)^2 - i\Theta_1\right\}\begin{pmatrix} 1 \\ 1 \end{pmatrix}; \tag{3.27}$$

$$E_2 = \frac{E_0}{\sqrt{2}r_2} \exp\left\{-\left(\frac{\varphi_2}{\theta_0}\right)^2 - i\Theta_2\right\}\begin{pmatrix} 1 \\ 1 \end{pmatrix}, \tag{3.28}$$

where θ_0 is the beam divergence angle, φ_C, φ_1, and φ_2 are the bearings from ports C, 1, and 2, and the signal is assumed to be polarised at 45°. E_0 is given by [LESU96]

$$E_0 = \frac{\omega_0}{2 \times 10^{\frac{\alpha}{104}}} \sqrt{\pi P_T G_T}, \tag{3.29}$$

where ω_0 is the beam waist, and α is the absorptivity of the air measured in decibels per kilometre (all other linear dimensions being in metres). P_T and G_T are respectively the power and the gain of the transmitter.

By combining equations (3.22) to (3.25) with (3.26) to (3.28), we obtain

$$O_1 = \frac{E_0}{2\sqrt{2}}\left[\frac{\exp\left\{-\left(\frac{\varphi_1}{\theta_0}\right)^2 - i\Theta_1\right\}}{r_1} - \frac{\exp\left\{-\left(\frac{\varphi_2}{\theta_0}\right)^2 - i\Theta_2\right\}}{r_2} - \frac{i\exp\left\{-\left(\frac{\varphi_C}{\theta_0}\right)^2\right\}}{r_C}\right]\begin{pmatrix}1\\1\end{pmatrix}; \tag{3.30}$$

$$O_2 = \frac{E_0}{2\sqrt{2}}\left[\frac{\exp\left\{-\left(\frac{\varphi_2}{\theta_0}\right)^2 - i\Theta_1\right\}}{r_2} - \frac{\exp\left\{-\left(\frac{\varphi_1}{\theta_0}\right)^2 - i\Theta_2\right\}}{r_1} - \frac{i\exp\left\{-\left(\frac{\varphi_C}{\theta_0}\right)^2\right\}}{r_C}\right]\begin{pmatrix}1\\1\end{pmatrix}; \tag{3.31}$$

$$O_3 = \frac{E_0}{2\sqrt{2}}\left[\frac{\exp\left\{-\left(\frac{\varphi_1}{\theta_0}\right)^2 - i\Theta_1\right\}}{r_1} + \frac{\exp\left\{-\left(\frac{\varphi_2}{\theta_0}\right)^2 - i\Theta_2\right\}}{r_2} + \frac{\exp\left\{-\left(\frac{\varphi_C}{\theta_0}\right)^2\right\}}{r_C}\right]\begin{pmatrix}1\\1\end{pmatrix}; \tag{3.32}$$

$$O_4 = \frac{E_0}{2\sqrt{2}}\left[\frac{\exp\left\{-\left(\frac{\varphi_1}{\theta_0}\right)^2 - i\Theta_1\right\}}{r_1} + \frac{\exp\left\{-\left(\frac{\varphi_2}{\theta_0}\right)^2 - i\Theta_2\right\}}{r_2} - \frac{\exp\left\{-\left(\frac{\varphi_C}{\theta_0}\right)^2\right\}}{r_C}\right]\begin{pmatrix}1\\1\end{pmatrix}. \tag{3.33}$$

At this point it is useful to make a small approximation. The above equations for the fields are entirely accurate, as they take into account the different positions of the three ports. This is indicated by the different r and φ for each port. The source will, in reality, be in a slightly different place in the beam pattern of each antenna, and therefore each antenna will receive a slightly different power. However, to continue to insist upon this full level of accuracy in the analysis that follows would result in a complicated set of equations requiring a numerical solution. In any case, it is the phases rather than the

powers that are of interest in this analysis. I therefore make the assumption that all ports receive equal powers, and consequently that the bearing and range for the centre port apply to ports 1 and 2. In other words we can say that $\varphi_1 \cong \varphi_2 \cong \varphi_C \cong \varphi$ and that $r_1 \cong r_2 \cong r_C \cong r$. The validity of this assumption is discussed in detail in Chapter 6.

By rewriting equations (3.30) to (3.33) including the new assumptions, we then obtain

$$O_1 = \frac{E_0}{2\sqrt{2}r} \exp\left\{-\left(\frac{\varphi}{\theta_0}\right)^2\right\}\left[\exp\{-i\Theta_1\} - \exp\{-i\Theta_2\} - i\right]\begin{pmatrix}1\\1\end{pmatrix}; \quad (3.34)$$

$$O_2 = \frac{E_0}{2\sqrt{2}r} \exp\left\{-\left(\frac{\varphi}{\theta_0}\right)^2\right\}\left[\exp\{-i\Theta_2\} - \exp\{-i\Theta_1\} - i\right]\begin{pmatrix}1\\1\end{pmatrix}; \quad (3.35)$$

$$O_3 = \frac{E_0}{2\sqrt{2}r} \exp\left\{-\left(\frac{\varphi}{\theta_0}\right)^2\right\}\left[\exp\{-i\Theta_1\} + \exp\{-i\Theta_2\} + 1\right]\begin{pmatrix}-1\\1\end{pmatrix}; \quad (3.36)$$

$$O_4 = \frac{E_0}{2\sqrt{2}r} \exp\left\{-\left(\frac{\varphi}{\theta_0}\right)^2\right\}\left[\exp\{-i\Theta_1\} + \exp\{-i\Theta_2\} - 1\right]\begin{pmatrix}-1\\1\end{pmatrix}, \quad (3.37)$$

where φ and r are the bearing and range with respect to the centre port, but which have been also assumed valid for ports 1 and 2. If we then mod-square and add the horizontal and vertical components and simplify using Euler's equation ($e^{i\theta} = \cos\theta + i\sin\theta$), the powers at the four receivers can be obtained.

$$P_1 = \frac{P_0}{4r^2} \exp\left\{-2\left(\frac{\varphi}{\theta_0}\right)^2\right\}\left[3 + 2\sin\Theta_1 - 2\sin\Theta_2 - 2\cos\Theta_1\cos\Theta_2 - 2\sin\Theta_1\sin\Theta_2\right]; \quad (3.38)$$

$$P_2 = \frac{P_0}{4r^2} \exp\left\{-2\left(\frac{\varphi}{\theta_0}\right)^2\right\}\left[3 - 2\sin\Theta_1 + 2\sin\Theta_2 - 2\cos\Theta_1\cos\Theta_2 - 2\sin\Theta_1\sin\Theta_2\right]; \quad (3.39)$$

$$P_3 = \frac{P_0}{4r^2} \exp\left\{-2\left(\frac{\varphi}{\theta_0}\right)^2\right\}\left[3 + 2\cos\Theta_1 + 2\cos\Theta_2 + 2\cos\Theta_1\cos\Theta_2 + 2\sin\Theta_1\sin\Theta_2\right]; \quad (3.40)$$

$$P_4 = \frac{P_0}{4r^2} \exp\left\{-2\left(\frac{\varphi}{\theta_0}\right)^2\right\}\left[3 - 2\cos\Theta_1 - 2\cos\Theta_2 + 2\cos\Theta_1\cos\Theta_2 + 2\sin\Theta_1\sin\Theta_2\right]. \quad (3.41)$$

Rearranging these for Θ_1 and Θ_2 we obtain (see Appendix 1, section A1.3)

$$\Theta_1 + \Theta_2 = 2\cos^{-1}\left(\frac{3\sqrt{(P_1 - P_2)^2 + (P_3 - P_4)^2}}{2(P_1 + P_2 + P_3 + P_4)}\right); \tag{3.42}$$

$$\Theta_2 - \Theta_1 = 2\tan^{-1}\left(\frac{P_1 - P_2}{P_3 - P_4}\right), \tag{3.43}$$

which gives

$$\Theta_1 = \cos^{-1}\left(\frac{3\sqrt{(P_1 - P_2)^2 + (P_3 - P_4)^2}}{2(P_1 + P_2 + P_3 + P_4)}\right) - \tan^{-1}\left(\frac{P_1 - P_2}{P_3 - P_4}\right); \tag{3.44}$$

$$\Theta_2 = \cos^{-1}\left(\frac{3\sqrt{(P_1 - P_2)^2 + (P_3 - P_4)^2}}{2(P_1 + P_2 + P_3 + P_4)}\right) + \tan^{-1}\left(\frac{P_1 - P_2}{P_3 - P_4}\right). \tag{3.45}$$

The values for the relative phases obtained from these last two equations can be substituted into equations (3.14) and (3.15) in the previous section, so that a range and bearing may be obtained from the values of the four powers reaching the detectors.

3.3 Summary

In this chapter, formulas have been derived which should describe fairly accurately the behaviour of the quasi-optical system being used. In doing this though, certain assumptions have been made. As I pointed out, it has been assumed that the powers received by each antenna are equal, because it is the powers received at the detectors, after the field has passed through the quasi-optics, which is important. I would not expect this assumption to affect the usefulness of the derived equations in describing the behaviour of the system. I will however examine this issue more closely in Chapter 6.

The second assumption I have made is that all path lengths in the system are equal. In reality, it is doubtful that this is the case, as it is difficult to ensure that a system is built to the necessary accuracy. Given that we are dealing with a wavelength of about 3mm, a small offset of one or more of the circuit elements from their ideal position may be enough to produce a result which does not agree with the theory. This issue is discussed in the next chapter.

Chapter 4
Theory and Experiment I

In this chapter I will present an analysis of data obtained prior to my involvement in this project. I will show that it is compatible with the theory described in the previous chapter, providing we introduce a small correcting factor, or 'phase offset' into the equations. I will also discuss other implications of the analysis, with particular emphasis on possible improvements that could be made in the construction of the system.

4.1 Origin of data

The experimental data I have used are ones obtained by Lesurf and Robertson [LESU97] in the period from June to September 1997. The data had been saved as sets of values for P_1 to P_4, from which equations for range and bearing had been derived empirically for demonstration purposes. The data had been saved as sets of power values which had been calculated as an average of about a third of a second's worth of raw power data sampled at 41kHz. More information on the data capture method, and on the rest of the experimental apparatus used, is contained in Chapter 5. It is worth mentioning though that the port spacing of the instrument used in these experiments was 0.396m, or double the spacing I used in my final design. I will discuss the related issues later in this chapter. A photograph of the original system is shown in figure 4.1 on the next page.

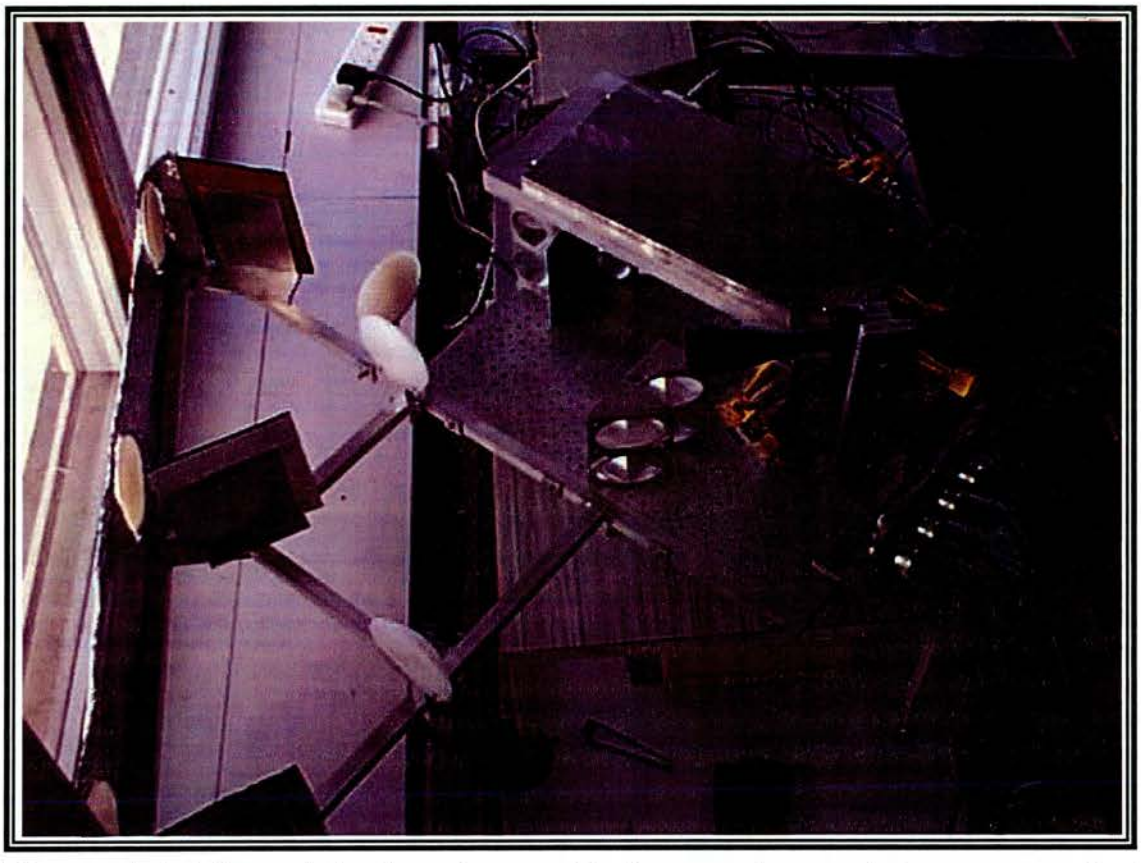

Figure 4.1 The original system, with the receiver antennas mounted on an aluminium frame, and the rest of the quasi-optical circuit on the baseplate visible to the right

The data had been taken by moving a source to a given range and taking a set of measurements. The range at each position was established with the use of a laser range-finder. The ranges involved were from a couple of hundred metres to about two kilometres. It was hoped that the range calculated using equations (3.44), (3.45), (3.14) and (3.15) would agree with the figures obtained from the laser range-finder.

4.2 Analysis of data

INITIALLY, THERE was no agreement at all between the theory outlined in the last chapter and the results previously obtained. The calculated range would fall when the real range rose or would give negative values. It was obvious

therefore that the model would require some modification in order to make the two agree.

At the end of the previous chapter I mentioned that no allowance had been made for the presence of inequalities in the path lengths in the system. However, it was clear from looking at the real data that an adjustment to the theory would be needed to take these path length differences into account. The adjustment I made consists of adding a small constant phase offset to each of the two phase differences Θ_1 and Θ_2 as follows. They are first calculated from the powers using equations (3.44) and (3.45). The offset is then added and the resulting modified phase differences are used in equations (3.14) and (3.15) to calculate the range and bearing. The modified phase differences Θ_1' and Θ_2' can be expressed as

$$\Theta_1' = \Theta_1 + \Delta\Theta; \tag{4.1}$$

$$\Theta_2' = \Theta_2 + \Delta\Theta, \tag{4.2}$$

where $\Delta\Theta$ is the constant offset term. The offset corresponds to a physical difference in path length $\Delta l = \lambda\Delta\Theta$ between the field passing through the centre port and the fields passing through the side ports.

It will have been noted that only one phase offset term is required, despite there being two phase differences. The reasoning behind this comes from the idea that any path length differences within the quasi-optics can be thought of as forwards or backwards displacements of the ports at the front of the system. Boresight is then defined as the direction perpendicular to the line passing through the outer ports, leaving the centre port in front of or behind this line by the distance Δl. In fact, the experimental method for finding boresight assumes equal path lengths from the detectors to each of the two outer ports, resulting in the described offset for the centre port only.

4.2.1 Results of analysis

In this section I present three graphs in which I compare the adjusted theory with three sets of experimental data. The comparison was carried out as follows. I had written a computer program to calculate range and bearing from powers and tested the theory by adding in the offset term into the calculation as described above. A starting value for the offset was chosen, and theoretical ranges were calculated for all the ranges in the data set under test. Different offset values were tried until there was a reasonable correspondence between the theoretical and real values. This process is illustrated in the graphs (figures 4.2 to 4.4) where I have plotted points and the best fit lines for a few offsets around the final value. I have also plotted the $y = x$ line so that one may get an immediate impression of the quality of the fit.

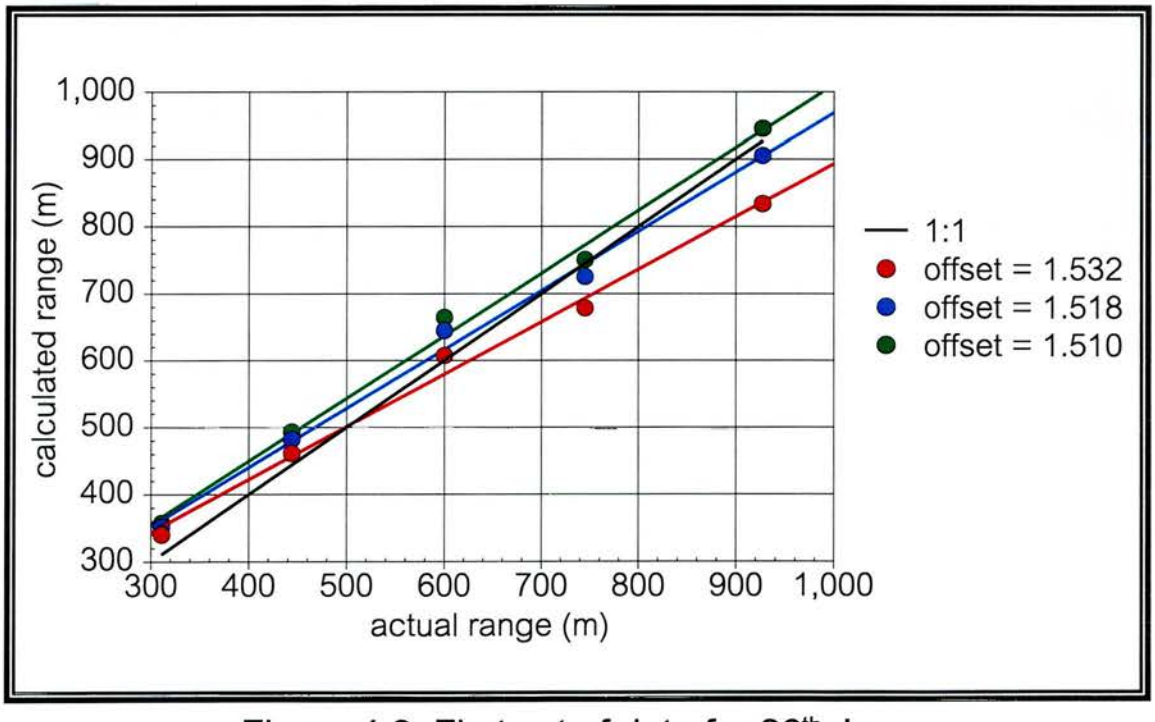

Figure 4.2 First set of data for 26th June

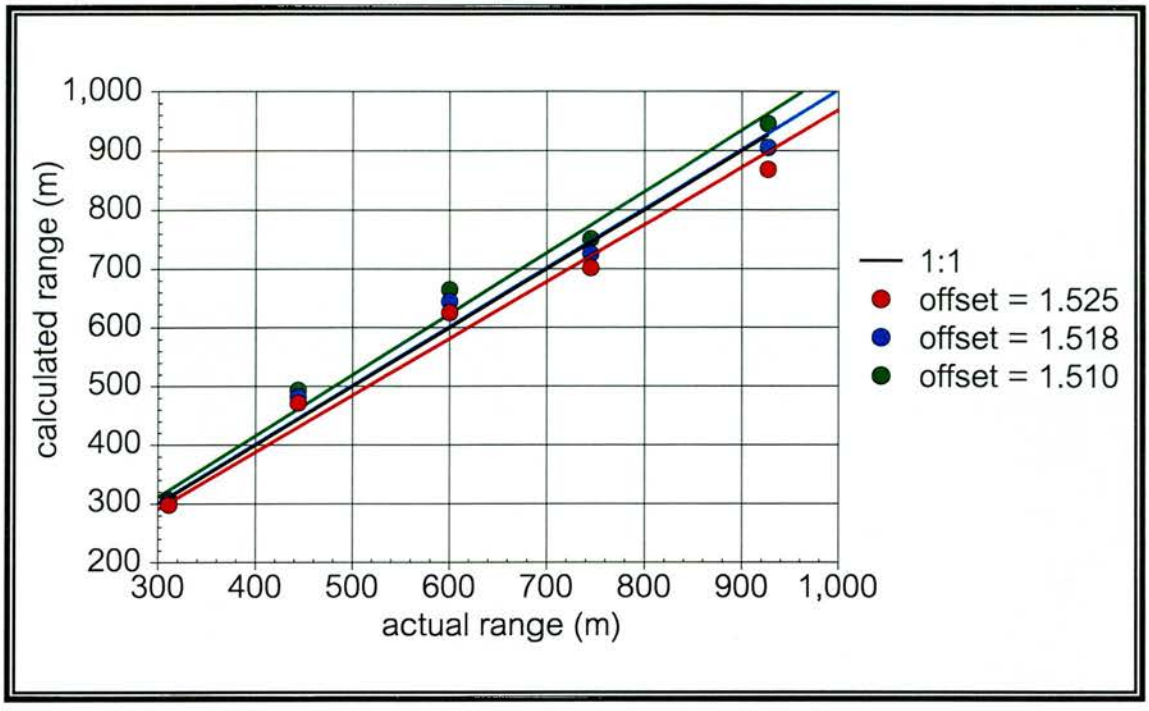

Figure 4.3 Second set of data for 26th June

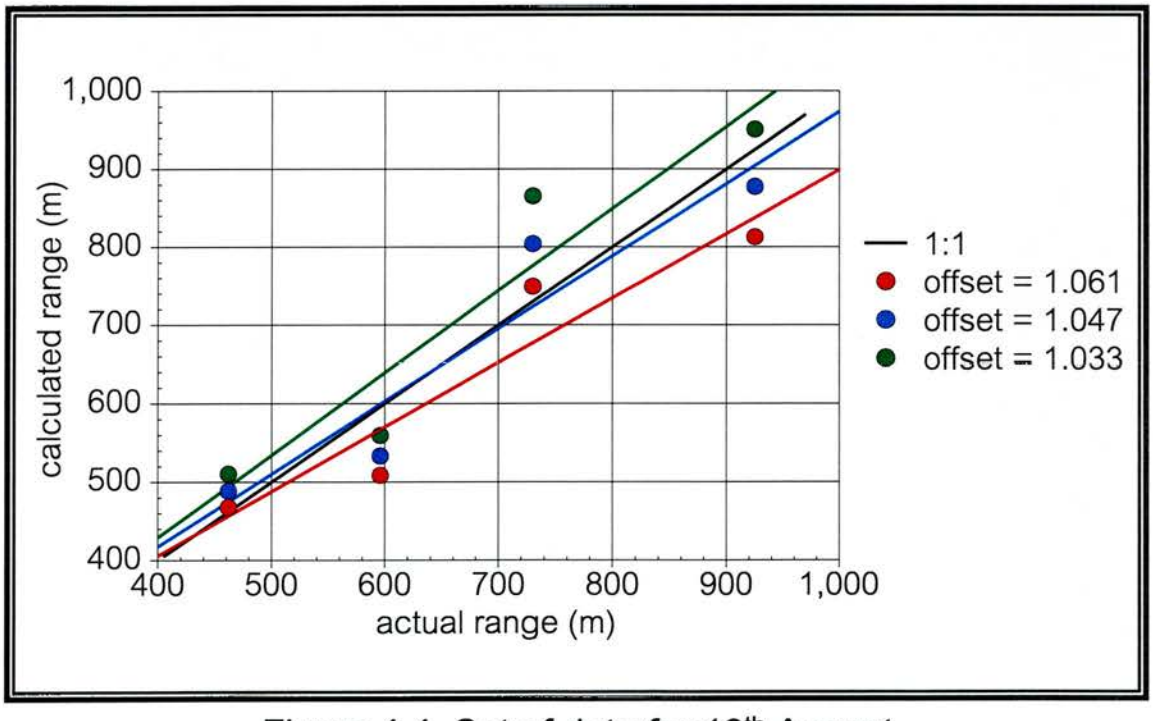

Figure 4.4 Set of data for 19th August

As can be seen from the graphs, the best results are the two sets from the 26th of June, and in particular the second set. For both these sets, the calculated points

are fairly close to the real values once the correct phase offset term has been applied. The sets taken on the other days are less convincing, however. For the set of results from the 19th of August shown in figure 4.4 for example, the actual data points are much further away from the $y = x$ line, even though the best fit line for these points is quite close. Another point to note is that the phase offset required to fit the data on the different days varies between 1.0 and 1.6 radians. While this does indicate a relatively constant pathlength difference, probably caused by one of the components being slightly displaced from its ideal position, the day-to-day variation is still over 50%.

The likely explanation for the variation of the offset value lies in the physical instability of the system. At 95GHz the above range of phase offset values corresponds to pathlength variations between 500 and 800μm. In the size of instrument being used, this represents a relatively very small movement. It is therefore clear that, ideally, movement of components should be kept to a minimum. The tolerance level required for a given range measurement accuracy can be found theoretically, as described in the next section.

4.3 Tolerance

As shown in the previous section, the introduction of a constant offset gives calculated range values which are close to the actual values. However, there is still a fair amount of fluctuation in the accuracy of these calculated ranges, both within a data set taken on one day, and between data sets taken on different days. We can assume that each of these fluctuations is caused by a variation $\delta\Theta$ in the measured phase differences. Equations (4.1) and (4.2) can therefore be rewritten as

$$\Theta_1' = \Theta_1 + \Delta\Theta + \delta\Theta; \quad (4.3)$$

$$\Theta_2' = \Theta_2 + \Delta\Theta + \delta\Theta, \quad (4.4)$$

Again, the small fluctuations in phase difference correspond to small path length changes $\delta l = \lambda\delta\Theta$. We can now determine the relationship between this path length change and the corresponding change in the calculated range, δr, which we will call the *range error.*

4.3.1 Theory

We will only concern ourselves with the boresight case where $\Theta_1 = \Theta_2 = \Theta$. In this case, a right-angled triangle will be formed by the source, the centre port, and one of the side ports. The distance from the source to the centre port is defined as r, and the source - side port distance is $r + l$ where $l = \lambda\Theta$. The equation for this triangle is therefore

$$(r + l)^2 = r^2 + X^2. \tag{4.5}$$

Expanding the bracket and simplifying, we obtain

$$l^2 + 2rl - X^2 = 0. \tag{4.6}$$

By solving this quadratically for l and ignoring the negative root, which is meaningless in this context, we can get an expression for l in terms of r:

$$l = \sqrt{r^2 + X^2} - r. \tag{4.7}$$

By differentiating l with respect to r we get

$$\frac{\mathrm{d}l}{\mathrm{d}r} = \frac{r}{\sqrt{r^2 + X^2}} - 1, \tag{4.8}$$

and we can therefore write

$$\delta r = \left(\frac{r}{\sqrt{r^2 + X^2}} - 1 \right)^{-1} \delta l. \qquad (4.9)$$

Using this equation we can determine how the small path error affects the range measurement at different ranges. At large ranges, the range error will be much greater, as the term in the brackets tends to zero for large values of r.

In the graph below, I have calculated the range error at ranges from 100m to 10km for a few different values of path error. The graph is plotted on a log-log scale, because for any given path error the range error rises exponentially with range. As a result of this behaviour, large ranges become difficult to measure unless we can eliminate as many of the sources of pathlength error as possible.

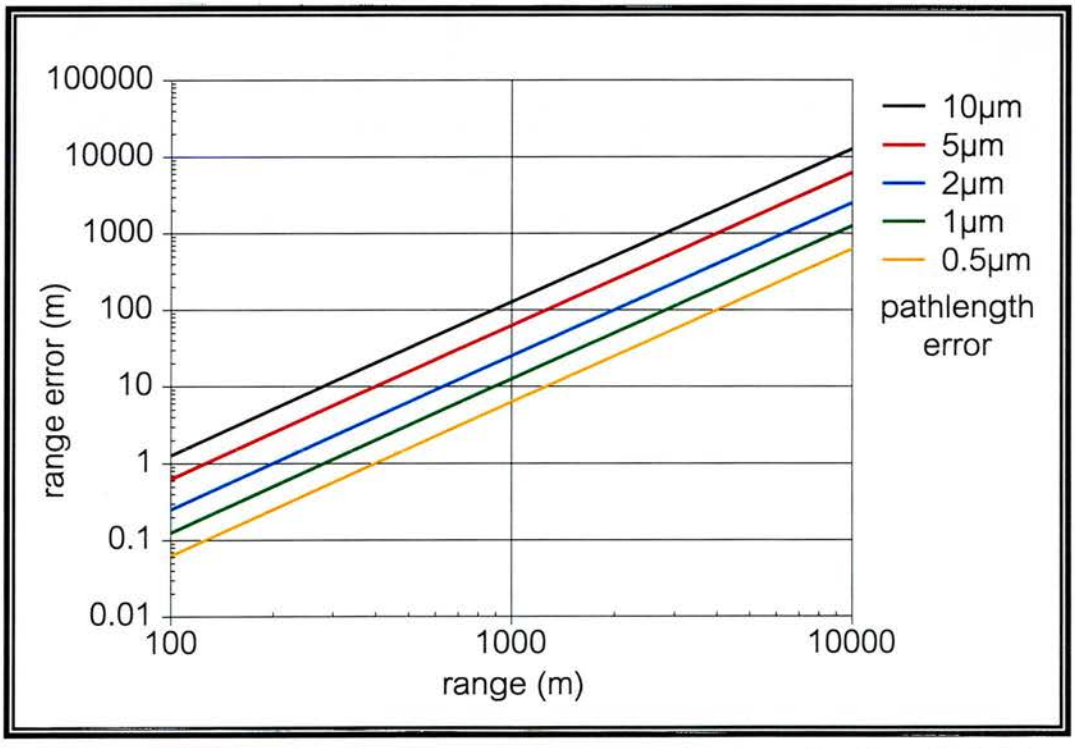

Figure 4.5 Graph of range error against range for X = 0.396m

The graph above shows the expected range error with range for a given pathlength error. Another way of looking at the problem is to ask what level of

stability would be required for a given percentage range accuracy. The graph below illustrates this.

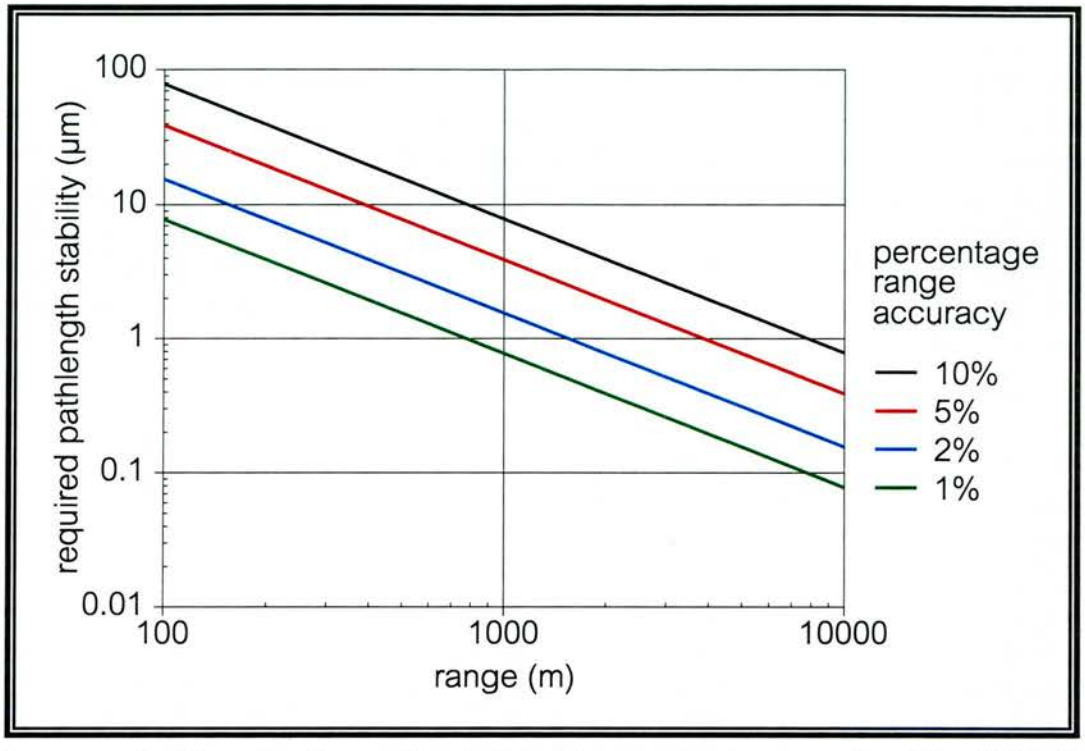

Figure 4.6 Graph of required stability against range for X = 0.396m

4.3.2 Reevaluation of results

FIGURE 4.7 on the following page shows how the above theory could help explain the results obtained. I have redrawn the second graph for the 26th of July to show only the points calculated using the constant phase offset term of 1.52 radians and I have again plotted the $y = x$ line for comparison. In addition I have put in two 'tolerance lines'. These are the loci of points that would be obtained if any component in the system were to move by 10µm, thereby increasing or decreasing the total pathlength by that amount.

Since all the points are between these lines, we can say with relative confidence that during the course of those measurements, no component in the system moved by more than 10µm. The results for the 19th of August are much less

consistent however, and it is likely that something in the system moved by a greater amount.

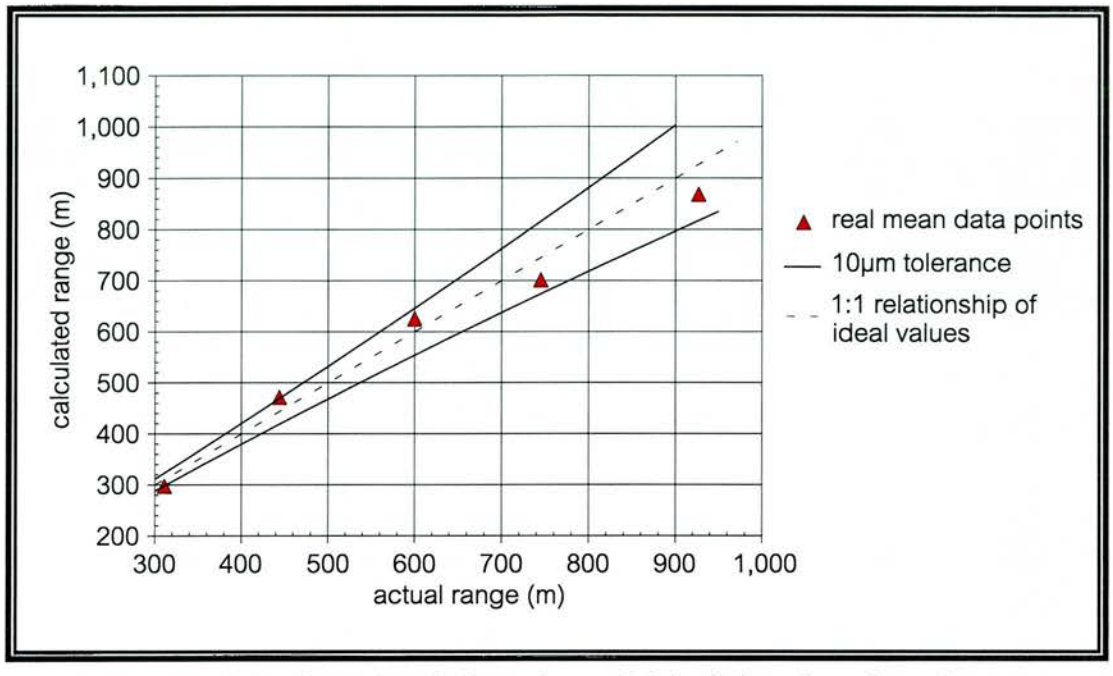

Figure 4.7 Graph of data from 26th July showing data points within tolerance lines of 10µm

4.3.3 Sources of error

PERHAPS THE most obvious source of error, as I assumed in the previous section, is the mechanical instability of the instrument. The half cubes holding the polarisers and other components in the original system were mounted on second half cubes which were attached to the baseplate by steel dowels. This arrangement meant that the components were not fastened down securely and it was fairly easy to cause them to move in their mountings.

Thermal expansion may also be a factor in causing errors in measurement, as the coefficient of expansion of aluminium is about 23µm m^{-1} $°C^{-1}$. However, the symmetrical design of the circuit should lead to all pathlengths increasing or decreasing equally, therefore cancelling out any effect.

A third possible source of error is atmospheric turbulence. Changes in the refractive index of the air through which the signal propagates will result in changes in the phase of the received signal, in turn resulting in changes in the measured range. This will be considered in more detail in later chapters.

Whatever the other possible causes, it is clear that the mechanical stability of the instrument has to be as high as possible. Only then can the other possible sources of error be reliably examined. I decided that the best approach would be to redesign the system with the aim of making it as rigid as possible. The issues involved in this redesign are discussed in the next section.

4.4 Considerations for system redesign

THE ORIGINAL system consisted of an aluminium baseplate with the quasi optical components attached, and of a 'front end' made from aluminium box section to hold the mirrors, the front lens antennas and some extra focussing lenses. The front end meant that a port spacing of about 40cm, giving a total span of over 80cm, could be achieved using the existing 50cm square baseplate. However, the design was far from robust, and flexed very easily.

The large size of the instrument also meant that the beam size at the front ports was larger than one half cube height, hence the need for the extra half cube under each component. However, as was mentioned in the previous section, due to the structure of the half cubes it was impossible to fasten them securely to the baseplate if they were stacked on top of each other. This is simply because they were not originally designed that way. They have, in addition to three locating holes for steel dowels, one threaded hole that can be used to fasten it down with a screw from beneath the baseplate. However, when stacking one on top of another, this secure method of fastening is not possible and we have to rely on the dowels alone, which unfortunately allow some

degree of movement. The freedom of movement of any one component was in fact of the order of one millimetre, so in this context the tolerance achieved on the 26th of June seems quite impressive.

The solution seems obvious. A smaller instrument would mean that all the components and the front lens antennas could be fitted on one baseplate, eliminating the need for a separate front end. Also, given the shorter distance the beams would travel in the system, they could be kept narrow enough to allow the front lenses to fit in one half cube. This would mean that the second layer of half cubes would not be needed and therefore that the components could be securely fastened to the baseplate with screws.

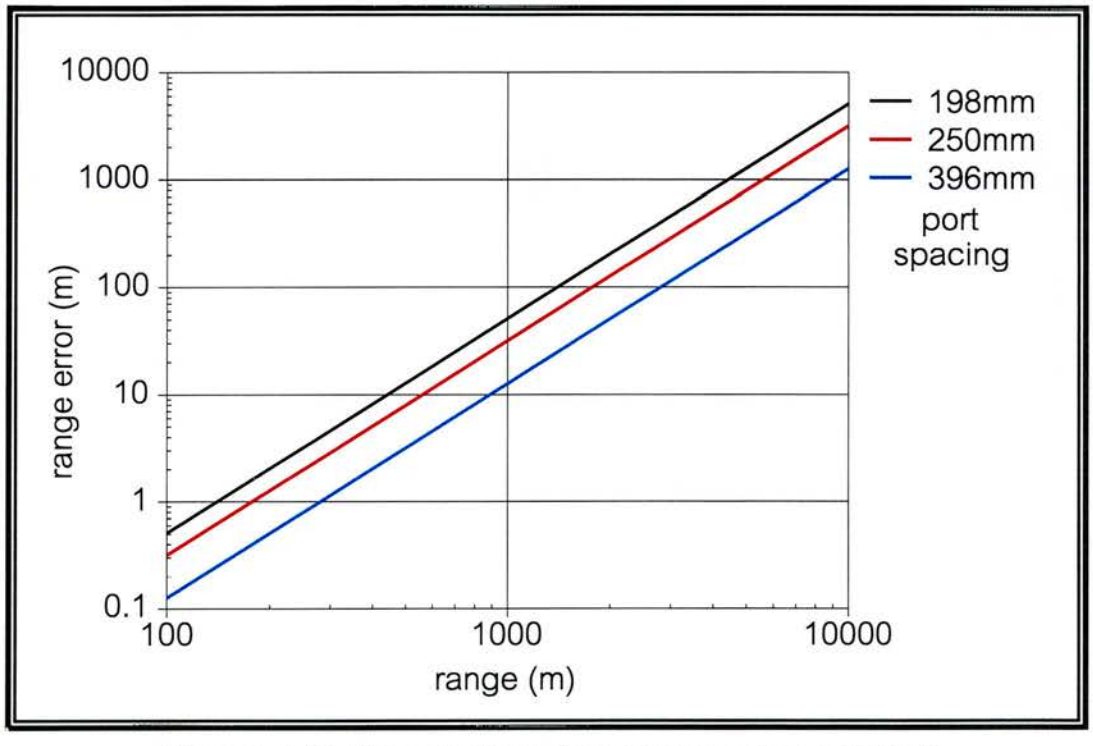

Figure 4.8 Graph showing range error against range for different port spacings

However, before we go ahead and look at redesigning the instrument in this way, it is worthwhile to look at the potential drawbacks of a smaller system. A

glance at equation (4.7) indicates how port spacing will affect the accuracy of the system. In a smaller system, the port spacing X will be proportionately less. The term in brackets will therefore approach zero faster than for a larger spacing meaning that at any one range, if we have the same pathlength error, the range error will be greater. This is shown graphically in figure 4.8. It can be seen from this graph that halving the port spacing from 39.6cm to 19.8cm will increase the range error fourfold. The conclusion from this is that we need to make sure that the mechanical stability of the smaller system is at least four times greater than that of the larger one, in order for the redesign to be worthwhile.

At the time I was considering redesigning the system it became apparent that long-range measurements would no longer be practical, and therefore that I would be performing experiments at shorter ranges. This made the prospect of a smaller system more attractive. The design and construction of the new system is considered in the next chapter.

Chapter 5
Experimental Setup

In this chapter I will describe the redesign and building of the system which was proposed in the previous chapter. I will also describe the calibration and initial testing of the instrument. In addition, I will give a description of the data processing methods used and the programs written for the capture and processing of the data.

5.1 Description of new system

The conclusion reached at the end of the previous chapter was that in redesigning the system it would be best to make it smaller but more rigid. In the end, I decided on a setup that would result in a port spacing of 197.990mm, or half the spacing of the previous system. This was principally because of the ease of construction of a system with these dimensions given the pitch of the locating holes in the existing components.

The previous system consisted of an aluminium baseplate with all the quasi-optical components attached and a box section aluminium front end to hold the mirrors and lens antennas. I decided to use the baseplate as the primary mount for all the parts of the new system. I would therefore require a second, smaller baseplate for the quasi optics and small mounts for each of the mirrors and lens antennas. By mounting all the components on one baseplate in this way, the resulting system would be more rigid than if a separate front end were used as in the previous system.

5.2 Design of new system

THE EXISTING baseplate was already drilled with holes at a pitch of 17.5mm. This would serve as a reference for the holes to be drilled in the secondary baseplate and the three front mounts. The same pitch would be used for these, since the components were already designed and available for this pitch, but the grid would have to be at 45° relative to the primary baseplate.

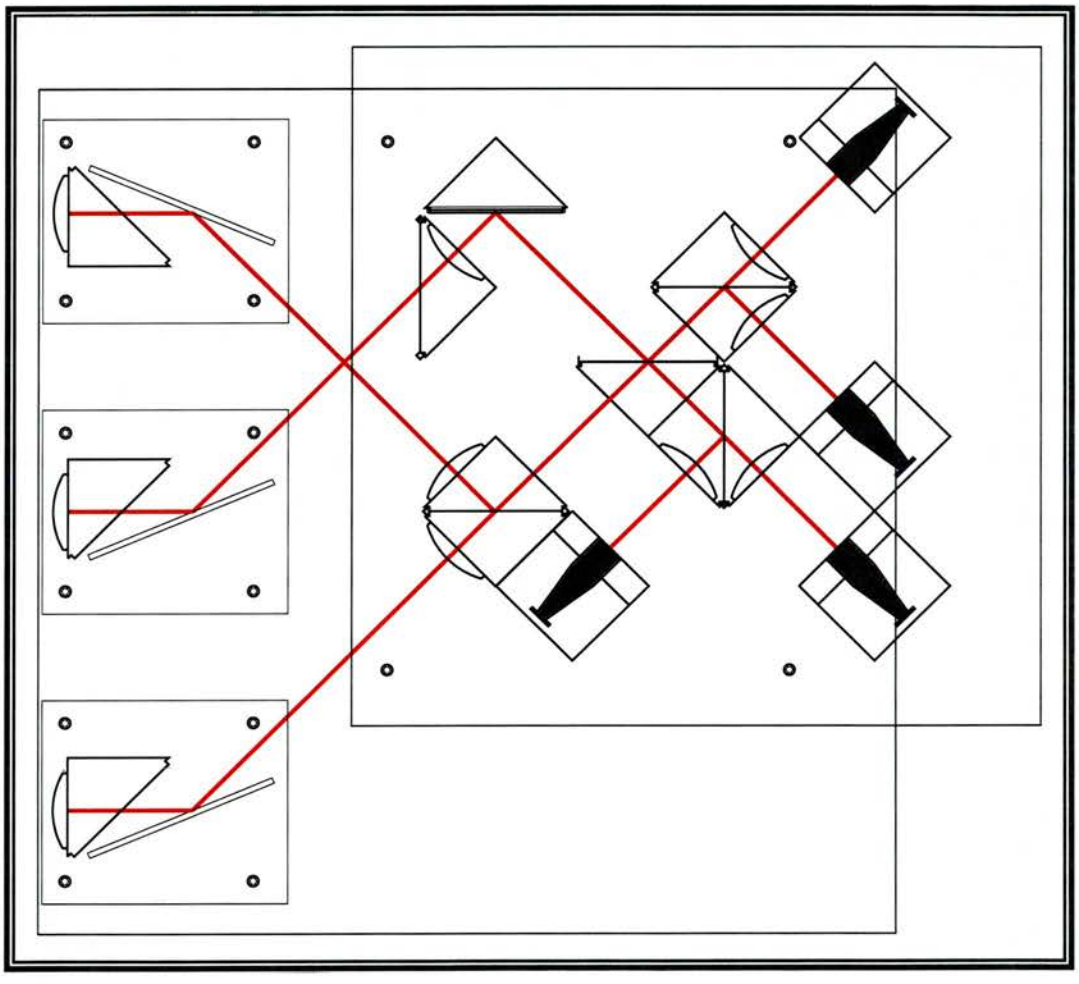

Figure 5.1 A plan of the new system, showing the main baseplate with the four secondary baseplates on top

Calculating the locations of the necessary holes was a fairly straightforward task. The required positions of all the components were found, and the positions of the corresponding holes were calculated for the secondary baseplates. The

positions of locating holes that corresponded with the holes on the primary baseplate were also calculated. To hold the secondary baseplates in position I decided to use aluminium rods drilled down their axes to accept a 4mm bolt. This would allow access to the top of the large baseplate for attaching it to a turntable. Once in place with the locating dowels, the half-cubes holding the components on the secondary baseplates were fastened down securely with bolts from underneath. A plan of the receiver is shown in figure 5.1, and a photo of the final system is shown in figure 5.2

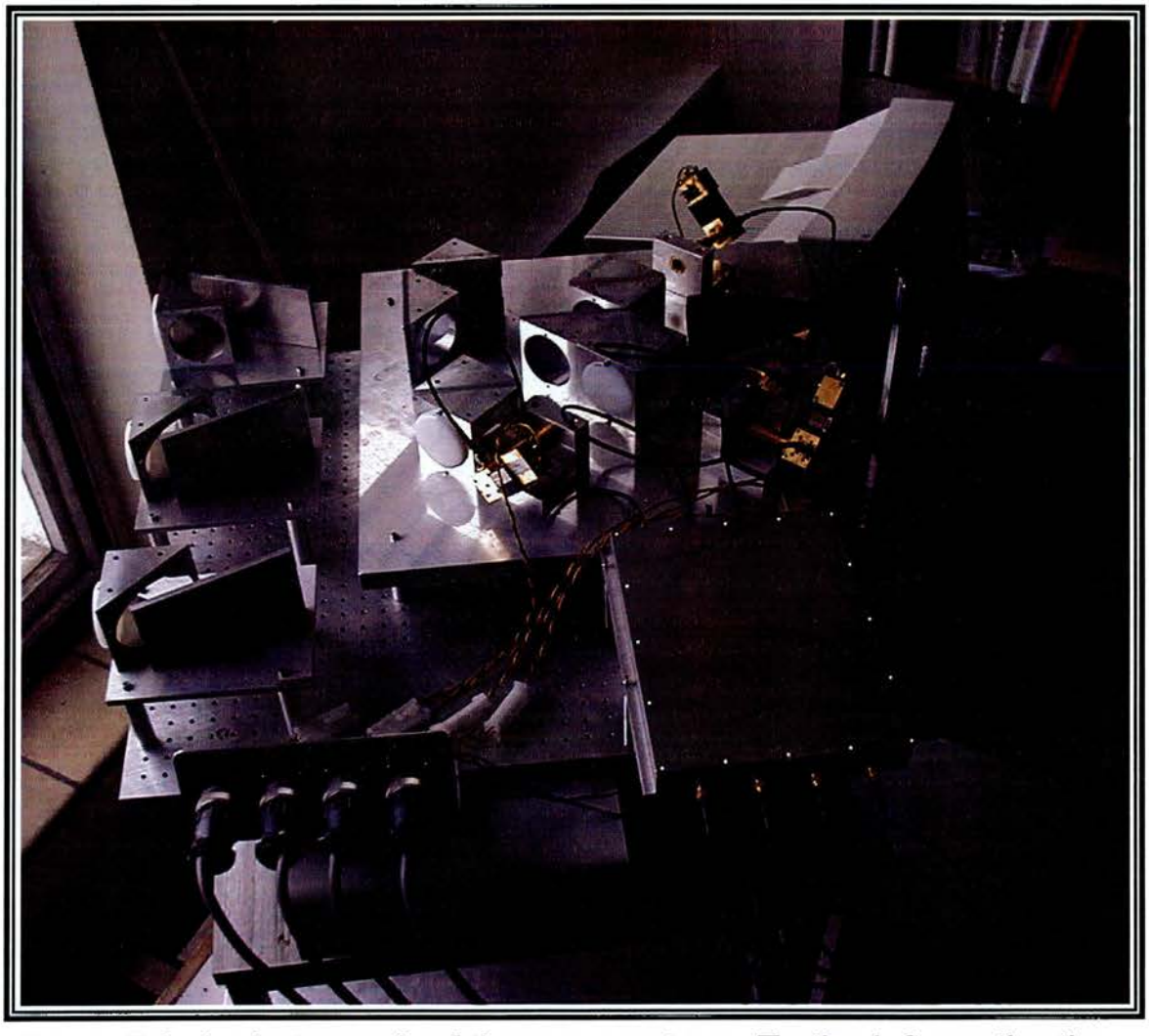

Figure 5.2 A photograph of the new system. To the left are the three small antenna baseplates, and the main quasi-optical processing elements can be seen on the main secondary baseplate on the right.

5.2.1 Lens design

IN ORDER to keep the received beams contained, they need to be periodically refocussed using lenses. At St Andrews, we use dielectric lenses made from high density polyethylene (HDPE). In order to provide an antireflection matching layer, the lenses are blazed with concentric grooves. While easy to manufacture, this does introduce a level of frequency dependence. This is not a problem for this system, as we can arrange that the transmitted signal is always as close as possible to 95GHz.

In order to minimise loss due to absorption, I wanted to use as few lenses as possible. I would need a lens at each port as the antenna, and I would need another in front of each feedhorn to focus the beam down tightly to the feedhorn waist. The maximum throw of a lens this size (53mm diameter) with underillumination ratio 3 at 95GHz is

$$z_{\max} = \frac{\pi\omega^2}{2\lambda} \approx 165\text{mm}.$$

The beam can travel twice this distance, or 330mm, before requiring refocussing. The distance between the two lenses already required is about 610mm, so one more lens is needed for each path. The most convenient position for the extra lens is 280mm from the feedhorn lens, as this corresponds to the position of a half-cube to which the lens can be attached.

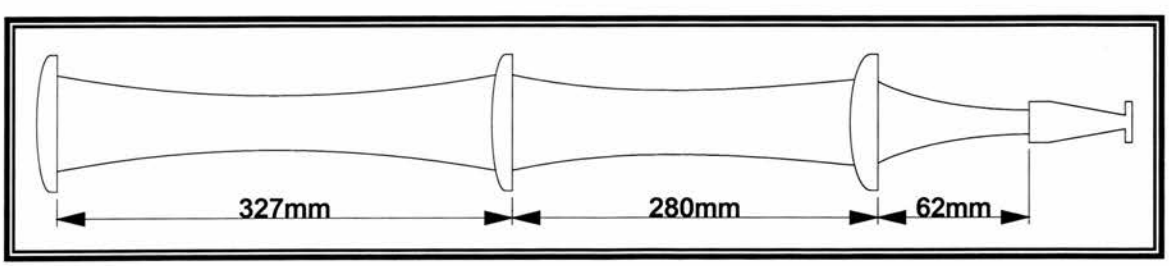

Figure 5.3 Schematic illustration of the beam waveguide employed in the system

The orientation of the lenses is of some importance, and is as shown in the schematic in figure 5.3. There are two main considerations when designing a lens waveguide. The first is that the flat face of the lens adjacent to the feedhorn is oriented towards it. If the lens is the other way round, in other words with the convex face towards the horn, then standing waves may form between the feedhorn and the planar face of the lens. With the lens oriented as shown above, any reflections off the curved dielectric-air interface will be highly divergent and therefore will not couple back into the feedhorn. Another advantage of the orientation used here is that when the planar surface faces the more divergent beam the intensity distribution in the lens matches more closely the intensity of the beam than when the convex surface faces the beam.

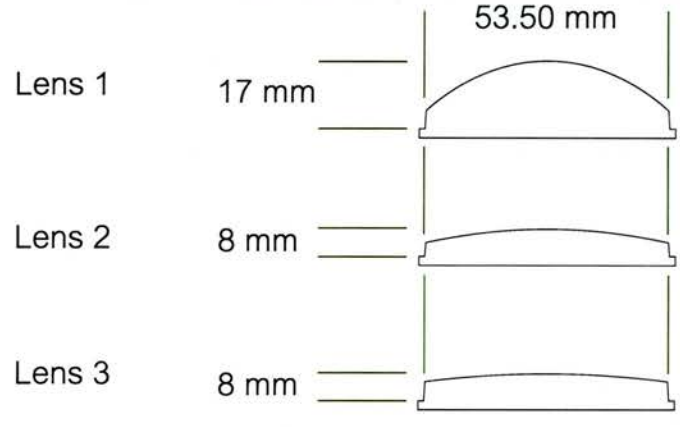

	Lens 1		Lens 2		Lens 3	
	Input	Output	Input	Output	Input	Output
ω_0 (mm)	4.20	15.51	15.51	13.83	13.83	18.17
ω (mm)	14.86	17.43	17.98	18.16	17.92	18.17
R (mm)	64.78	589.13	548.69	385.85	387.99	107984.8
Z (mm)	59.61	140.00	140.54	170.00	156.97	9.00
U	3.60	3.07	2.98	2.95	2.98	2.94

Note: Input refers to flat face, output to curved face

Figure 5.4 Profiles of the three lenses, as calculated from the lens design program.

The second consideration is regarding the orientation of the other lenses. It is important that the planar faces of two adjacent lenses are not facing each other. This is to avoid setting up Fabry-Perot type standing waves between the lenses.

Now that the positions of the lenses had been established, it was necessary to calculate their profiles. This was done with the aid of a C program developed by Lesurf and Smith based on an iterative technique described by [HARV90]. The profiles are shown in figure 5.4, together with data on each lens. It can be seen from the table that the input beam waste for one lens corresponds to the output beam waste from the previous.

5.2.2 Designing the mirrors

ONCE THE position and focussing behaviour of the lenses had been established, it was necessary to calculate the size of the mirrors which would be situated on each of the three front antenna mountings. The position of these mirrors was already determined by the geometry of the setup, but the size would be determined by the width of the beam at the point where it would meet the mirrors. The calculation of the necessary mirror size was done graphically by plotting the beam profile from the middle lens (lens 2) and then plotting a line intersecting it where the mirror would be. Allowing for an underillumination ratio of 3 and an extra margin of error, a mirror size of 130mm wide by 70mm high was decided upon.

5.3 Source setup

THE SOURCE used in the experiments is a Gunn diode oscillator operating at 95GHz. A controlling heater is attached to the oscillator block in order to provide thermal stability, thereby improving the stability of the power and frequency outputs. A variable attenuator is put in front of the oscillator, and in front of that is a PIN switch, as shown in figure 5.5 below. The variable

attenuator is to control the level of the signal so that it doesn't saturate the receiver amplifiers, and the PIN switch is to modulate the signal at a known frequency in order to improve detection by a phase sensitive detection method [LESU95], Chapter 16. The modulation is often applied to the received signal in phase sensitive detection techniques, since the source is usually not controllable (if it is a star, for example). In this case, the source is under experimental control, and so the modulation can be easily incorporated. The advantage is that only one PIN switch is required, whereas four would be needed if they were used on the receiver. Also, we are not chopping the background, and are thus able to filter out its contribution to the noise level. The reference signal for the PSD at the receiver end will be supplied by the computer program described in section 5.5.

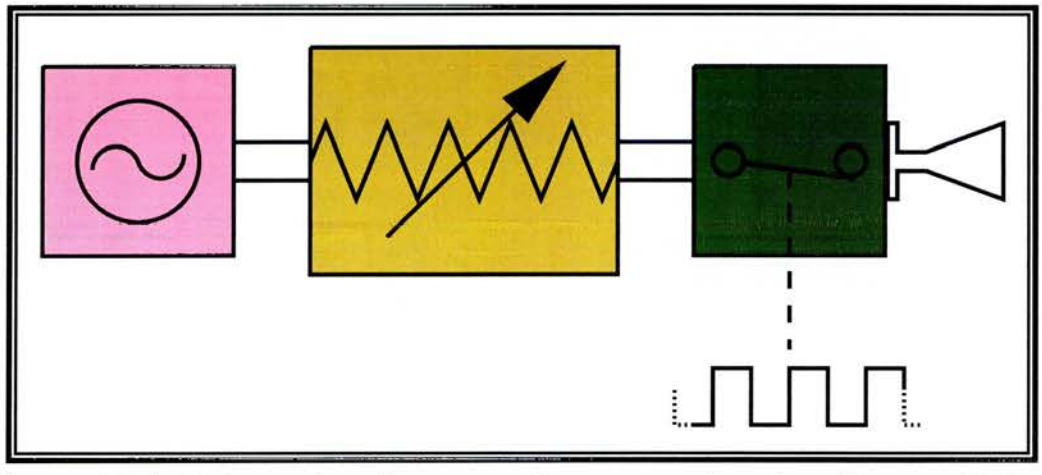

Figure 5.5 Schematic diagram of source, showing the oscillator, attenuator, PIN switch and feedhorn

5.3.1 PIN switch modulation circuit

In order to drive the PIN switch, a modulation signal is required. The 'on' voltage for this particular PIN switch is 1.2V and the 'off' voltage is zero, so a circuit is required which switches between these levels at the desired modulation frequency f. The circuit used is shown in figure 4.4. The signal is provided by a crystal oscillator with a fundamental frequency f_0 of 16MHz.

The multiplexer in the crystal oscillator I.C. allows the frequency to be divided by 128, to 125kHz. An LS93 divider I.C. is used to divide the frequency again, this time by 16, to obtain the modulation frequency 7.8125kHz.

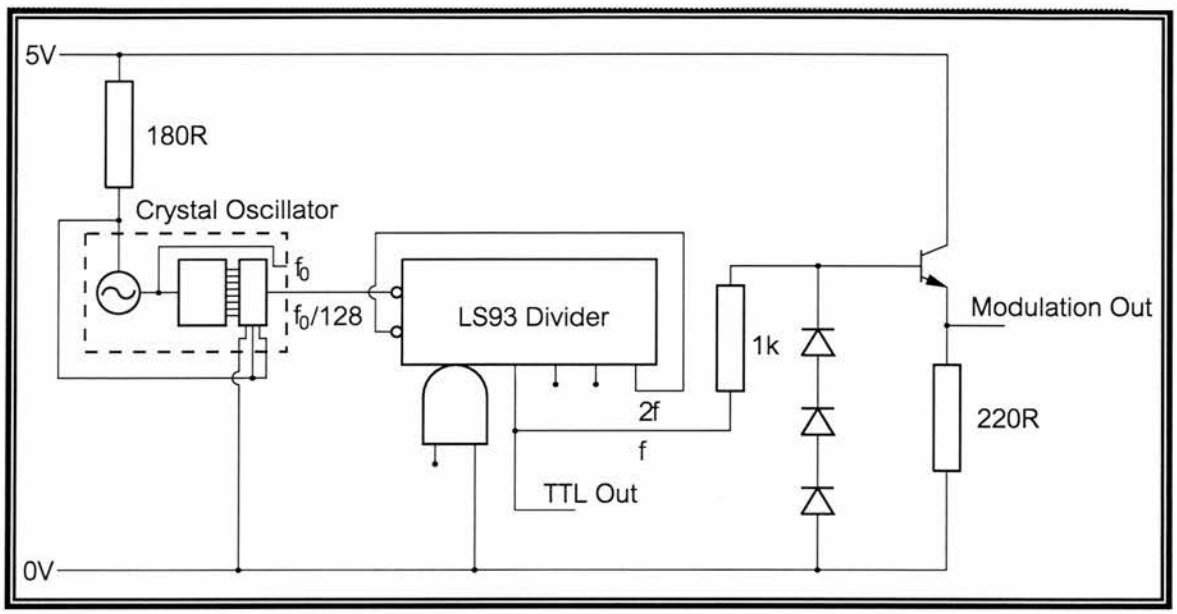

Figure 5.6 PIN diode modulation circuit.

The output from the divider is brought down from five volts (TTL) to 1.2 volts with the aid of the three diodes and a transistor. The diodes prevent the voltage at the base of the transistor going above 1.8 volts, and the base-emitter voltage of 0.6 volts provides the drop to the required output voltage.

A printed circuit board was designed for the circuit, with the inclusion of small decoupling capacitors at the five volt supply inputs of the two I.C.s. The five volts itself was supplied by a 7805 voltage regulator running off a 12 volt car battery supply. The circuit was housed in a small die-cast aluminium box before being ready for use.

5.3.2 Gunn oscillator power supply

THE TYPE of Gunn oscillator power supply used at St. Andrews is described in detail elsewhere [ROBE94b], and will therefore only be covered briefly here. The bias voltage is supplied by a 7805 regulator, and is adjusted by a 10-turn pot. The necessary current (about 1A) is provided by a series pass power transistor. Since a voltage of over 5V is required, diodes are used in order to raise the regulator output above its nominal 5V rating. I have modified the circuit to include only two of these diodes, since that produces a high enough voltage to supply the Gunn bias, but allows the voltage of the power supply to drop below 10 volts before the regulator moves out of its optimal operating area. This is important in providing a more reliable bias to the oscillator, since the power will be supplied by the car battery mentioned in the last section, whose output voltage drops as it loses charge.

5.3.3 Putting it all together

THE OSCILLATOR, attenuator, PIN switch and feedhorn arrangement are mounted at 45° on a piece of ¼″ aluminium tool plate. An additional circuit is required link the battery with the PIN switch and Gunn oscillator supplies, and also with the heater. This circuit is shown in figure 5.7.

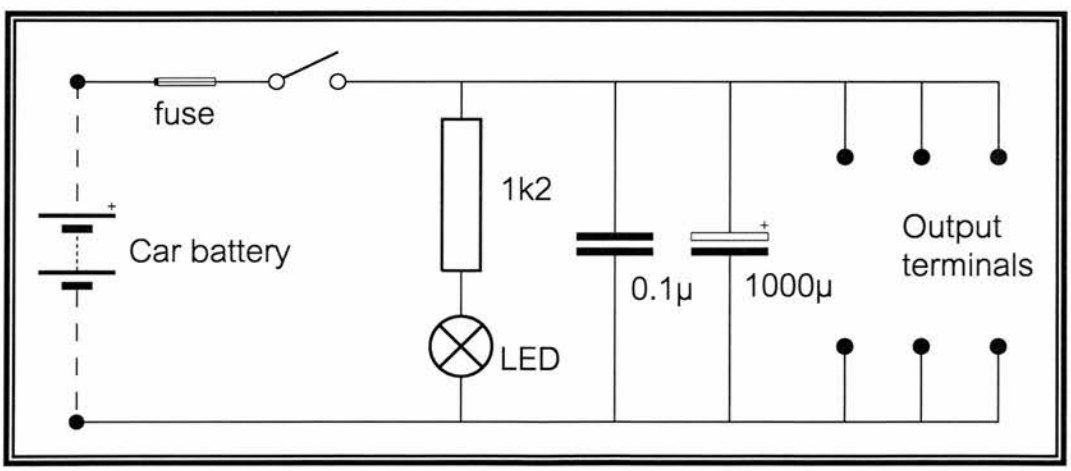

Figure 5.7 Power supply distribution circuit

The whole equipment is housed in a large plastic box made by Curver™, which is transparent to millimetre waves.

For use in the field, a 2.5m high platform was constructed upon which the box with the transmitter could be placed. The platform was made from box section aluminium, with a wooden top for putting the equipment on, and with spikes on the bottom for fixing it firmly into the ground.

5.4 Description of detection equipment

THE DETECTORS used for each channel are heterodyne radiometers. The mixers are fed by a 94GHz local oscillator, which will produce an i.f. of 1GHz when receiving a signal at 95GHz. This 1GHz signal is then passed down an i.f. chain consisting of a d.c. block, amplifiers, attenuators, a bandpass filter and a crystal detector connected as shown in figure 5.8.

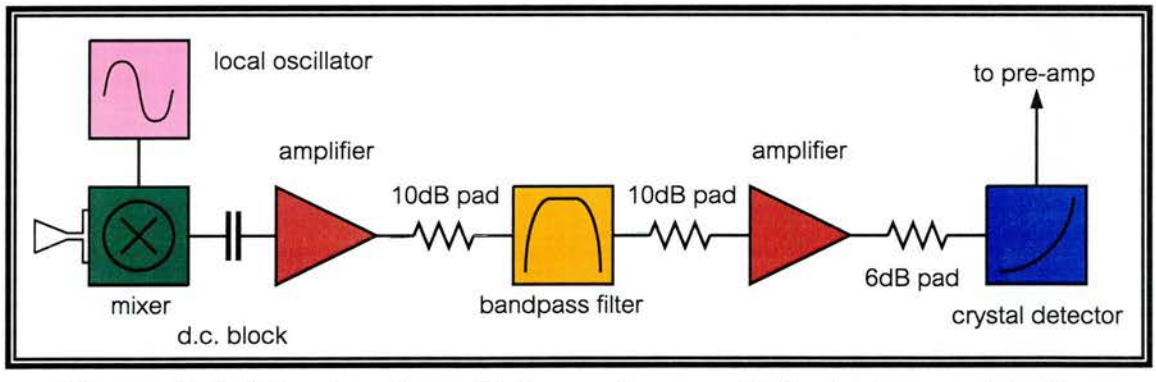

Figure 5.8 The local oscillator, mixer and i.f. chain used in the receiver

5.4.1 Audio-frequency pre-amplifier

THE OUTPUT of the crystal detectors is fed to an a.c. amplifier which provides a voltage gain of about 50 and which filters the output from the detectors. The filter incorporated is a pilot-tone 17kHz low-pass filter, which will reject all but the fundamental frequency of the modulation square-wave. The circuit for this amplifier is shown in figure 5.9.

The two operational amplifiers are set up as non-inverting amplifiers each of voltage gain 10, but the filter has a voltage gain of about ½, so the total gain of the amplifier is 10 × ½ × 10 = 50. In addition to the two RC high pass filters before each op-amp, a high pass filter is put on the output, because it was discovered that some of the channels had a small d.c. offset on the output voltage.

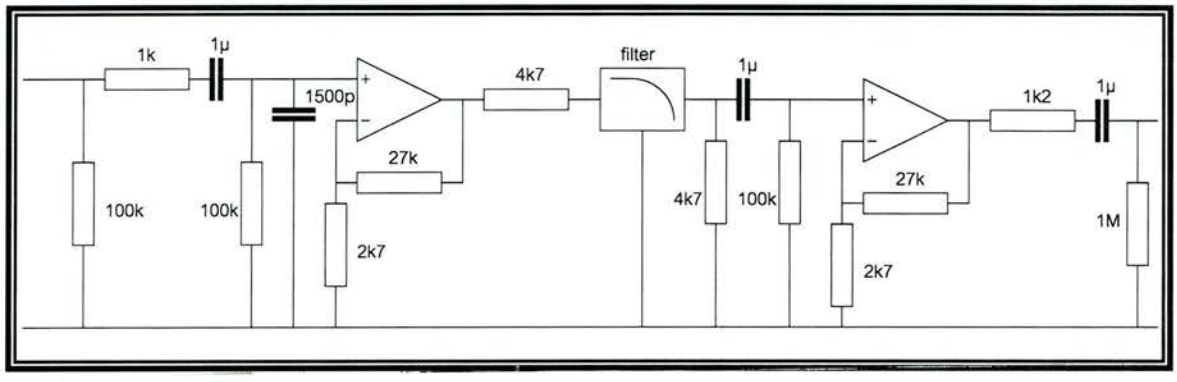

Figure 5.9 Circuit diagram for the audio preamplifier

The filter was chosen to pass frequencies of above a few Hertz. A typical response of the amplifier with frequency is shown in figure 5.10.

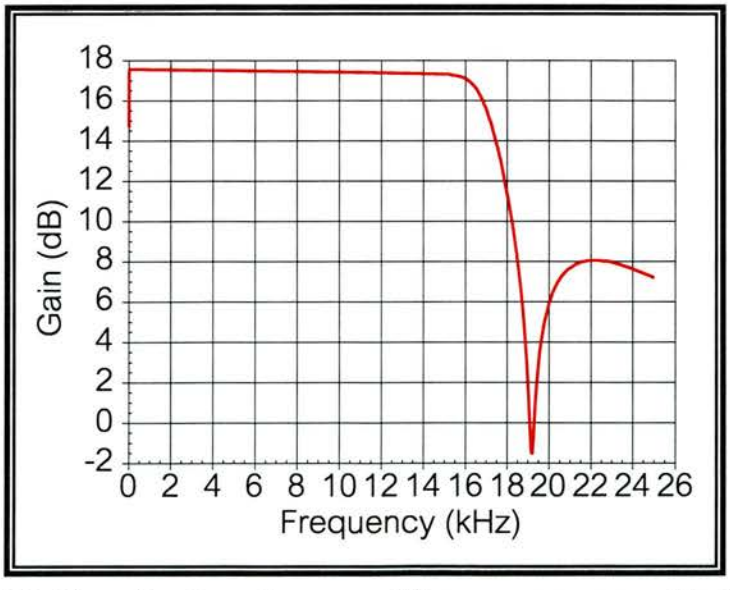

Figure 5.10 Graph showing amplifier response with frequency

5.4.2 Calibration of crystal detectors

THE CRYSTAL detectors were calibrated in order to obtain the relationship between power in and voltage out. A 1GHz signal, modulated at 1kHz, was provided by a signal generator. The output from the crystal detector was fed to the audio-frequency pre-amplifier, whose output voltage was read using a true-rms digital voltmeter. A graph of voltage versus power was plotted for each detector and a curve was fitted using a curve-fit program. The data obtained, and the curves fitted to the data, are shown in figure 5.11.

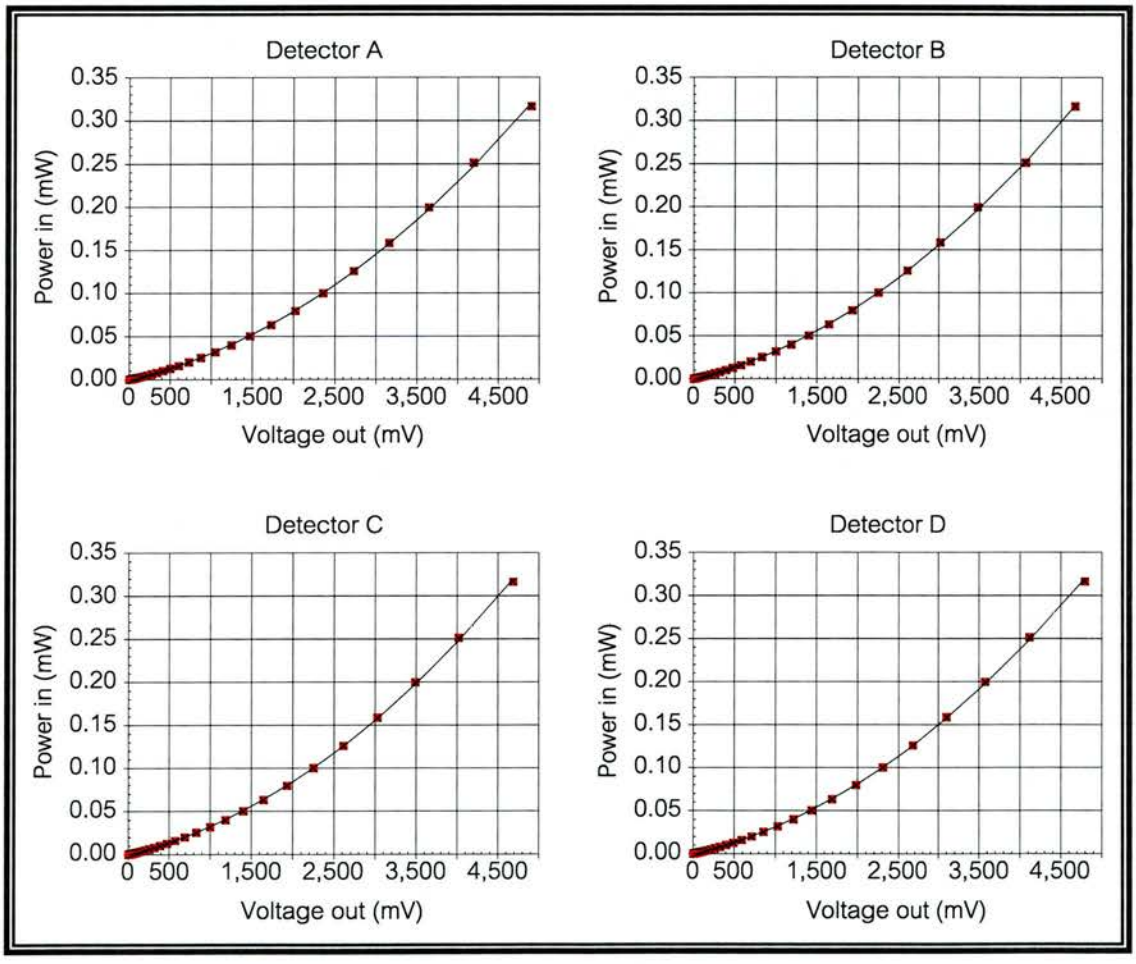

Figure 5.11 Crystal detector power curves

The equations of the fitted parabola can be used to calculate power values from the detected voltages at the computer. The coefficients of the quadratic

relation

$$P = aV^2 + bV + c,$$

where P is the input power in mW and V is the output voltage in mV, are given in the table below.

Detector	a	b	c
A	8.9048×10^{-9}	2.1692×10^{-5}	-1.8957×10^{-4}
B	9.6757×10^{-9}	2.2834×10^{-5}	-1.4807×10^{-4}
C	9.6904×10^{-9}	2.2816×10^{-5}	-1.5280×10^{-4}
D	9.3273×10^{-9}	2.1988×10^{-5}	-1.4482×10^{-4}

These coefficients can now be used to obtain values for the power falling on the crystal detectors, when a given voltage is measured at the output of the amplifier.

5.4.3 Measurement of i.f. gain

THE MEASUREMENTS done in the previous section allow us to calculate the power at the input to the crystal detectors. This power is in turn determined by the behaviour of the i.f. chain and also the conversion loss of the mixer, which will be dealt with in the next section.

The i.f. gains were measured as follows. A signal generator was used to produce a signal at 1GHz. This was fed into the i.f. chain being measured. The output power was measured using a spectrum analyser. This was done for 7 input power levels from -70 to -100dBm, and was repeated for each channel. An average gain in dB was calculated for each channel, the results being:

Channel	Gain
1	57·71dB
2	58·01dB
3	57·73dB
4	57·24dB

These gain figures can be used to calculate what the signal power would have been at the output of the mixer.

5.4.4 Mixer conversion loss

THE FINAL stage in calculating the input power from the voltages arriving at the computer, involves measuring the conversion loss of the mixers which receive the r.f. signals. A Gunn diode like the one used in the source setup was used to supply the input signal. The frequency and input power were measured using a EIP frequency counter and Boonton power meter. The output i.f. power was measured using the spectrum analyser. The results are shown in figure 5.12.

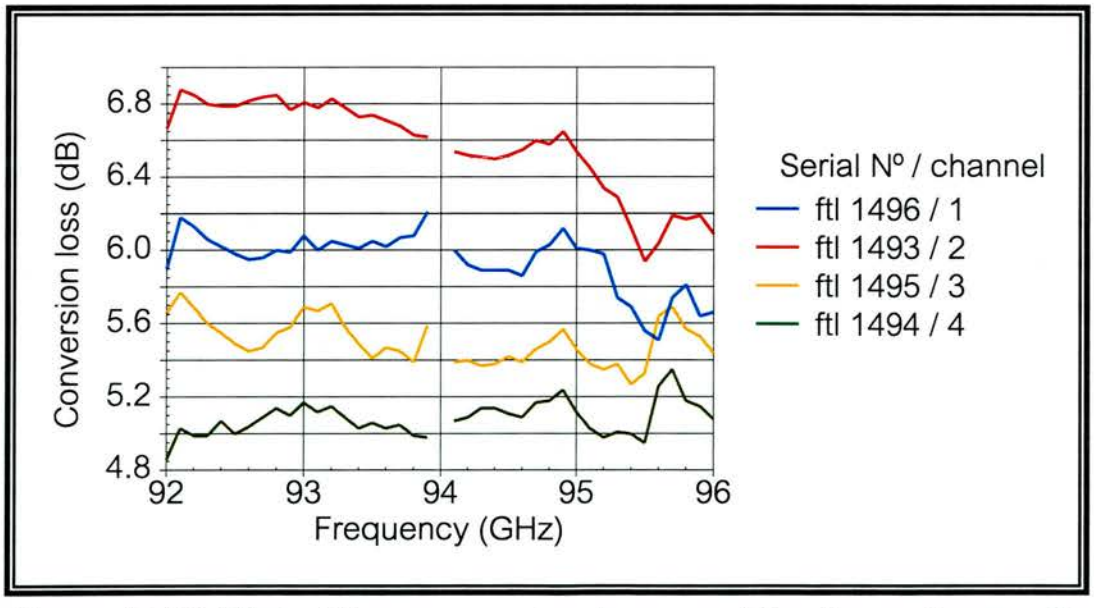

Figure 5.12 Plot of the conversion losses of the four mixers with frequency

At the chosen operating frequency of 95GHz, the graphs are slightly sloped, meaning that any variation in frequency will result in a change in conversion loss. However, as all the mixers exhibit similar behaviour, any change would be mirrored across all four.

The values for the conversion loss at 95GHz were incorporated into the calculation of the final relative gains for each channel, for use in the program described in the next section.

5.5 Data capture

THE DATA capture was done using an Acorn RiscPC and an ADC card from Intelligent Interfaces. The C routines written for this are transcribed in full in Appendix 2 and will only be referred to below. The program written consists of several functions all called from the function `main()`. Some of these functions are described in the following section.

5.5.1 Overview of program

THE DIFFERENT functions are saved in different files and are linked together using Make. This necessitates the creation of a header file (`program.h`) in which the various functions are declared and global variables are defined. Various arrays are set up in `main.c`. There is one large array for each channel, the size of which was usually set at 16kb. These arrays will be passed to the data capture routine where they will be filled with data captured by the card; they will then be passed to the routine `psd()` which will work out the amplitude of the signal in each channel as described below. The two arrays `sine[]` and `cosine[]` are required for this purpose. The two remaining arrays, `psd_channel_[]` and `if_power_[]` are used to hold the results returned by `psd()` and the routine `get_powers()` which calculates the powers from those results.

An output file is opened in the ram disc to hold the output, and then the routine `introduction()` is called. This routine begins by looking in a file called "offset" which is in the program directory. If the file is not present, it creates it, otherwise it reads the the value from the file, which will be the previous offset value given by the user. This offset value is the variable $\Delta\Theta$ described in the previous chapter. The user is then asked to input a value for $\Delta\Theta$, with the value read from the file given as the default value which will be used if no new value is given. Finally, a value for the number of trials is requested. The values for the offset and for the number of trials are passed back to `main()`. The next routine to be called is `make_psd_tables()`. This routine simply creates a sine and cosine at the modulation frequency and puts them in the `sine[]` and `cosine[]` arrays, ready for use during the rest of the program.

At this point the data capture and process loop is begun. A `for` loop is started, with the number of passes being set to the value for the number of trials given by the user in `introduction()`. The function `get_data()` is called, which reads data in from the card and puts it in the arrays `channel_1[]` to `channel_4[]`, before passing the arrays back to `main()`. The function `psd()` then operates on each of the four arrays, providing an average voltage level for each channel, placing the four results in the array `psd_channel_[]`. Next, this array is sent to the `get_powers()` function, along with the `if_power_[]` array and the offset value. In this function, the coefficients a, b, and c, as calculated in section 5.4.2, are used along with the calculated gains to produce values for the powers at each of the four detectors from the PSD voltages. Finally, the function `get_r_and_phi()` is called to calculate the range and bearing using the equations (3.14), (3.15), (3.44) and (3.45). The four power values, the range, the bearing and the total power are then all saved to disc before the loop is begun again.

Chapter 6
Analysis of Approximations

In this chapter I will explore the validity of the equal received power approximation made in the calculations in the previous chapters and which are used in the rest of this work.

6.1 Initial analysis

As was mentioned in Chapter 3, an approximation was made regarding the antenna patterns of the ports. The problem is illustrated in figure 6.1 below. For simplicity's sake, let us consider a source placed on boresight. This means that this source will be in the middle of the centre port's antenna pattern.

For this analysis we will assume a point source. For close ranges, this is perhaps not the case, so in the next section I will look at the possible implications of this in more detail.

As is clear from the diagram, the source will not be in a central position relative to the antenna patterns of the other two ports, and therefore less power will be received by these. This situation is compounded by the fact that the source-port distances are also greater, so less power will be received for this reason as well.

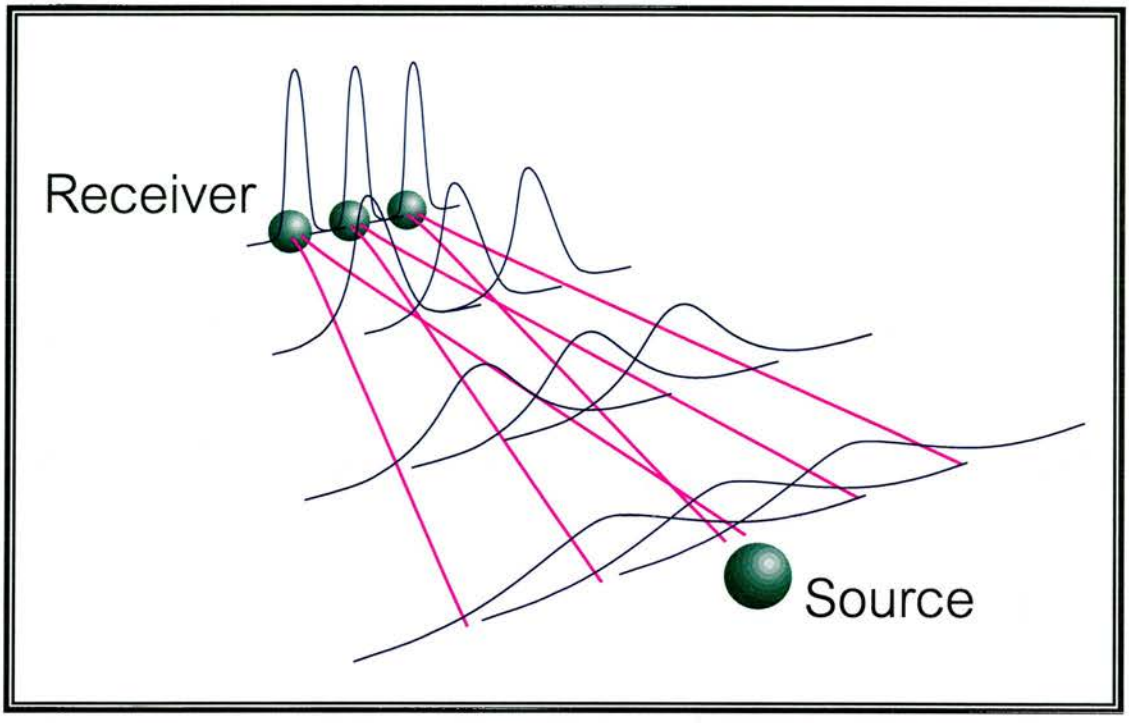

Figure 6.1 A representation of the antenna patterns of the three ports of the receiver. The source is in the middle of the pattern of the centre port, which will therefore receive maximum power. There will be a relative reduction in power received at the other two ports

The angle of arrival at each of the outer ports for the boresight case is determined by simple trigonometry

$$\varphi = \tan^{-1}\frac{X}{r_0}, \tag{6.1}$$

where X is the port spacing and r_0 is the boresight range. The received field relative to the on axis field is given simply as

$$E_{rel} = \frac{r_0}{r}\exp\left\{-\left(\frac{\varphi}{\theta_0}\right)^2\right\}, \tag{6.2}$$

the relative power therefore being

$$P_{rel} = \left(\frac{r_0}{r}\right)^2 \exp\left\{-2\left(\frac{\varphi}{\theta_0}\right)^2\right\}. \tag{6.3}$$

Clearly, for the centre port, with the source on axis, P_{rel} will be 1, and away from this position, it will fall by an amount determined by the beam angle θ_0. The table below shows the relative outer port powers for boresight ranges between 10m and 500m, for two receiver setups. The first is the original three port described in Chapter 4 and in [LESU97]. The second is the modified version described in Chapter 5, designed partly with closer range work in mind.

	Setup 1: $\theta_0 = 1.832°$, $X = 0.396$m		Setup 2: $\theta_0 = 3.196°$, $X = 0.198$m	
range r_0	φ	P_{rel}	φ	P_{rel}
10m	2.268°	0.047	1.134°	0.777
20m	1.134°	0.464	0.569°	0.939
30m	0.756°	0.711	0.378°	0.972
40m	0.567°	0.825	0.284°	0.984
50m	0.454°	0.884	0.227°	0.990
75m	0.303°	0.947	0.151°	0.996
100m	0.227°	0.970	0.113°	0.997
200m	0.133°	0.992	0.057°	0.999
500m	0.045°	0.999	0.023°	1.000

Table 6.1 Relative powers at outer ports for different ranges and for the two receiver setups

As can be seen from the table, the relative powers are very near to unity for all but the shortest ranges. Certainly, for ranges greater than 50m in the case of Setup 2, and 200m in the case of Setup 1, it looks as if it is indeed valid to

assume equal powers are received by all three ports. However, in the interest of thoroughness, I will now work out theoretical values for the powers at each detector, and use these values in the range calculation equations, which were of course derived using the equal powers assumptions. It will therefore be possible to compare the ranges calculated using the approximations with the original range values. I will perform this calculation for Setup 2 only, as it is of more relevance to this work.

We start by rewriting equations (3.30) to (3.33) for the on boresight case. For this case the following are true:

$$\begin{aligned} r_C &= r_0; \\ r_1 = r_2 &= r; \\ \varphi_C &= 0; \\ \varphi_1 = \varphi_2 &= \varphi; \\ \Theta_1 = \Theta_2 &= \Theta. \end{aligned}$$

Equations (3.30) to (3.33) therefore become

$$O_1 = \frac{E_0}{2\sqrt{2}}\left[-\frac{i}{r_0}\right]\begin{pmatrix}1\\1\end{pmatrix}; \tag{6.4}$$

$$O_2 = \frac{E_0}{2\sqrt{2}}\left[-\frac{i}{r_0}\right]\begin{pmatrix}1\\1\end{pmatrix}; \tag{6.5}$$

$$O_3 = \frac{E_0}{2\sqrt{2}}\left[\frac{2\exp\left\{-\left(\frac{\varphi}{\theta_0}\right)^2 - i\Theta\right\}}{r} + \frac{1}{r_0}\right]\begin{pmatrix}1\\1\end{pmatrix}; \tag{6.6}$$

$$O_4 = \frac{E_0}{2\sqrt{2}}\left[\frac{2\exp\left\{-\left(\frac{\varphi}{\theta_0}\right)^2 - i\Theta\right\}}{r} - \frac{1}{r_0}\right]\begin{pmatrix}1\\1\end{pmatrix}. \tag{6.7}$$

The powers are obtained as before by mod-squaring and adding the two components

$$P_1 = \frac{P_0}{4r_0^2}; \tag{6.8}$$

$$P_2 = \frac{P_0}{4r_0^2}; \tag{6.9}$$

$$P_3 = \frac{P_0}{4}\left[\frac{1}{r_0^2} + \frac{4\exp\left\{-\left(\frac{\varphi}{\theta_0}\right)^2\right\}\cos\Theta}{r_0 r} + \frac{4\exp\left\{-2\left(\frac{\varphi}{\theta_0}\right)^2\right\}}{r^2}\right]; \tag{6.10}$$

$$P_4 = \frac{P_0}{4}\left[\frac{1}{r_0^2} - \frac{4\exp\left\{-\left(\frac{\varphi}{\theta_0}\right)^2\right\}\cos\Theta}{r_0 r} + \frac{4\exp\left\{-2\left(\frac{\varphi}{\theta_0}\right)^2\right\}}{r^2}\right]. \tag{6.11}$$

For any range r_0, theoretical values of r, φ, and Θ can be worked out by trigonometry and substituted into the above equations to give values for the four powers. These can then be used in equations (3.44) and (3.45) followed by (3.14) and (3.15) to give a calculated range using the approximations. This value can then be compared with r_0 to give an idea of the range error introduced by the approximations.

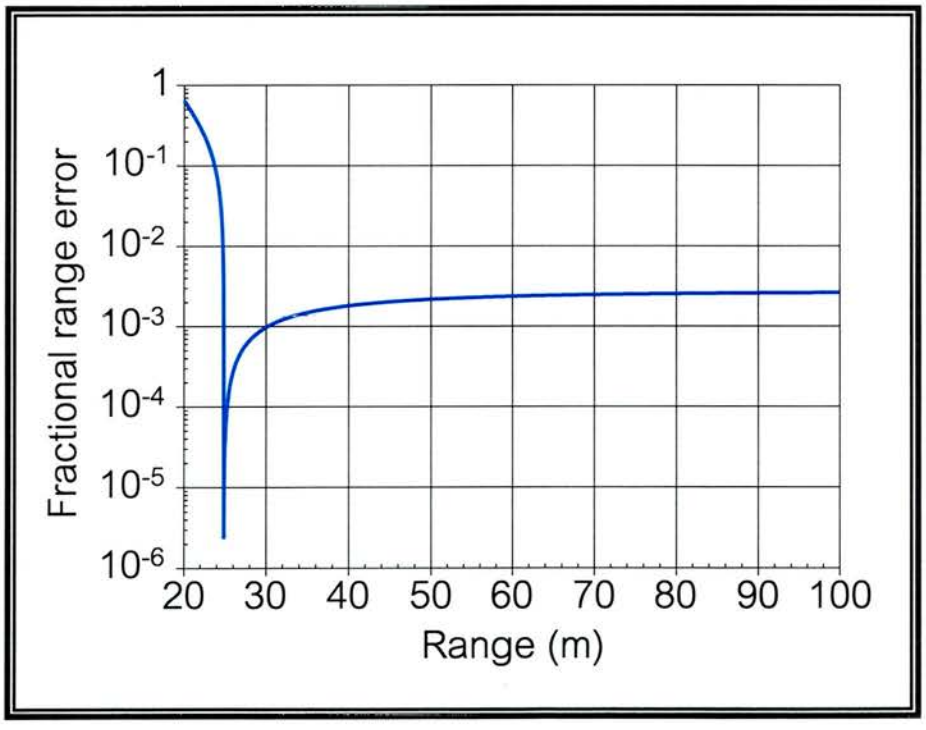

Figure 6.2 A graph of theoretical range error against range

Figure 6.2 shows a graph of the range error against the range. The range error in this case is a fractional error defined as

$$\Delta r = \frac{r - r_0}{r_0}. \tag{6.12}$$

The graph shows clearly that the range error is a minimum (in fact it is zero) at just under 25 metres, after which point it climbs again. Given that P_{rel} can clearly be seen in table 6.1 to be decreasing with range, it seems strange that the range error should be increasing. The explanation lies in the fact that the phase difference Θ, which is the quantity measured by the system, varies non-linearly with range. So, although the error in the received powers decreases with range, the system magnifies these errors at larger ranges.

It is also clear from the graph that the error we are dealing with is very small, only around a quarter of a percent. It is also, in theory at least, a straightforward error to correct for. For ranges above 50 metres certainly, a simple correction factor for all ranges would suffice, leaving the error at less than a tenth of a percent. However, as was discussed in Chapter 4, the errors introduced by the mechanical instability of the system will almost certainly introduce larger errors than that. The assumptions made in the calculations in section 3.2.2 and elsewhere can therefore be considered justifiable, based on these initial calculations.

6.2 Analysis of coupling efficiency

As I mentioned in the last section, the calculations thus far have assumed a point source. This assumption can be made for for two reasons. Firstly, since the beam waist at the feedhorn of the transmitter is small enough to produce a fairly divergent beam, having a θ_0 of about 6°: almost twice as large as the antennas in Setup 2, it can be assumed that all three receiver antennas are well

enough within its beam angle to receive roughly equal powers. Secondly, it is assumed that the angle subtended by the source within the antenna radiation patterns will be small enough for it to appear point like to them. However, for short ranges, this assumption is not necessarily valid. In order to be truly thorough in our analysis therefore, we need to consider the case of an extended source, and therefore the coupling between it and each of the three antennas. Since both the source and antenna can be thought of as part of the same quasi-optical system, I will use a beam coupling analysis for offset beams based on [KOGE64] and [GOLD98], Chapter 4.

Taking the boresight case again, we now have to work out the relative strength of the coupling between the source and the centre port and the source and side ports. This reduces essentially to the problem illustrated schematically in figure 6.3, one of working out the drop in coupling efficiency when two beams are offset laterally.

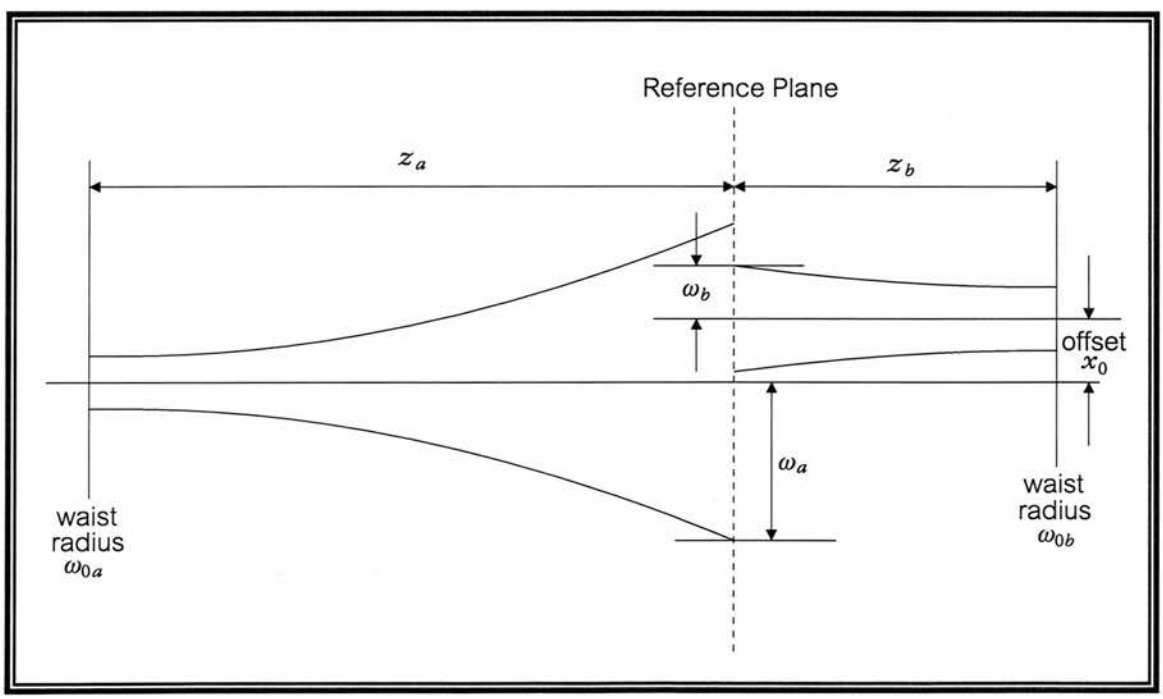

Figure 6.3 Schematic representation of offset Gaussian beams

We can take the offset as applying to either beam. If we assume that the axis of the incoming beam (from the left) is offset from the system axis by an amount x_0, then from [KOGE64] the field distribution of the fundamental mode of the beam is

$$\psi_{a0}(x) = \left(\sqrt{\frac{2}{\pi}}\frac{1}{\omega_a}\right)^{\frac{1}{2}} \exp\left\{-\frac{(x - x_0)^2}{\omega_a} - \frac{2j\pi}{\lambda}\frac{(x - x_0)^2}{2R_a}\right\}, \tag{6.13}$$

where the symbols have their usual meanings. The one dimensional coupling coefficient between the two beams is defined as

$$c_{ab} = \int_{-\infty}^{+\infty} \psi_a(x)\,\psi_b^*(x)\,dx, \tag{6.14}$$

which for the fundamental modes yields

$$c_{x_0} = \left(\frac{2}{\pi\omega_a\omega_b}\right)^{\frac{1}{2}} \int_{-\infty}^{+\infty} \exp -\left\{\frac{(x - x_0)^2}{\omega_a^2} + \frac{x^2}{\omega_b^2} + \frac{j\pi}{\lambda}\left[\frac{(x - x_0)^2}{R_a} - \frac{x^2}{R_b}\right]\right\} dx. \tag{6.15}$$

Substituting the complex beam parameter

$$q = \frac{1}{R} - \frac{j\pi}{\lambda\omega^2},$$

and rearranging the exponential into a form where it can be integrated using the relation

$$\int_{-\infty}^{+\infty} \exp\{-ax^2 + bx\}dx = \left(\frac{\pi}{a}\right)^{\frac{1}{2}} \exp\left\{\frac{b^2}{4a}\right\}, \tag{6.16}$$

we obtain

$$c_{x_0} = \left(\frac{2}{\pi\omega_a\omega_b}\right)^{\frac{1}{2}} \int_{-\infty}^{+\infty} \exp -\left\{\frac{j\pi}{\lambda}\left(\frac{1}{q_a^*} - \frac{1}{q_b}\right)x^2 + \frac{2j\pi x x_0}{\lambda q_b} - \frac{j\lambda x_0^2}{\lambda q_b}\right\} dx, \quad (6.17)$$

which yields

$$\begin{aligned} c_{x_0} &= \left[\frac{2j\lambda}{\pi\omega_a\omega_b(1/q_a^* - 1/q_b)}\right]^{\frac{1}{2}} \exp\left\{\frac{j\pi x_0^2}{\lambda(q_a^* - q_b)}\right\}; \\ &= c_{00} \exp\left\{\frac{j\pi x_0^2}{\lambda(q_a^* - q_b)}\right\}, \end{aligned} \quad (6.18)$$

where c_{00} is the coupling coefficient for the fundamental modes of two axially aligned beams [KOGE64] and is equal to the square bracket term. Taking the offset as being lateral only, the fractional power coupled between the modes is the product of the magnitude squared of the coefficients in both directions and is therefore

$$\kappa_{x_0} = |c_{x_0}|^2 \cdot |c_{00}|^2; \quad (6.19)$$

$$= \kappa \cdot \left|\exp\left\{\frac{j\pi x_0^2}{\lambda(q_a^* - q_b)}\right\}\right|^2, \quad (6.20)$$

where κ is the on-axis power coupling coefficient. We can get the equation in a more usable form by taking the other expression for the complex beam parameter

$$q = \frac{j\pi\omega_0^2}{\lambda} + z,$$

and using it to evaluate the mod-square of the exponential in (6.20). We simplify further when we take the reference plane at the receiver antenna, since we can say that $z_b = 0$. What we are interested in is the power loss at the side ports relative to the centre port. This is the fractional power coupling loss due to the offset x_0 and is

$$\kappa'_{x_0} = \frac{\kappa_{x_0}}{\kappa} = \exp\left\{\frac{-2x_0(\omega_{0a}^2 + \omega_{0b}^2)}{(\omega_{0a}^2 + \omega_{0b}^2) + (\lambda z/\pi)^2}\right\}, \qquad (6.21)$$

where $z = z_a$. Substituting in values for the beam waists, where ω_{0a} is the source feedhorn beam waist of 10mm and ω_{0b} is the receiver antenna beam waist of 18mm (Setup 2), we can calculate the power loss at any distance of the receiver from the source. The table 6.2 below shows the fractional power coupling loss at the same ranges as in table 6.1. Also included in the table is a column showing the difference in the relative powers calculated in this section and the last.

range z	κ'_{x_0}	$P_{rel} - \kappa'_{x_0}$
10m	0.720	0.057
20m	0.921	0.018
30m	0.964	0.008
40m	0.980	0.005
50m	0.987	0.003
75m	0.994	0.001
100m	0.997	0.001
200m	0.999	0.000
500m	1.000	0.000

Table 6.2 Fractional power reaching outer ports relative to centre port calculated using equation (6.21) for Setup 2. The difference between these values and the values calculated previously is also shown for reference

The table shows that the assumption of a point source is valid for most ranges, and as with the calculations in the previous section, it is only at the shortest

ranges that we will experience any major disagreement between theory and results.

6.3 Conclusion on validity of approximations

FOR THE purposes of this work, the assumptions made in section 3.2.2 regarding equal received powers at all three ports can be considered justified. Since the aim was to produce a system that would be used mostly in the far field, in other words at ranges of a few hundred times the port spacing, this aim can be adequately fulfilled making this approximation.

However, these calculations have shown that at short ranges, it is not valid to assume that all three antennas receive equal powers. If we are making short range measurements therefore, we need to be mindful of this, either making adjustments in the calculations, or treating the results with less confidence.

Chapter 7
Theory and Experiment II

In this chapter I will compare theory with extensive experimental results taken using the experimental setup described in Chapter 5.

7.1 Preliminary tests of the setup

The experimental setup was as described in Chapter 5. The experiments were performed with the receiver in the laboratory, pointing out of an open window. The source was taken into the field in front of the laboratory in its shielding box and placed on the platform. Initially, the system was tested with the source at a distance of about 30m.

7.1.1 Antenna pattern measurements

The first measurements carried out were of the antenna patterns of the three ports. The antenna pattern of each port was taken in turn by covering the mirrors behind the other two ports with ecosorb. The total power arriving at the four detectors was therefore the power received by the port being examined.

Measurements of this received power were taken every 10 minutes of arc for about four degrees either side of boresight. The results for two different days are shown in figure 7.1 below. As can be seen, the antenna patterns are essentially the same for the two different days, indicating the stability of the system. The only difference is in the total and the relative powers received by the different ports, and this is almost certainly due to fluctuations in the

transmitted power: since a set of measurements could easily take half an hour per port, the transmitted power could change significantly over this period.

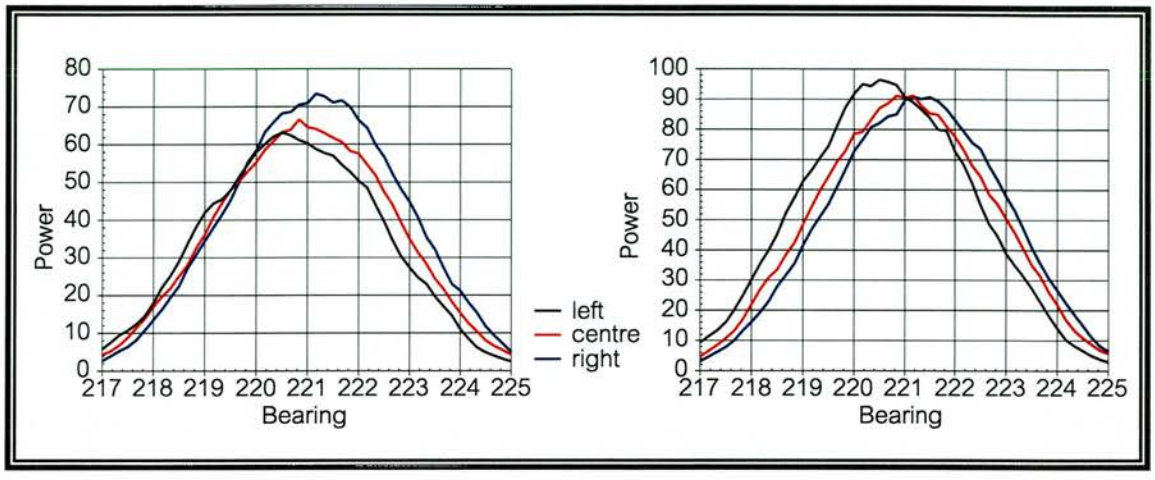

Figure 7.1 A pair of graphs showing antenna pattern measurements taken on two different days. The bearing and power are both relative measurements, and as such absolute values are not important

The important thing to note in these plots is the constant position and separation of the maxima of the patterns of the three antennas. On both days, the left port has its pattern centred at about 220.5°, the centre port at 220.9° and the right at 221.3°. This tells us two things. Firstly, that the setup is rigid enough that the directions of the antennas do not change from day to day. Secondly, the equal angular separation of the maxima indicates that the port lenses are indeed lined up in a plane, all pointing the same way. While working with the previous system, I had found the positions to vary considerably from day to day, to such an extent that the maximum of the centre port was often outside that of one of the side ports, a manifestation of the port squinting present.

7.1.2 Two port interferogram

HAVING MEASURED the antenna patterns, I decided to measure the 2-port interferogram that would be produced by blocking off only the centre port. This should show clearly the sensitivity to bearing of the system, and enable a more accurate estimation of the position of boresight than from the antenna patterns alone. Essentially, without the centre port being used, we have the simple direction finder described in section 1.3.2, and we should therefore expect the characteristic interference fringes associated with such a system.

Referring back to figure 3.2 showing the quasi-optical circuit and using the matrix method outlined in section 3.2.2, we can get an idea of what the interferogram should look like.

The modified expressions for the fields arriving at the four power detectors will be

$$O_1 = N_T H_T S; \tag{7.1}$$

$$O_2 = N_R H_T S; \tag{7.2}$$

$$O_3 = P_R H_R S; \tag{7.3}$$

$$O_4 = P_T H_R S; \tag{7.4}$$

where

$$S = P_T M N_T E_2 + N_R M N_T E_1, \tag{7.5}$$

as before. This gives essentially a simplified version of the three port solution

$$O_1, O_2 = \frac{1}{4}\begin{pmatrix} 1 & 1 \\ 1 & 1 \end{pmatrix}[\pm E_1 \mp E_2]; \tag{7.6}$$

$$O_3, O_4 = \frac{1}{4}\begin{pmatrix} -1 & -1 \\ 1 & 1 \end{pmatrix}[E_1 + E_2], \tag{7.7}$$

showing that the 2-port setup gives us the difference of the two incoming signals at detectors 1 and 2, and the sum at ports 3 and 4, as expected. By solving the equations in a similar way to that described in chapter 3, we obtain

$$P_1 , P_2 = \frac{P_0}{4r^2} \exp\left\{-2\left(\frac{\varphi}{\theta_0}\right)^2\right\}[1 - \cos(2\Theta)]; \tag{7.8}$$

$$P_3 , P_4 = \frac{P_0}{4r^2} \exp\left\{-2\left(\frac{\varphi}{\theta_0}\right)^2\right\}[1 + \cos(2\Theta)], \tag{7.9}$$

where $2\Theta = \Theta_2 - \Theta_1$, since for the 2-port case we can assume that $\Theta_1 = -\Theta_2$. We can see from this that we expect P_1 and P_2 to be minimum on boresight (when $\Theta = 0$) and P_3 and P_4 to be maximum.

The interferogram was taken in a similar way to the antenna pattern measurements, with the source at a range of 30m, except that the powers were measured every 5 minutes of arc, since a finer resolution was required to get enough points per cycle.

The two port interferogram is shown in figure 7.2. It can be seen that the pattern is very close to what would be expected by theory. The space between maxima for each detector can be determined by counting the peaks between 220° and 222° and can be seen to be 0.44°. The expected value would be the maximum unambiguous FOV given in Chapter 1 as

$$\theta_{unamb} = 2 \sin^{-1}\left(\frac{\lambda}{2d}\right),$$

which for the setup here gives a value of 0.43°, very close to the experimental value. The irregular shape of the pattern is more due to the undersampling of bearing, rather than any real irregularity.

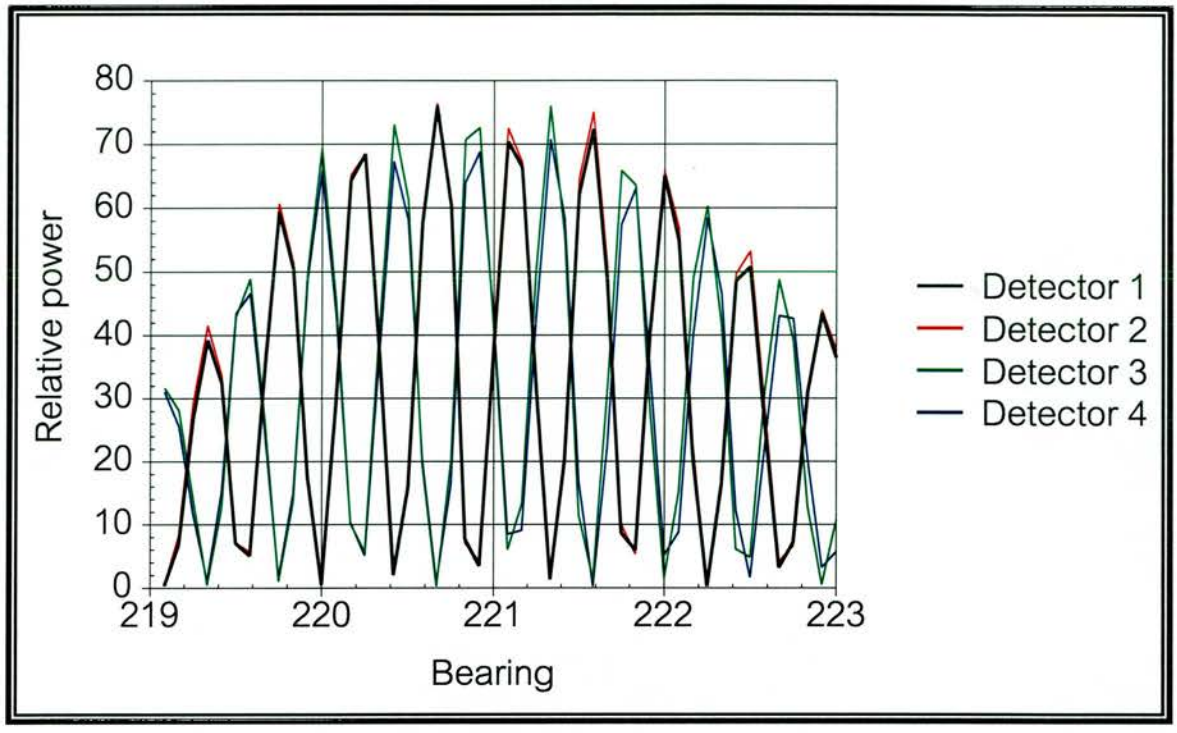

Figure 7.2 Two port interferogram

At this point I used the results from the two port interferogram and the antenna patterns to line a gun sight up with the boresight of the receiver in order to make it easier to find when doing future experiments. The gun sight was mounted on the primary base plate, roughly in line with the boresight. The mount used was tall enough for the sight to be above the level of the half cubes on the secondary plates, and was adjustable in three dimensions, to allow accurate positioning of the sight. To line the sight up I made a mark on the outside of the transmitter box corresponding to the position of the feedhorn inside. I then found the boresight using the interferogram by looking for the point nearest the centre of the antenna patterns where the powers at receivers 1 and 2 were a minimum while the levels at receivers 3 and 4 were maximum. I then simply lined up the crosshair of the sight with the mark on the box. To make sure that the sight was indeed properly lined up, I found boresight in the same way at two more ranges, making sure that the crosshair was still located over the mark on the box. Once I was satisfied, I fixed the sight in position.

7.1.3 Three port interferogram

IN ADDITION to the two port pattern, I also took an interferogram with all three ports uncovered. This is of course the way in which the system will ultimately be used, but a preliminary test is useful to establish that the system is working as expected before more extensive testing is undertaken. The pattern taken is shown in figure 7.3. Unlike the two port pattern, the exact shape of this interferogram is dependent on range, as well as bearing. How well the theory behind this corresponds to experimental results is the subject of section 7.4.

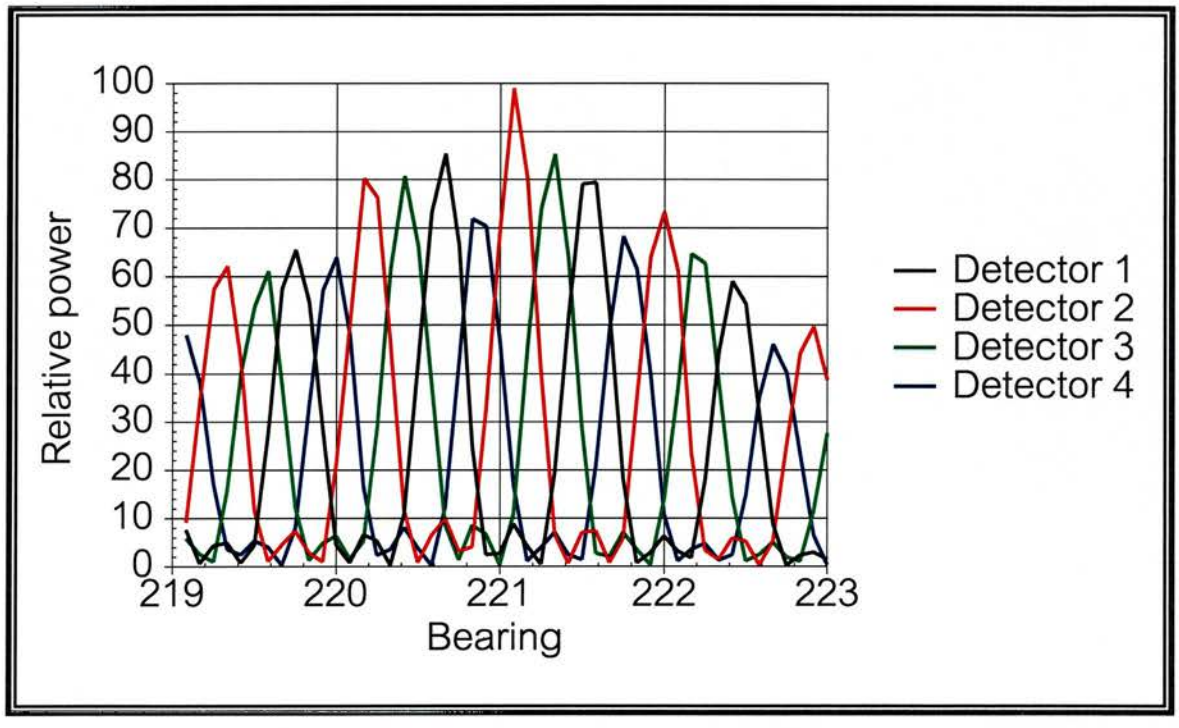

Figure 7.3 Three port interferogram

From both the two port and three port interferograms we can see that the patterns are a superimposition of the interferograms themselves and the antenna patterns of the ports. In much of the analysis that follows later in the chapter, I will be ignoring the contribution of the antenna patterns to the received power levels. The justification for this approach has already been dealt with in more depth in the previous chapter.

7.2 Experimental procedure

THE SETUP used in the following data acquisition was the same as that used in the previous section. The platform was taken to a variety of ranges. The transmitter-receiver distance was measured using a tape measure, providing an accurate enough figure for these experiments. To aid accuracy and repeatability, lines were painted on the grass at regular distances. Although this method is clearly not as accurate as the laser range finder used in the original experiments, I would estimate that it gave an error of no more than a few tenths of a percent.

Before the transmitter was taken into the field, the Gunn oscillator was switched on in the lab in order to allow it to warm up fully and stabilise, since the frequency and power of an oscillator can drift slightly after being switched on. The frequency was also checked in the lab, using a spectrum analyser. The radiometers are sensitive enough that the receiver doesn't need to be pointed at the source for it to detect a signal in the lab, so I would just reflect some of the source power off the window in front of the receiver to carry out the following part of the setup. The crystal detector was removed temporarily from one of the channels, and the output i.f. was fed to the analyser. Since, as mentioned in Chapter 5, the local oscillators had a frequency of 94GHz, the choke of the oscillator would then be adjusted to give an output of 1.0GHz meaning that the oscillator was at the required 95GHz. However, care would be taken to make sure that this frequency rose as the choke was wound in, and fell as it was wound out, in order to make sure that the oscillator hadn't been inadvertently tuned to 93GHz. Once I was satisfied with the source setup, the box would be taken into the field and the crystal detector replaced on the i.f. chain.

Once on the platform at each range, it was necessary to check that a suitable amount of power was being received. The data acquisition card can accept 10V peak to peak, so a scope was connected to each of the four outputs of the pre-

amp box in turn to make sure that the largest voltage (usually on channel 4) was somewhere between 6Vpp and 9Vpp. It would sometimes be necessary to go out again and adjust the attenuator on the front of the oscillator in order to obtain a desirable output level.

7.2.1 Initial measurements

INITIALLY, I took a set of measurements at ranges from 50m to 100m in steps of 10m. At each range I set up the platform with the transmitter as described above and then used the !Ranging program to take a set of power levels. I set the program to take 500 grabs, each time taking 16k samples and using the PSD routine to calculate a voltage value. This was converted to the power value which was finally saved to file. I would therefore end up with a file for each range, containing 500 lines of four power values.

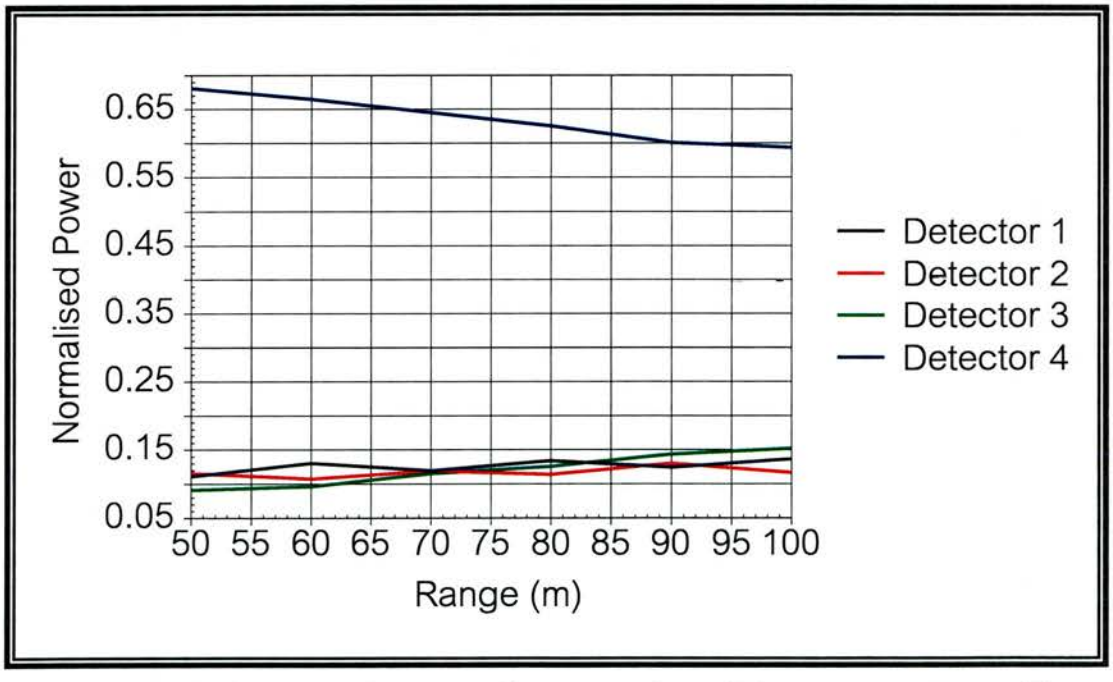

Figure 7.4 Graph showing first results of the new setup. The normalised powers received at the four detectors are shown plotted against range.

To plot the data, I found the average for each of the four powers at the

different ranges. I then normalised the values by dividing by the sum of the powers at each range. The graph obtained from these preliminary results is shown above in figure 7.4.

The shape of the graph looks encouraging, in that a clear fall in power with range can be seen for detector 4 (in blue) while the power at detector 3 (in green) rises by a similar amount, indicating that the system is indeed sensitive to range as intended.

7.2.2 Main experimental run

AFTER THE results of the initial measurements had been looked at, I decided to take a more comprehensive set of data, to test the theory much more thoroughly. I initially decided to take measurements from a range of 25m out to 85m, first every 2.5m to 40m, then at 43m, 46m and 50m, and lastly every 5m. I later decided to take measurements at three more ranges down to 15m. The reason for this was to try and cover the maximum and minimum values of P4 and P3 respectively as they change with range. As was discussed in the previous chapter though, we should not expect these measurements to be conform to the theory quite as well, since the theory makes no allowances for the port antenna patterns: something which will have a small effect at these very short ranges. In taking measurements close in however, we should be able to get a better idea of exactly where the limitations of the theory lie.

At each range I took measurements at a set of bearings from -10 to +10 minutes of arc at 2 arc minute intervals. In order to save time, since I was taking eleven sets of measurements instead of one at each range, I reduced the number of data runs from 500 to 100, taking the average in the same way as before.

7.3 Main experimental results

In this section I will simply be presenting the results for the four detectors at the ranges and bearings mentioned at the end of the previous section. Analysis of these results and comparison with theory will be done in section 7.4. In order to give the most meaningful representation of the results, I decided to graph them as surface plots for each channel, with power on the vertical (z) axis and range and bearing as the x and y axes.

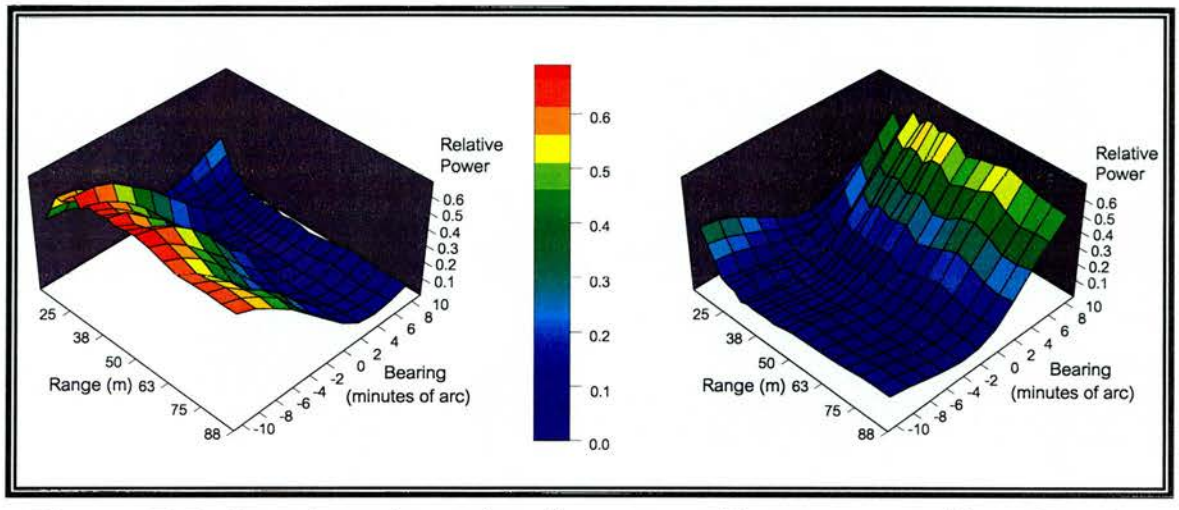

Figure 7.5 Graphs of received power with range and bearing for detectors one and two

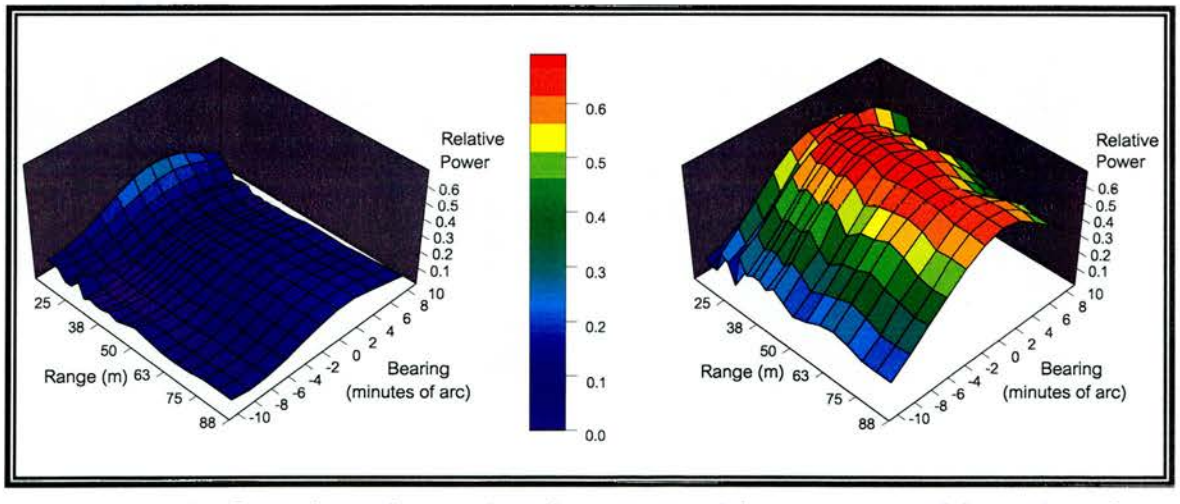

Figure 7.6 Graphs of received power with range and bearing for detectors three and four

As before, I took the average of the power values obtained from the data runs at each range and bearing. The values for the four channels were then normalised by dividing by the sum of the powers at each individual range and bearing coordinate. These final values were put into the form of a 2-D matrix of power values with range going down the columns and bearing across the rows. All this was accomplished by writing a small program in C to read the data files, process the values and save the final four matrix files. The final matrices for each channel were fed into Transform 3D on the PC, which I used to plot four surfaces.

A cursory glance at the figures shows up a couple of problems with this representation of the results, which I will deal with in more depth in the following sections. It can be noticed that the centre of the patterns doesn't quite line up with the centre of the graphs. This is probably due to a misalignment of the gunsight referred to previously. Although I had taken care to align it along the boresight of the receiver, it may have got knocked since, therefore skewing the results by a couple of minutes of arc. In addition to this, it can be seen that at different ranges, the amount of misalignment appears to vary slightly, presumably due to the difficulty with lining the sight up with the transmitter to better than one arc minute or so. In fitting the theory to the results therefore, these misalignments will need to be taken into account and corrected for.

7.4 Analysis of results and comparison with theory

In the next couple of sections I will compare the results shown in the previous section with predicted theoretical values obtained using the equations derived in Chapter 3. First I shall look at the general behaviour of the results with both range and bearing, and show that there is a general agreement with the theory, providing the phase offset term $\Delta\Theta$, mentioned in previous chapters, is introduced. Then I shall try and find a value for this term by using a simple

least squares fit for the data.

The theoretical data for the graphs and the fitting procedures in the following sections were calculated as follows. We refer back to equations (3.12) and (3.13)

$$(r \sin\phi - X)^2 + (r \cos\phi)^2 = (r + \lambda\Theta_1)^2; \tag{3.12}$$

$$(r \sin\phi + X)^2 + (r \cos\phi)^2 = (r + \lambda\Theta_2)^2. \tag{3.13}$$

and instead of solving for range r and bearing ϕ, we rearrange the equations to give expressions for Θ_1 and Θ_2

$$\Theta_1 = \frac{1}{\lambda}\left(\sqrt{(r \sin\phi - X)^2 + (r \cos\phi)^2} - r\right); \tag{7.10}$$

$$\Theta_2 = \frac{1}{\lambda}\left(\sqrt{(r \sin\phi + X)^2 + (r \cos\phi)^2} - r\right), \tag{7.11}$$

which on simplification become

$$\Theta_1 = \frac{1}{\lambda}\left(\sqrt{r^2 - 2rX \sin\phi + X^2} - r\right); \tag{7.12}$$

$$\Theta_2 = \frac{1}{\lambda}\left(\sqrt{r^2 + 2rX \sin\phi + X^2} - r\right). \tag{7.13}$$

The negative square root has been ignored as meaningless in this context. As an aside, we note that the change of phase with bearing is in fact a nearly linear relationship, as can be seen by expanding the square root term using the binomial expansion for $\sin\phi$, the first two terms of which give

$$\Theta_1 = \frac{1}{\lambda}\left(\sqrt{r^2 + X^2} - \frac{1}{2}\sqrt{\frac{2rX}{r^2 + X^2}} \sin\phi - r\right). \tag{7.14}$$

$$\Theta_2 = \frac{1}{\lambda}\left(\sqrt{r^2 + X^2} + \frac{1}{2}\sqrt{\frac{2rX}{r^2 + X^2}} \sin\phi - r\right). \tag{7.15}$$

The first and third terms in each bracket combine to give a small positive value which confirms that the phases are not zero at zero bearing. The sine term provides the nearly linear relationship, since for small ϕ, $\sin\phi \approx \phi$.

The theoretical power values are obtained by taking the phase values calculated in equations (7.12) and (7.13), and substituting them into equations (3.38-41). I wrote a C routine to do this, in which I could specify the ranges and bearings at which I wished to calculate the four power values.

7.4.1 Behaviour with bearing

A CHANGE in bearing will manifest itself most clearly in changes in the powers at detectors one and two. This can be seen from equations (3.38) and (3.39) (recalled below), by considering how the phase differences Θ_1 and Θ_2 vary with bearing.

$$P_1 = \frac{P_0}{4r^2}\exp\left\{-2\left(\frac{\varphi}{\theta_0}\right)^2\right\}\left[3 + 2\sin\Theta_1 - 2\sin\Theta_2 - 2\cos\Theta_1\cos\Theta_2 - 2\sin\Theta_1\sin\Theta_2\right]; \quad (3.38)$$

$$P_2 = \frac{P_0}{4r^2}\exp\left\{-2\left(\frac{\varphi}{\theta_0}\right)^2\right\}\left[3 - 2\sin\Theta_1 + 2\sin\Theta_2 - 2\cos\Theta_1\cos\Theta_2 - 2\sin\Theta_1\sin\Theta_2\right]; \quad (3.39)$$

On boresight, they will be equal, and as the source is moved to one side, one of the phase differences will rise, and the other will fall. Looking at equations (3.38) and (3.39) therefore, we can see that the first two sine terms in these equations will serve to magnify this effect, since they have opposite signs. The other two terms are the equivalent of $2\cos(\Theta_1 - \Theta_2)$, which in this case will remain constant, since at any one range the difference of the two phases will not change. Both the P_1 and P_2 values will show asymmetric behaviour about boresight, as is evident from looking at the first two terms again, hence they contain the bearing information. The powers at detectors three and four, calculated in equations (3.40) and (3.41),

$$P_3 = \frac{P_0}{4r^2}\exp\left\{-2\left(\frac{\varphi}{\theta_0}\right)^2\right\}\left[3 + 2\cos\Theta_1 + 2\cos\Theta_2 + 2\cos\Theta_1\cos\Theta_2 + 2\sin\Theta_1\sin\Theta_2\right]; \quad (3.40)$$

$$P_4 = \frac{P_0}{4r^2}\exp\left\{-2\left(\frac{\varphi}{\theta_0}\right)^2\right\}\left[3 - 2\cos\Theta_1 - 2\cos\Theta_2 + 2\cos\Theta_1\cos\Theta_2 + 2\sin\Theta_1\sin\Theta_2\right]. \quad (3.41)$$

will also vary with bearing, but this variation will be symmetrical about boresight, and will therefore not provide as much useful bearing information. We can see that this will be the case because the first two terms in each equation are cosines and are therefore even functions.

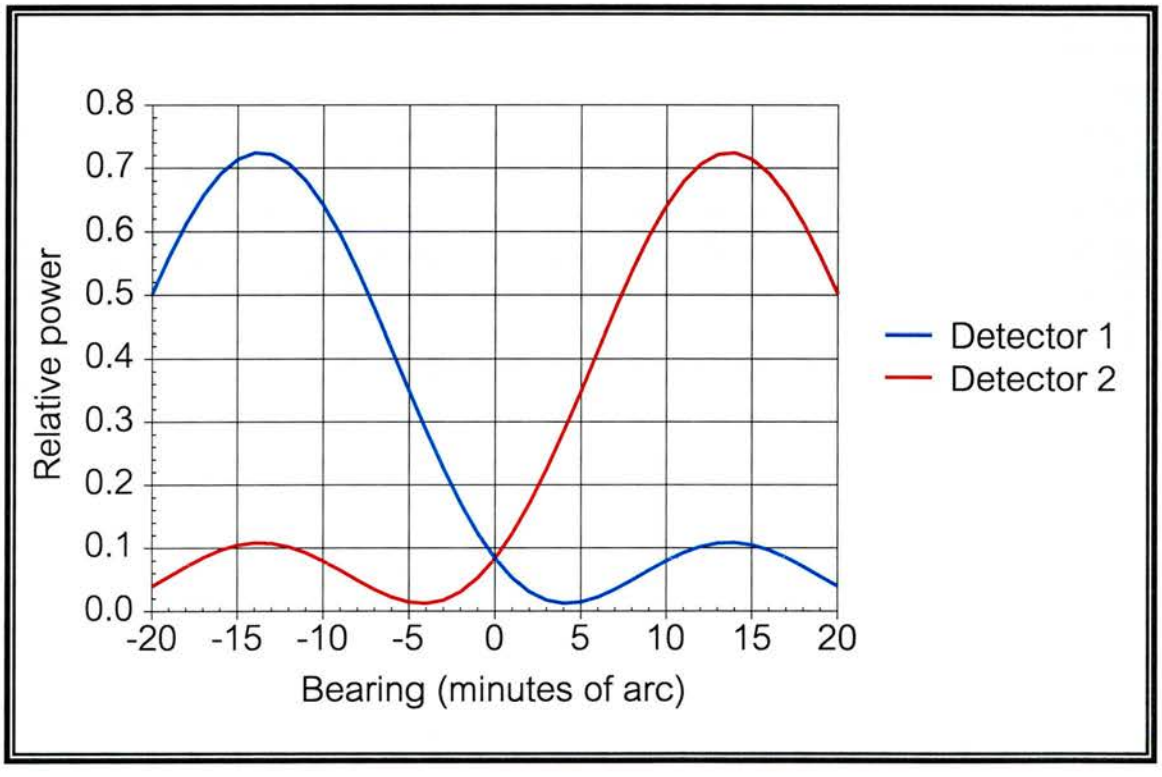

Figure 7.7 Graph showing theoretical detector behaviour with bearing for detectors one and two at a range of 50m

When using these equations to calculate the theoretical power values, we need the normalised values, in order to be able to relate them clearly to the real results. It is simplest if we just ignore the part outside the square brackets in the above equations (which is identical for all four powers), and then divide

each power by the sum of all four powers, which can be seen to be 12, since all the sine and cosine terms of course cancel.

A graph of the theoretical behaviour of the powers at detectors one and two for a range of 50m is shown in figure 7.7 on the previous page. I have included bearings between -20 and +20 minutes of arc in order to better show the structure of the grating lobes.

Due to the presence of the extra port in this setup and the fact that we are not assuming an infinite source-receiver distance, the expression for the maximum unambiguous field of view will be slightly different from that given in equation (1.6). However, as we shall see, for ranges of over 30 or 40 metres this difference will be minimal, so we can be confident of a claim of a more or less range-independent θ_{unamb} of 0°13′ for this particular port spacing.

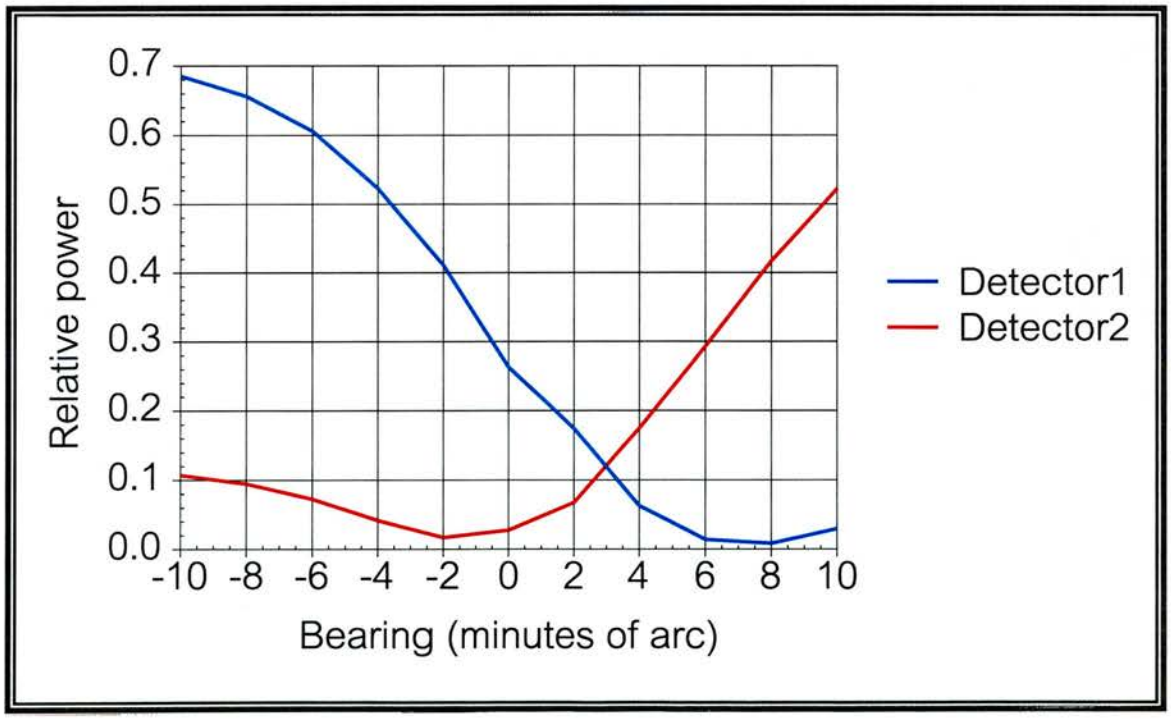

Figure 7.8 Graph showing actual detector behaviour with bearing for detectors one and two at a range of 50m

13 arc minutes is of course a very narrow field of view, and is one of the current limitations of this particular setup.

If we now look at the actual data from the system for the range of 50m, we get the graph in figure 7.8, for the powers at detectors 1 and 2.

The graph in figure 7.8 is clearly of the same overall shape as the one in 7.7, but with one slight difference. We can now notice more clearly the bearing offset to which I referred at the end of the previous section, which in this case appears to be about 3 minutes of arc. Although it looks quite significant on this graph, it is worth noting that the turntable used for angling the receiver relative to the source had a scale that only went to one minute of arc.

The other important feature to note is that although the shapes of the lines in both graphs are essentially the same, the slope of the data graph is slightly shallower than that of the theoretical curve. This effect is due to the phase offsets inherently present in the system, referred to at the beginning of this section.

In order to look more closely at these effects, we need to modify the modelling equations to include both the bearing offset and the phase offsets. Adding a bearing correction term to equations (7.12) and (7.13) we get

$$\Theta_1 = \frac{1}{\lambda}\left(\sqrt{r^2 - 2rX\sin(\phi + \Delta\phi) + X^2} - r\right); \qquad (7.16)$$

$$\Theta_2 = \frac{1}{\lambda}\left(\sqrt{r^2 + 2rX\sin(\phi + \Delta\phi) + X^2} - r\right), \qquad (7.17)$$

where $\Delta\phi$ is the bearing offset in radians. With the introduction of the phase offset term $\Delta\Theta$, the four equations for the theoretical powers become

$$P_1 = [3 + 2\sin(\Theta_1 + \Delta\Theta) - 2\sin(\Theta_2 + \Delta\Theta) - 2\cos(\Theta_1 + \Delta\Theta)\cos(\Theta_2 + \Delta\Theta) - 2\sin(\Theta_1 + \Delta\Theta)\sin(\Theta_2 + \Delta\Theta)]/12; \quad (7.18)$$

$$P_2 = [3 - 2\sin(\Theta_1 + \Delta\Theta) + 2\sin(\Theta_2 + \Delta\Theta) - 2\cos(\Theta_1 + \Delta\Theta)\cos(\Theta_2 + \Delta\Theta) - 2\sin(\Theta_1 + \Delta\Theta)\sin(\Theta_2 + \Delta\Theta)]/12; \quad (7.19)$$

$$P_3 = [3 + 2\cos(\Theta_1 + \Delta\Theta) + 2\cos(\Theta_2 + \Delta\Theta) + 2\cos(\Theta_1 + \Delta\Theta)\cos(\Theta_2 + \Delta\Theta) + 2\sin(\Theta_1 + \Delta\Theta)\sin(\Theta_2 + \Delta\Theta)]/12; \quad (7.20)$$

$$P_4 = [3 - 2\cos(\Theta_1 + \Delta\Theta) - 2\cos(\Theta_2 + \Delta\Theta) + 2\cos(\Theta_1 + \Delta\Theta)\cos(\Theta_2 + \Delta\Theta) + 2\sin(\Theta_1 + \Delta\Theta)\sin(\Theta_2 + \Delta\Theta)]/12, \quad (7.21)$$

where I have omitted the factor outside the square brackets and divided by the normalising power sum 12.

By choosing different values for $\Delta\phi$ and $\Delta\Theta$, we can see how the introduction of these terms changes the shape of the graphs of the power values, and can try and find values which fit the theory to the data.

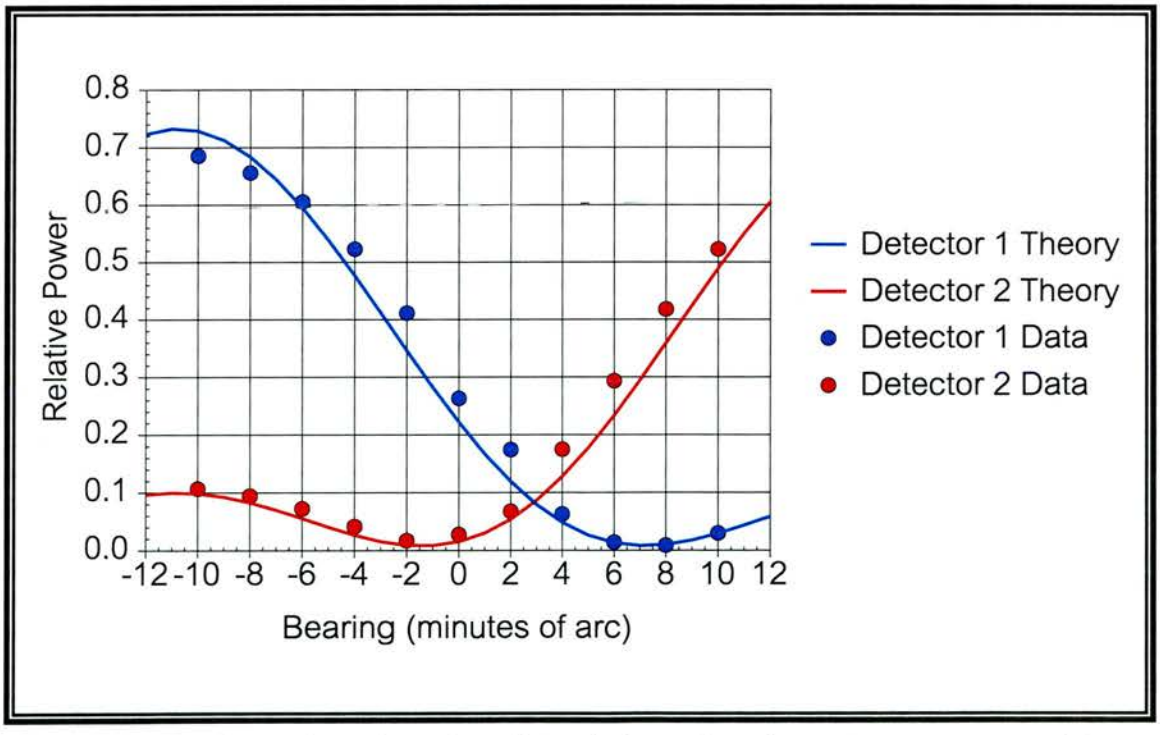

Figure 7.9 Graphs showing fitted data for detectors one and two for a range of 50m incorporating a phase offset of -1 rad.

In figure 7.9, I have plotted a graph of the received powers against bearing for both the real data and theoretical values at a range of 50m. I have set the bearing offset $\Delta\phi = -2.9$ minutes of arc, in order to line up the centres of the two patterns. Heuristically, a phase offset of $\Delta\Theta = -1$ radians seems to provide a good fit for powers 1 and 2 at this range, at least.

7.4.2 Theoretical behaviour with range

JUST AS bearing behaviour manifests itself most clearly in the values of the powers at detectors one and two, so range behaviour is shown up best by looking at detectors three and four. In fact, if we consider the boresight case, where $\Theta_1 = \Theta_2$, then equations (3.38) to (3.41) simplify to

$$P_1 = \frac{1}{12}; \tag{7.22}$$

$$P_2 = \frac{1}{12}; \tag{7.23}$$

$$P_3 = \frac{1}{12}[5 + 4\cos\Theta]; \tag{7.24}$$

$$P_4 = \frac{1}{12}[5 - 4\cos\Theta], \tag{7.25}$$

where I have normalised the four powers as in the last section. It can be seen from these equations that P_1 and P_2 will remain unchanged relative to the total power at any range. It can also be seen that P_3 and P_4 will be symmetric about one value. This is illustrated by the graph in figure 7.10 on the next page.

Let us now look at the data for detectors 3 and 4, and compare this with the calculated curves. In plotting the graphs in figure 7.11, I have chosen to use the data for the bearing of 2 minutes of arc, since because of the bearing offset that has crept into the measurements, this will be closer to the real boresight of the instrument. Although the amount of offset will be different for different ranges, as I pointed out previously, most of the measurements seem to be offset

by between 1 and 3 minutes of arc, so 2 minutes of arc provides a good enough approximation for these initial comparisons between theory and data.

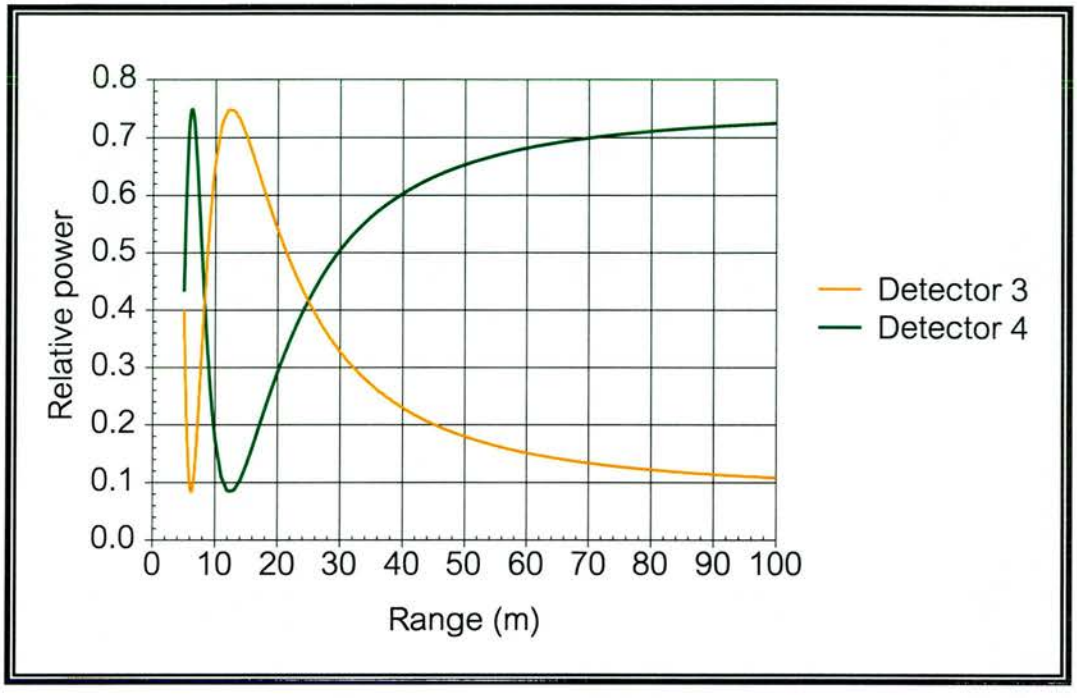

Figure 7.10 Graph showing theoretical detector behaviour with range for detectors three and four on boresight

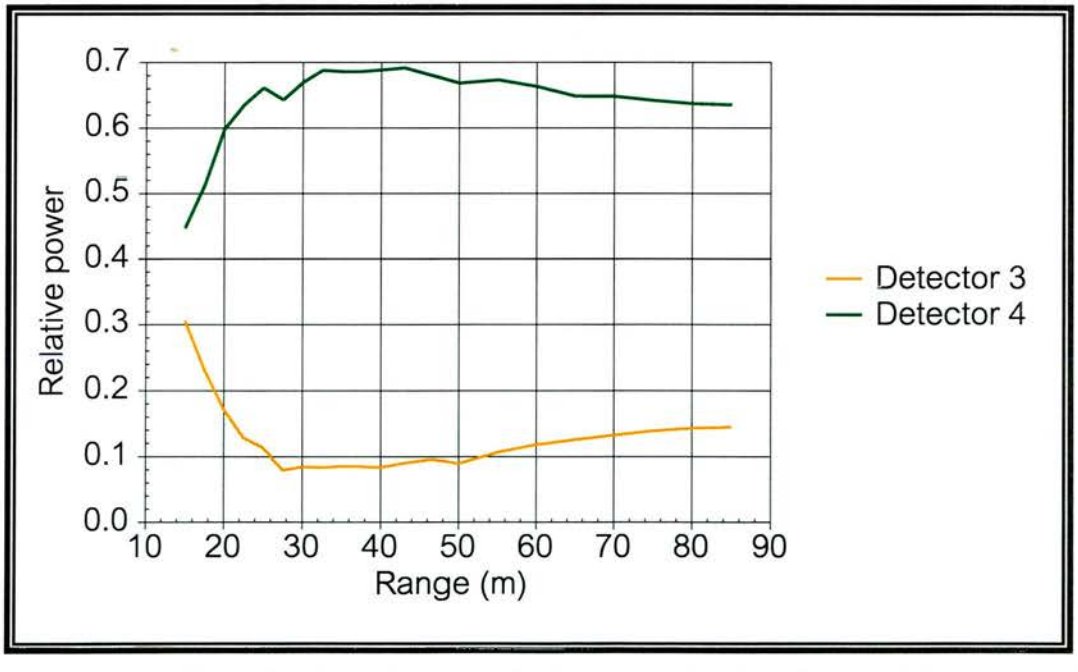

Figure 7.11 Graph showing real detector behaviour with range for detectors three and four

Looking at figure 7.11, we can see that although the received powers are symmetric about a value as we would expect, they are clearly not of the same shape as the curves in figure 7.10. Once again though, this effect is due to the presence of the phase offset within the system. To illustrate the effect that the presence of different offsets would have on the output at detectors 3 and 4, I have plotted graphs in figure 7.12 which show the theoretical received power at detectors three and four for phase offsets of zero, $\pi / 2$, and π. Negative phase offsets will produce curves which are the mirror image of the ones shown.

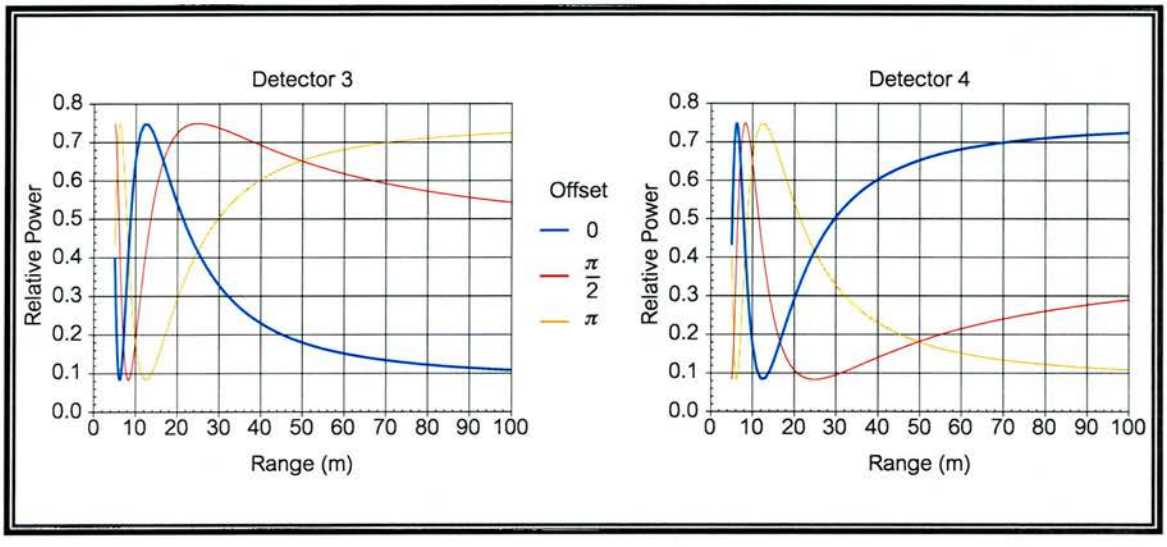

Figure 7.12 Theoretical received powers at detectors three and four for different values of phase offset

It can be seen quite clearly from these graphs that the phase offset term "stretches" the curve along the x axis, with the maximum or minimum values of the two power values appearing at different ranges for different phase offset values. This is of some importance when considering how the instrument will be used for ranging on an object. Obviously, at the point where the curves are flattest, a given change in phase will have a greater effect on the calculated value of the range than it will at ranges where the curves are steeper. This is important because it affects the range error and therefore the tolerance of the instrument. The largest range error will still be at infinite range, but if the

minimum / maximum point is far enough out in range, the curve will be flat enough that the range error is also significant at that distance also. What this means in practice is that if we want accurate measurements at a certain range, we need to make sure that it doesn't correspond to this "flat" point. In this particular instrument, we can see from the graph in figure 7.11 that the range error will be larger at ranges around 35 - 40m where the minimum and maximum points of the graphs occur. We would therefore not expect to get such accurate results for ranges around those values. Conversely, it can also be argued that there is an optimum offset for measuring any given range. This is the offset value that would give the largest gradient in powers three and four at the range being measured.

Including the phase offset in the calculations allows us to get a fairly decent fit for the results. In figure 7.13 I have plotted a graph showing the theoretical curves of powers 3 and 4 along with the real data for the two powers.

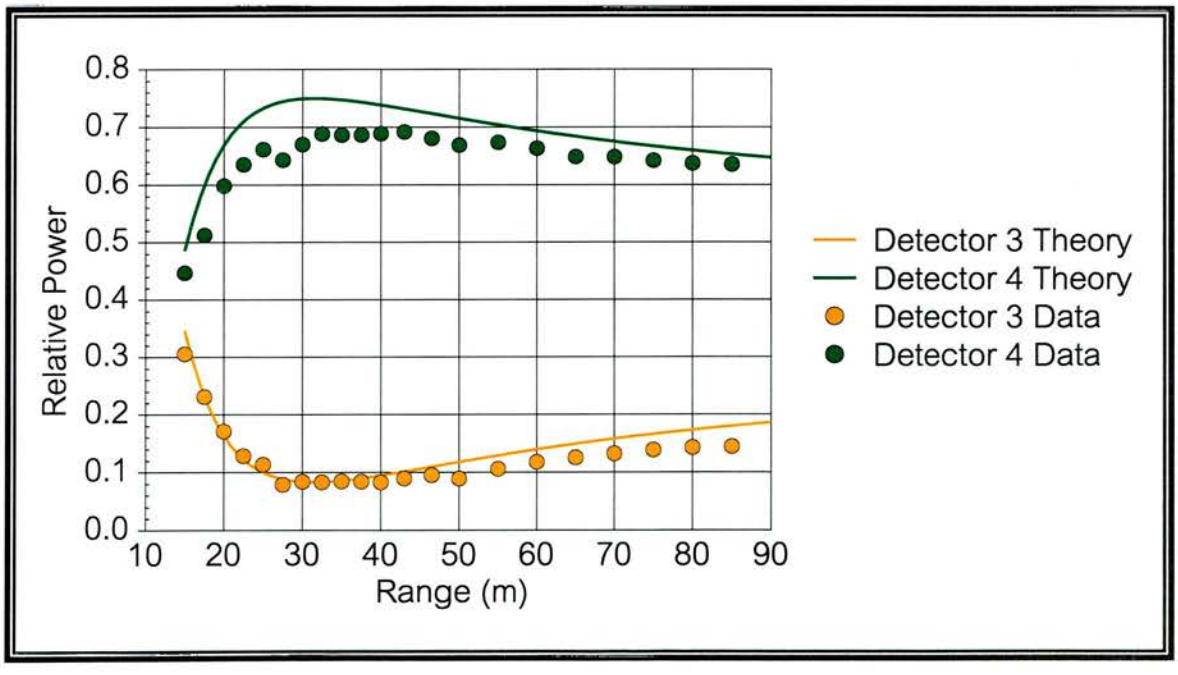

Figure 7.13 Graphs showing fitted data for detectors three and four along boresight incorporating a phase offset of -1 rad.

Again, agreement is seen between theory and data, just as we saw with the fit for detectors 1 and 2.

7.5 Fitting all the data with the theory

AFTER IT became apparent that writing a computer program to perform a fitting routine would prove too complicated, it was decided that the best method would be to use the powerful 'Solver' utility that comes with the Microsoft Excel™ spreadsheet. This would enable me to fit to all the four power equations simultaneously, while varying the bearing offsets for each range along with the phase offset in order to get the best agreement between theory and results.

I organised the spreadsheet as follows. For each range (down) and detector (across) there would be a set of columns for bearing, actual data, fitted data and the squares of the errors between them. The fitting equations would incorporate the relevant offsets, contained in cells at the top (phase offset) and the side (bearing offsets) of the spreadsheet. The sums of the squared errors for each range and detector were put in cells by each of those sets, and then summed together in one cell at the top. The Solver function was then told to minimise this sum value by altering the values of the various offsets, in other words performing a least squares fit on the data. By putting in suitable first guesses, the program was able to minimise the sum value quite rapidly.

The bearing offsets for most ranges were between -1 and -3 minutes of arc, and the phase offset was found to be -1.15 radians.

7.5.1 Quality of fit

THE QUALITY of the fit of the data to the equations is assessed by calculating the value of the statistical parameter R^2. It is defined as

$$R^2 = 1 - \frac{\sum_{i=1}^{n} (y_i - \hat{y}_i)^2}{\sum_{i=1}^{n} (y_i - \bar{y})^2}, \tag{7.26}$$

where y_i, $\hat{y}_i$, and $\bar{y}$ represent the actual data, the calculated data and the mean of the actual data respectively. In this case, the numerator will be the total sum of the squared errors calculated in the fitting process. The denominator was calculated by first working out the mean at each range and detector, and summing the squares of the deviations from that mean. The values of the sums at each range and detector were then summed as when working out the total sum squared error. The calculated value of R^2 for this data was 0.967. For a good fit, the value of R^2 should be above 0.95, which it is in this case.

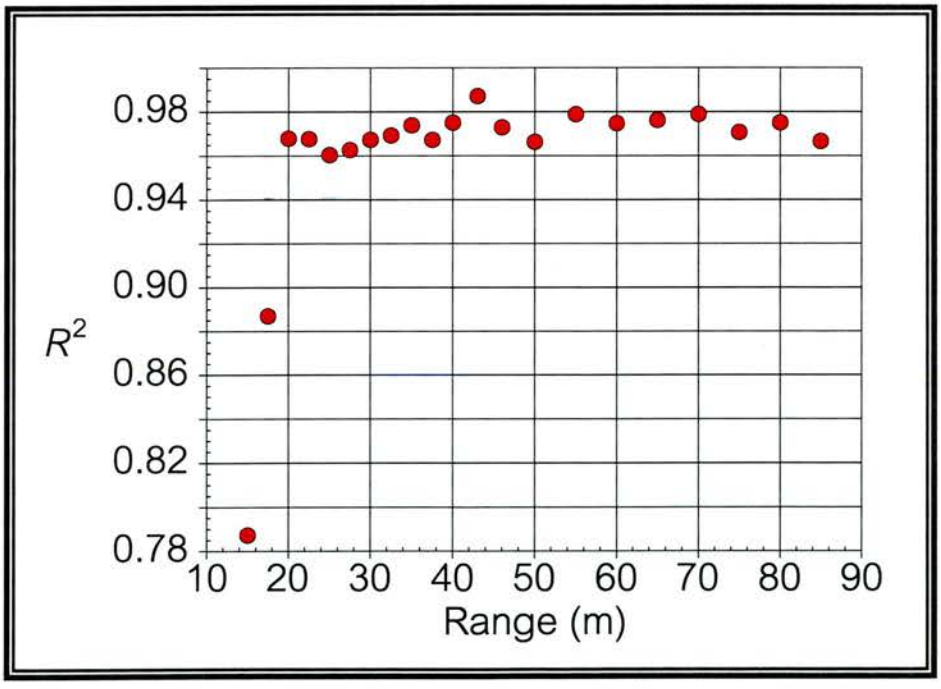

Figure 7.14 Graph of R^2 against range

In addition to working out R^2 for the entire data set, we can calculate it separately for each range. This is done in the same way as above, but summing the two quantities over the four detectors only. If we then plot R^2 against range we get the graph shown in figure 7.14.

What this shows is that while R^2 is fairly constant over most ranges, it is much lower for $r = 15\text{m}$ and 17.5m. In other words, the fit of the equations to the data is more or less equally good over the whole set of ranges except for these two shortest. This should come as no real surprise though. At the end of the previous chapter I sounded a note of caution about taking the results at distances close to the receiver too seriously. This was because of the assumption of equal received power at all three antennas of the interferometer, which was shown to be less valid when dealing with short ranges. The graph above therefore backs up the conclusion at the end of the last chapter.

7.5.2 Effect on range error

KNOWING THE quality of the fit of the power data with the theory is important, but what interests us in terms of the application of the system is the error in calculated range that would be produced by measurements such as these. The range is calculated from equations (3.44) and (3.45) followed by equation (3.14). However, it is not quite as simple as merely putting in the numbers and getting out a result. In order to be truly accurate, equations (3.44) and (3.45) need to be modified to

$$\Theta_1 = \frac{m\pi}{2} \pm \cos^{-1}\left(\frac{3\sqrt{(P_1 - P_2)^2 + (P_3 - P_4)^2}}{2(P_1 + P_2 + P_3 + P_4)}\right) - \tan^{-1}\left(\frac{P_1 - P_2}{P_3 - P_4}\right) - \Delta\Theta; \quad (7.28)$$

$$\Theta_2 = \frac{m\pi}{2} \pm \cos^{-1}\left(\frac{3\sqrt{(P_1 - P_2)^2 + (P_3 - P_4)^2}}{2(P_1 + P_2 + P_3 + P_4)}\right) + \tan^{-1}\left(\frac{P_1 - P_2}{P_3 - P_4}\right) - \Delta\Theta. \quad (7.29)$$

I have added the phase offset term $\Delta\Theta$ to the equations, as well as the extra term $m\pi/2$, where m is a positive or negative integer. This is because of the fact that when calculating the inverse cosine of a number in a computer program or spreadsheet, the answer is only given between 0 and π, and when calculating inverse tan, it is only given between $-\pi/2$ and $\pi/2$.

The easiest way of finding out the value of m and the sign in front of the inverse cosine was by using the theoretical values calculated during the fitting process. Theoretical phase values had been calculated from the range bearing and phase offset. These had then been used to calculate the power values which were fitted against the data from the interferometer. It should therefore be possible to retrieve the exact theoretical phase values for each range and bearing using the calculated powers in the above equations. By this method, using trial and error I was able to determine that equations (7.28) and (7.29) needed to be rewritten as

$$\Theta_1 = \frac{\pi}{2} - \arccos f_1(P) - \arctan f_2(P) - \Delta\Theta; \tag{7.30}$$

$$\Theta_2 = -\frac{\pi}{2} - \arccos f_1(P) + \arctan f_2(P) - \Delta\Theta; \tag{7.31}$$

for ranges of 35m or greater and

$$\Theta_1 = \frac{\pi}{2} + \arccos f_1(P) - \arctan f_2(P) - \Delta\Theta; \tag{7.32}$$

$$\Theta_2 = -\frac{\pi}{2} + \arccos f_1(P) + \arctan f_2(P) - \Delta\Theta; \tag{7.33}$$

for ranges less than 35m, where the terms in brackets in equations (7.28-9) have been replaced by $f_1(P)$ and $f_2(P)$ to aid clarity. The point in range at which the transition between the two sets of equations takes place corresponds to the point at which the centre-side path length difference, including the

offset, becomes greater than one wavelength. Using these equations on the real data, we can calculate the apparent range of the transmitter as seen by the receiver.

The calculated range was found to differ from the actual range, with a fairly clear trend with bearing. In order to look at this more closely, I have plotted in figures 7.15 and 7.16 on this page and the next graphs of the error in range against the range and the bearing. Both graphs are of the same data but the surface plot is viewed from different angles in order to show the two main areas of the graph more clearly.

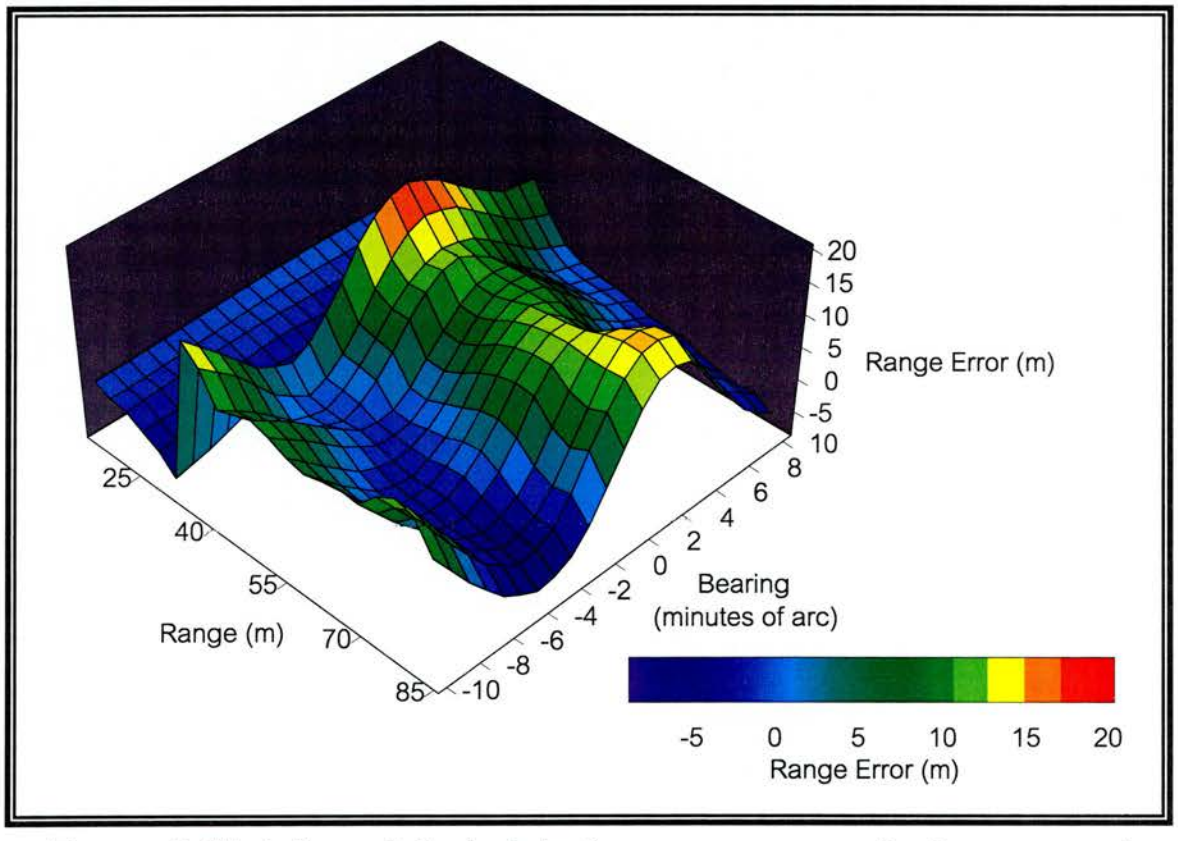

Figure 7.15 Interpolated plot of range error against range and bearing. Boresight is more or less down the bearing line of -2 minutes of arc, which corresponds to a very low range error except for ranges around 40m

In figure 7.15 we are viewing the surface from the side of higher range. We see that there is a systematic error in the range with bearing, but that range error is quite low on boresight, which as I have explained previously, corresponds to a bearing of about -2 minutes of arc. Even along this line though, the range error increases towards lower ranges, up to the discontinuity. This is possibly due to the fact that, as I mentioned towards the end of section 7.4.2, the changes in the levels of the powers at detectors 3 and 4 are much less as they reach a maximum and minimum, and as such errors are likely to be magnified.

In figure 7.16, I have shown the plot from side of lower range. After the drop following the discontinuity, the range error is minimal and much more constant with bearing than it is at higher ranges.

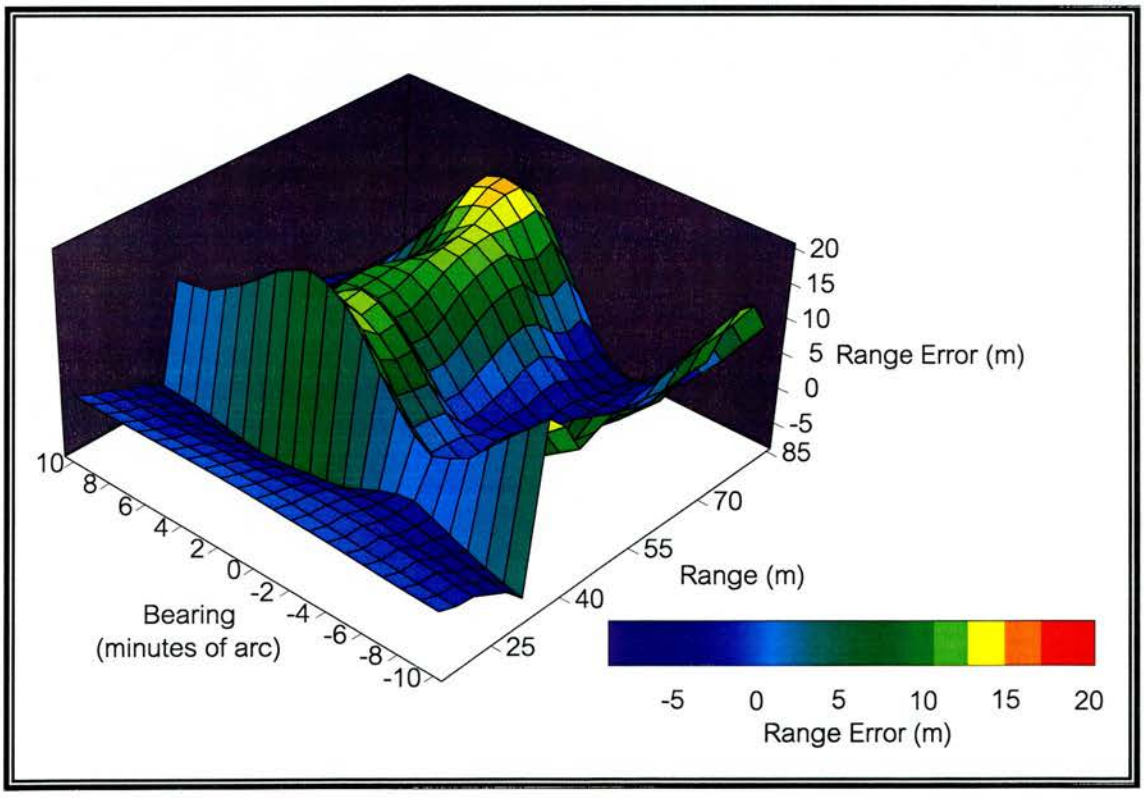

Figure 7.16 The same plot as in figure 7.15, but viewed from the reverse angle

7.6 Experiment with two transmitters

As WELL as characterising the system using one transmitter, I experimented with the possibility of resolving a second transmitter simultaneously at a different location. This was done as described below.

7.6.1 Experimental setup

THE SECOND transmitter was set up in the same way as the first one described in Chapter 5. It consisted of a similar Gunn oscillator, attenuator, pin switch and feedhorn. The main difference between the two transmitters was in the pin switch driver circuit. For the first transmitter, I used a modulation frequency of 7.8125kHz, derived by dividing down by 2048 the output from a 16MHz crystal oscillator chip. In the circuit for the new transmitter I used a different chip with a fundamental frequency of 19.6608MHz, giving a modulation frequency of 9.600kHz when divided down by the same factor. The new transmitter was put in a similar enclosure and placed on a similar stand to the first when taken out into the field.

Resolving the two transmitters is done entirely in software. The signals from both are essentially added together at the power detectors, and are amplified, filtered and sent to the computer in the same way that a single signal would be. It is in the processing that they are separated. The software is basically the same as described in Chapter 5 and Appendix 2, but with a second PSD routine. At the beginning of the program, sine and cosine arrays are set up for **both** the modulation frequencies. The PSD routine to recover a voltage value is then performed twice, once for each frequency. The four power values for each transmitter are then calculated in the same way as before, with the results being saved to two files, one for each transmitter.

The experiment itself was carried out as follows. I took both transmitters out to a range of about 55m, and placed them on their respective stands. I chose

55m as being an intermediate range, far enough away from the receiver to avoid all possibility of the errors described in Chapter 6. In fact, one transmitter was at 55m and the other at 56m sightly offset in bearing, since they would not both have fitted in the unambiguous central region of the interferogram if they had been side by side. I took one set of measurements with them both in those positions, before moving the transmitter at 56m further back to 65m while leaving the other in position. Additional measurements were taken with the second transmitter at ranges of 75m, 85m and 95m, all the while leaving the first at 55m. No measurements were taken at different bearings, since this was only intended as a proof of principle experiment for range measurements.

We would not expect this to give any more than an indication of the possibility of using two transmitters simultaneously, because of the necessity of having both sources positioned a few minutes of arc from the boresight of the receiver. As can be seen from the figure 7.15 and 7.16, this will result in a much larger range error than if we were able to position the sources dead along boresight.

7.6.2 Results

In fact, the results from these experiments were more or less masked by the error in range resulting from the source not being on boresight. Added to this is the inconsistency in the bearing of the second transmitter, arising from the fact that it had to be physically moved between each run.

The results from this experiment can be seen in figure 7.17. The calculated ranges are some way away from the actual range values, but this is probably more due to the off-boresight range error than the fact that we are trying to look at two transmitters.

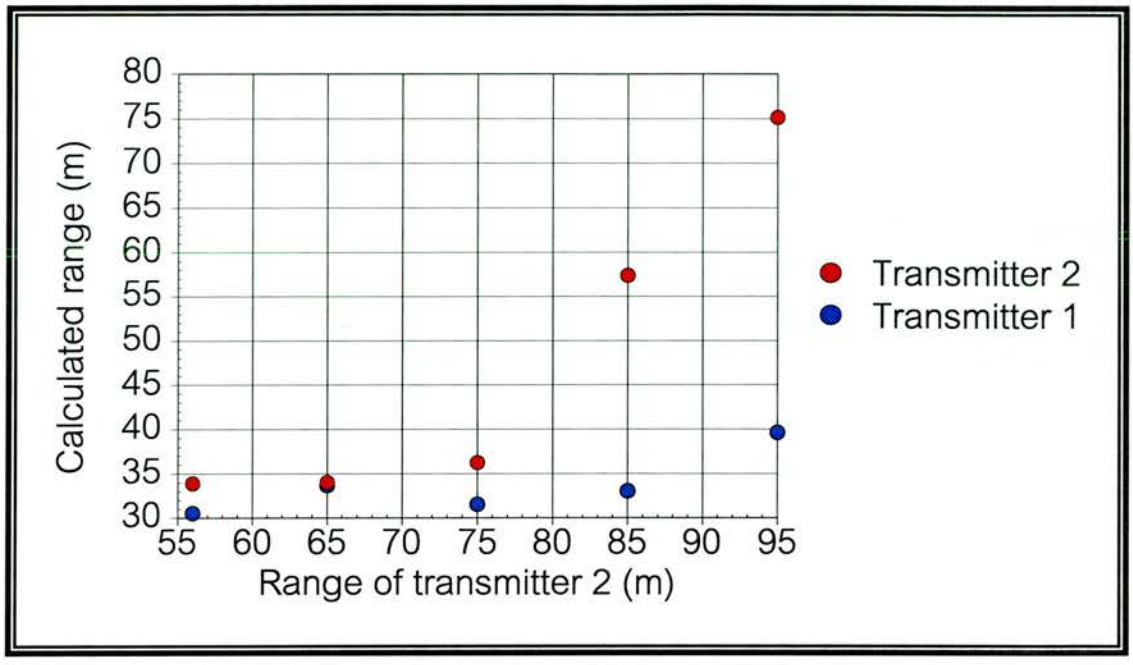

Figure 7.17 Results from experiment with two transmitters

7.7 Summary

THE RESULTS presented in this chapter have shown that there is a good agreement between theory and experiment, but that there are clearly some persistent effects that remain as yet unexplained. The values of the received powers have very good overall agreement with the theory, although it seems that the lower power values are consistently higher than expected, while the higher values are consistently lower. This would appear to be at the root of the problem of the range error off boresight. To investigate this effect fully would require some time, and so for now it is sufficient to say that we have a passive ranging system that works very well for a source in the line of sight.

Chapter 8
Atmospheric measurements

In this chapter I will present a case for using the system for studying the affect that atmospheric turbulence has on the propagating wave. This will be useful both from the perspective of determining the potential limits of this system, and in the more general case of studying this area.

8.1 Atmospheric factors affecting propagation

The effect that the atmosphere has on propagating millimetre waves is of great interest. For any application, a deeper knowledge of how a given set of atmospheric conditions can affect a signal is potentially very useful in designing a system to perform a particular task. For the ranging interferometer presented in this thesis for example, the performance will be limited by any atmospheric fluctuations altering the curvature of the incoming wavefront. I will consider this in particular in more detail shortly, but first I will give a brief outline of some of the vast amount of work that has already been carried out in the rest of the field of atmospheric studies at millimetre wave, and in particular at W-band.

8.1.1 Clear air phenomena

Clear air phenomena is the name normally given to the effects of molecular absorption, emission, and refraction, as well as the effects of atmospheric turbulence, as distinct from the effects of inclement weather. The effects of

refraction and turbulence will be considered in the next section when looking at the possible application of the interferometer system.

The major contributors to molecular absorption at millimetre wavelengths are water vapour and oxygen. As I mentioned in Chapter 1, there are a few peaks in absorption due to both types of molecules in the millimetre wave band. The water molecule absorption resonances in this part of the spectrum are due to rotational state transitions, and occur at frequencies around 22, 183, and 323 GHz [BOHL85]. The main oxygen absorption resonances, at around 60 and 118 GHz, are due to transitions between triplet components of the oxygen rotational ground energy state.

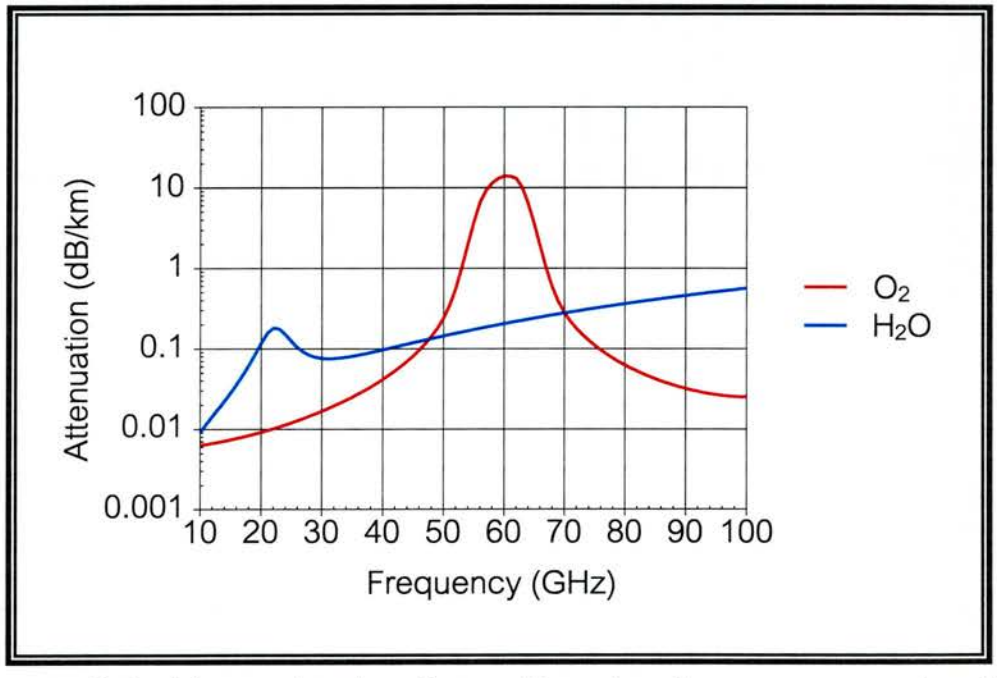

Figure 8.1 Atmospheric attenuation due to oxygen and water vapour at temperature 300K, pressure 1013mb and water vapour content 7.5g/m^3 [ULAB81]

Various models exist of the attenuation due to both types of molecule, for example [VANV47a], and [VANV47b]. For frequencies between 10GHz and

100GHz, we can use equations from [ULAB81] to plot the attenuation with frequency for each molecule, shown in figure 8.1. The total attenuation is the sum of the attenuations due to the two types of molecule. Figure 8.2 shows the variation of the total attenuation with frequency over the same range for different relative humidities.

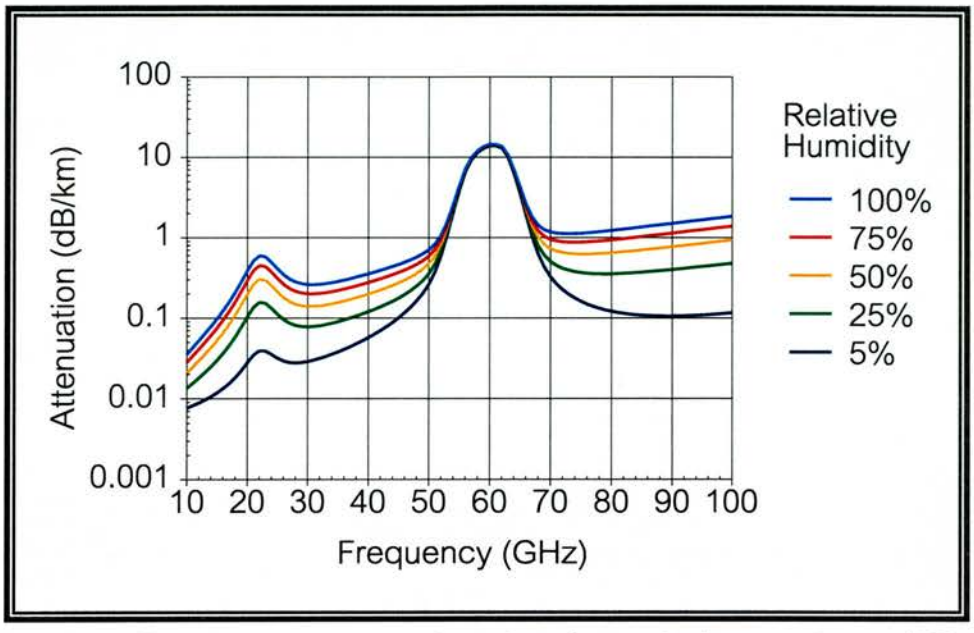

Figure 8.2 One-way attenuation in clear air for various different values of relative humidity

Emission in the millimetre wavelength region is often expressed as brightness temperature, or antenna temperature T_B, related to the power P received from the atmosphere by a radiometer [KRAU66], page 98. It produces only a small effect at the frequencies of interest, however, well below the levels of the signals normally being considered.

8.1.2 Hydrometeors and precipitation - Fog

THE TERM hydrometeor refers to any water-based particle present in the atmosphere. Larger particles are heavy enough that they fall under the force of gravity, while the lighter particles remain suspended. Suspended hydrometeors

include fog, haze and clouds, while falling hydrometeors (precipitation) include rain, snow, sleet and hail. Millimetre waves are much better than infrared or visible waves at penetrating fog, although not as good as microwaves. However, they suffer about the same amount of attenuation through rainfall.

Fog and haze are the names usually used to describe liquid water suspended in the atmosphere near the ground, the difference between them being a qualitative assessment of one's ability to distinguish objects at a difference: fog being the set of suspended water particles that limits visibility to less than 1km [TREB87].

There are two types of fog generally characterised: advection fog and radiation fog. An advection fog forms when warm, moist air moves across a cooler surface. A radiation fog forms when the ground cools after sunset, cooling the adjacent air mass until the air becomes supersaturated with water. The average drop size of an advection fog is usually larger than that of a radiation fog.

Using regression analysis to fit to real data, the following expression for attenuation in terms of temperature and wavelength has been produced [ALTS84]

$$A = -1.347 + 0.372\lambda + \frac{18.0}{\lambda} - 0.022T, \qquad (8.1)$$

where A is expressed in db/km/g/m^3, λ is the wavelength in mm and T is the temperature in °C. The expression is valid for wavelengths from 3mm to 3cm (frequencies from 100GHz to 10GHz) and temperatures from -8°C to 25°C.

The total fog attenuation per kilometre is obtained by multiplying the normalised attenuation calculated using the above equation with the fog

density in g/m^3. The fog density can be estimated from the visibility, which is defined as the greatest distance at which is it just possible for an observer to see a dark object against the horizon with the naked eye, and which is much easier to measure than density. [ELDR66] derived an empirical relationship giving visibility as a function of fog density

$$V = 0.024M^{-0.65}, \tag{8.2}$$

where V is the visibility in km and M is the density in g/m^3. Care must be taken when using this formula, however, as the correlation coefficient is dependent on the type of fog. The formula should be satisfactory for a radiation fog, which has drop diameters of typically less than 10μm, but the predicted visibility may be too low for an advection fog, in which the drop diameters can be as large as 100μm.

8.1.3 Hydrometeors and precipitation - Rain

RAINFALL, RATHER than fog, is the main contributor to attenuation at millimetre wavelengths. There has been extensive theoretical and experimental study of the relationship between rainfall rate and specific attenuation, which will only be touched upon briefly here.

The rainfall rate is usually expressed in millimetres per hour, with values ranging from 0.25mm/h for drizzle, through 20mm/h for heavy rain, to 100mm/h for a tropical downpour. Different rain rates contain different drop size distributions, the two main models of which being Laws and Parsons, and Marshall and Palmer. Attenuation can be calculated using these models if the rain rate is known. Empirically, the attenuation is commonly related to the rain rate by the expression

$$A = \alpha R^b, \tag{8.3}$$

where R is the rain rate, and α and b are constants, the values of which vary with frequency [ULAB81].

8.2 Refraction and atmospheric turbulence

THIS IS the area of atmospheric propagation effects most relevant to the use of the passive ranging interferometer described in this thesis, and it is for this reason that it is being considered separately. The attenuation effects described previously will affect the equipments ability to detect a given signal, but it is refractive index inhomogeneities in the air that will affect the final resolution of the system.

The most general form of the refractive index n is given in complex form as

$$n = n' - jn'', \tag{8.4}$$

where n' and n'' are the real and imaginary components of the refractive index. The imaginary component is associated with absorption, and makes an important contribution in fog and precipitation. In this discussion, however, we will only consider the real refractive index, responsible for the anomalous clear air effects of interest here. The refractive index of the troposphere at millimetric frequencies differs very little from the refractive index in a vacuum (which is unity), so it is often replaced with the term N, called the refractivity and defined by

$$N = (n - 1) \times 10^6. \tag{8.5}$$

An approximate relationship between the refractivity and the atmospheric pressure P, absolute temperature T and the partial pressure of water vapour e exists, proposed by [BEAN68]

$$N = \frac{77.6}{T}\left(P + \frac{4810e}{T}\right), \tag{8.6}$$

where P and e are in millibars, and T is in kelvin. The refractivity of the atmosphere varies with altitude, largely because of the fall in pressure. Temperature change also plays a role in its changing value, but its effects are much smaller than pressure change [SAUV92].

High humidity gradients, or temperature inversions, can give rise to a rapid decrease in refractive index with altitude which causes an atmospheric duct. A signal beam will become trapped in the duct and be bent, in a similar way to an electromagnetic wave in a waveguide structure.

8.2.1 Turbulence

VARIOUS STUDIES have shown that atmospheric turbulence is a significant problem when considering the propagation of millimetre waves (eg. [BOHL88], [HILL88], [KONK92]), and many theoretical studies and models exist (eg. [STRO68], [VANH90], [VANH91]). The main effects of these fluctuations in refractive index are scintillations in intensity, causing variations in received signal level, and phase changes, which give rise to fluctuations in angle of arrival of the received signal wavefront. As I have said above, it is the latter fluctuations which are of concern in this case. There have been some measurements of phase fluctuations, for example [OLMI92] and [WRIG96] at 86GHz, [KASU86] at 22GHz, and [McMIL97] at a set of frequencies from 116GHz. The latter team have investigated the way phase fluctuations affect angle of arrival measurements by using an array of four receiver apertures over a path length of 1370m.

In the case of the ranging interferometer, the expected effects of atmospheric refractive index changes can be looked at in the following way. We can imagine

a region of higher or lower refractivity moving across the field of view as in figure 8.3. As such a region crosses the field of view we will observe first a prism effect, followed by a lensing effect and another prism effect. We would therefore expect the interferometer to register correlated changes in both apparent bearing and apparent range. A region of higher refractive index will produce the effect of a focussing lens, causing the apparent range to increase as the transmitted signal diverges less rapidly. A region of lower refractive index on the other hand will increase the divergence of the signal and so make the source appear closer to the receiver than it really is.

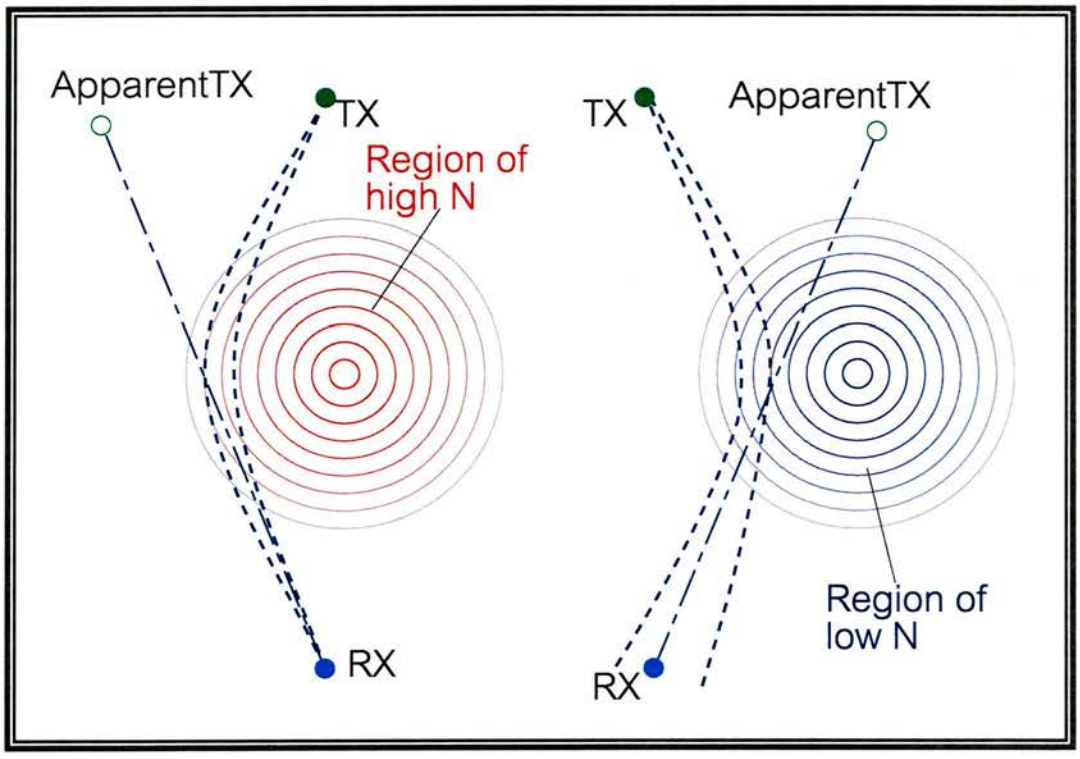

Figure 8.3 Schematic showing how regions of high or low refractive index can produce variations in apparent source bearing and range

Comparing values of range, bearing and received power, we should be able to obtain information about the sort of atmospheric variations that will affect the system, and about atmospheric turbulence in general. The aim would be to

separate the effects of the atmosphere from the effects of any vibrations or other movements of the system itself. We could then get an idea of the ultimate resolution of a perfect system, preferably in different weather conditions.

8.2.2 Potential measurement resolution

By calculating the size of the minimum detectable signal level of the interferometer, we can get an idea of the kind of refractive index change that would be observable with the system. We can begin by considering a simplified two port quasi-optical interferometer, where the power levels at two receivers will be

$$P_1 = P_R(1 + \sin\Theta); \tag{8.7}$$

$$P_2 = P_R(1 - \sin\Theta), \tag{8.8}$$

where Θ has its usual meaning, being the phase difference between the two input ports. In the system we have used a heterodyne radiometer, and can therefore define a minimum detectable temperature change [KRAU66]

$$\Delta T_{\min} \approx \frac{T_N}{\sqrt{B\tau}}, \tag{8.9}$$

where T_N is the receiver noise temperature, B is the bandwidth and τ is the integration time. This can be related to a minimum detectable power change

$$\begin{aligned} \Delta P_{\min} &= k\Delta T_{\min} B; \\ &\approx k T_N \sqrt{\frac{B}{\tau}}. \end{aligned} \tag{8.10}$$

We can use this value as a typical uncertainty level when using the powers to calculate a given quantity. In this case, we can deduce the minimum detectable change in the phase difference.

Using the small angle approximation for $\sin\Theta$, we can express the phase difference as

$$\Theta = \frac{P_1 - P_2}{P_1 + P_2}. \tag{8.11}$$

If each of the observed powers is allowed to be in error by a typical amount ΔP, then we can write

$$\Theta_0 = \frac{P_1 \pm \Delta P - P_2 \pm \Delta P}{P_1 \pm \Delta P + P_2 \pm \Delta P}, \tag{8.12}$$

which, if the variations are uncorrelated between the receivers can be approximated to

$$\Theta_0 \approx \Theta \pm \frac{\Delta P}{\sqrt{2}P_R}. \tag{8.13}$$

Combining equations (8.10) and (8.13), we can say that the uncertainty in the phase measurements will be

$$\delta\Theta \approx \frac{\Delta P}{\sqrt{2}P_R} = \frac{kT_N}{P_R}\sqrt{\frac{B}{2\tau}}. \tag{8.14}$$

Using the Link Gain equation we can relate this to the transmitted signal power P_T, obtaining

$$\delta\Theta \approx \frac{kT_N}{P_T G_T G_R}\left(\frac{4\pi Z}{\lambda}\right)^2\sqrt{\frac{B}{2\tau}}. \tag{8.15}$$

In a Gaussian mode system, we can rewrite the antenna gains G_T and G_R in terms of the underillumination ratios U_T and U_R and diameters D_T and D_R of

the transmitter and receiver antennas using

$$G = \left(\frac{2\pi D}{\lambda U}\right)^2. \tag{8.16}$$

Assuming that the antennas are aligned and are at a large enough range that both the antenna patterns overlap sufficiently, we obtain

$$\delta\Theta \approx \frac{kT_N}{P_T}\left(\frac{\lambda Z U_T U_R}{\pi D_T D_R}\right)^2 \sqrt{\frac{B}{2\tau}}. \tag{8.17}$$

The above expression can be used to estimate the phase sensitivity of the interferometer. Although the calculations are for a two port interferometer, the result should be equally applicable to the three port system being used. Recall that in the system as described in Chapter 5, we had a receiver port diameter D_R of 53mm, a transmitter port diameter D_T (the feedhorn diameter) of 30mm, and a transmitter power P_T of around 1mW, at a wavelength of 3mm. Also in Chapter 5, the underillumination ratios in both cases were stated as $U = 3$ for both transmitter and receiver. The radiometers used have a bandwidth of about 1GHz. In the next chapter, we will consider a revised receiver setup which will use a low pass filter having a cut-off of about 100Hz, giving an integration time of 10ms. A typical noise temperature for this type of receiver is 600K. This gives us the calculated relationship between phase sensitivity and range shown in figure 8.4.

It can be seen from the plot that the phase uncertainty at a range of 100m is the order of 1 microradian, rising to about a milliradian at 5km. These values are very much less than the magnitude of the phase fluctuations recorded in [HILL88], for example. Extrapolated for the port spacing of this system, the standard deviation of their results would be from 1000 to 10000 greater than this level. Although the sensitivity of the system may differ from these

theoretical values, if we take a phase sensitivity of 1 milliradian, then at a wavelength of 3mm, this would correspond to a path length difference of less than 0.5μm.

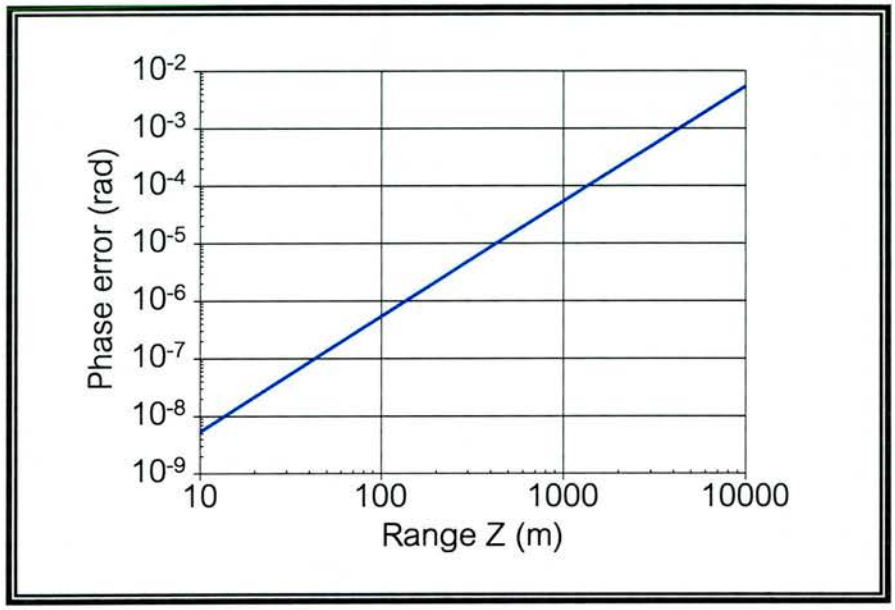

Figure 8.4 Calculated phase error with range for a system similar to that described in Chapter 5

The most common cause of turbulence at microwave and millimetre wave frequencies is fluctuations in humidity [BRUS95]. At W-band, the refractive index of liquid water is about 3.6. The phase change imposed by a layer of water of thickness δz will be given by

$$\Delta\phi = \frac{2\pi\delta z\,(n-1)}{\lambda}. \tag{8.18}$$

At a frequency of 94GHz, with an assumed detectable phase change of 100 milliradians, we would theoretically be able to observe a differential integrated thickness of liquid water between two paths of around 0.2μm.

Chapter 9
An Atmospheric Measurement System

In this chapter I will look at the issues of system redesign if the interferometer is to be used in the context of an atmospheric measurement program.

9.1 Modification of computer program

In order to be able to continuously monitor the signal from the transmitter it would be necessary to redesign the rear of the system to accommodate this sort of measurement. The original setup had the capture computer program taking the data from the output of the pre-amp, which was demodulated using the PSD routine in software. This method involved taking chunks of data and turning it into one value, rather than obtaining a continuous stream.

9.1.1 Continuous data acquisition

The previous program, as I have just mentioned, was designed to take a chunk of data, and then stop the acquisition whilst the data was processed. It used a function call to the card which streamed a given number of data points into main memory for the main program to deal with. Instead of this, I decided to use a different call which would stream data continuously into an area of main memory. Another call could tell the main program which half of this buffer was being filled at any given time, enabling it to save the other half to disc without interfering in the capture process.

The original plan was to save a stream of data captured directly from the output of the preamp, leaving the PSD processing still to be done in software. On the face of it, this was still possible, although challenging. It would require the programming of a digital filter, such as outlined in [LOCK89], but I began by modifying an existing program* for one that would work in this case. The modified program (see Appendix 2, section A2.2) works by performing a PSD-type operation on each data point to obtain the real and imaginary parts. A first order filter is then applied to each of these, before the result is saved to file. The first order filter consists simply of the application of the two filter constants

$$a = \frac{1}{e^{2\pi B\tau}}; \tag{9.1}$$

$$b = 1 - a, \tag{9.2}$$

where B is the desired bandwidth in Hz and τ is the sample length in seconds. The filtered value in each case is

$$x_i = ax_{i-1} + bx, \tag{9.3}$$

where x is the newly calculated real or imaginary value. I chose B to be 100Hz, on the assumption that any interesting effects will not be at higher frequencies. With the card sample length of about 50μs (a sampling frequency of 20kHz - see below), a comes out at about 0.97 (with b therefore 0.03), so we can see that the value x_i will depend mostly on its previous value x_{i-1}, with the new data point x contributing only slightly to it. Given that the filter bandwidth is 100Hz, the sampling theorem tells us that we only need sample at double this frequency in order to retain all the information in the waveform. This means that we only need to save every 100th point.

* Lesurf, J.C.G., Private communication

The sample rate used in the original program was about 41kHz. However, while trying to stream data continuously at this rate, it became apparent that there were some problems with the card. In trying to both acquire the data and save to disk, it would frequently outrun itself, with the result that there would be a loss of data. Dropping the sampling rate to half its original value seemed to cure this problem. It would still be a high enough rate for the sampling condition to be met, and had the added advantage that half the disk space would be required. In order to further save disk space, and to make the saving process more reliable, I opted to save the data in binary format.

9.1.2 Impracticalities of initial approach

AFTER HAVING tried this method for a period of time, it became apparent that there were two significant disadvantages with the whole approach. Firstly, the sheer volume of data made the process impractical. For example, an hours worth of binary data saved to disk would produce

$$\begin{aligned}\text{Number of bytes} &= \text{No of channels} \times \text{No of bytes in an integer} \times \text{Sample rate} \times \text{Time} \\ &\approx 4 \times 4 \times 20000\ \text{Hz} \times 3600\ \text{s} \\ &= 1152000000\ \text{bytes} \approx 1\ \text{Gb}.\end{aligned}$$

Even in the age of hard drives of over 30Gb capacity, one gigabyte per hour still represents a relatively unmanageable amount of data. The second disadvantage is related to this high volume of data and concerns the running of the filter program. On an hours worth of data, the filter program would require several hours to process it. In fact, it was necessary to leave the program running over night.

Clearly, these problems were going to make it difficult to gather and analyse the amounts of data that would be necessary. The obvious solution was to try and lower the data rate at which the card needed to sample, and therefore the

amount of data being saved to disk. As I was only interested in a final data rate of a couple of hundred Hertz at most, it seems rather wasteful to capture data at a hundred times this rate.

9.2 Addition of processing hardware

IN ORDER to avoid capturing at a high data rate it would be necessary to perform the PSD processing in hardware. This would necessitate the construction of a processing circuit which could do the following things:

- produce two signals of the same frequency as the transmitter modulation frequency, but offset 90° from each other;
- multiply each of these signals by the received waveform at each channel to produce an I and Q component;
- filter the components using an appropriate low pass filter;
- perhaps perform the root-sum-square of the I and Q.

The last point is not so important, as it doesn't affect the final sampling rate. The only disadvantage would be that it would require eight channels of data to be saved instead of four. I have therefore not included it in the circuit I built, since the card is capable of handling eight inputs, and because the construction of such a component to perform that task is non-trivial. If work were to be carried out with two transmitters however, it may be necessary to introduce a device to do this into the circuit, the alternative being to buy a second acquisition card.

All the circuits that follow were built on custom made printed circuit boards that I designed using 'EasyPCB' for DOS.

9.2.1 Circuit design

I WILL now discuss the three stages of the circuit I designed. First is the stage where the signals are produced. The simple solution to producing a signal of the same modulation frequency as the one modulating the transmitter signal is to use the same basic setup, using the same model of crystal oscillator chip. In the original circuit (shown in chapter 5, figure 5.4), I used a chip with a fundamental frequency f_0 of 16MHz. This frequency could be divided down in the chip itself to $f_0 / 128$, after which an LS93 divider was used to divide this frequency by 16 to obtain the 7.8125kHz modulation frequency.

The basic design of the original circuit would therefore remain the same, the only problem being to find a way of producing a second signal at the same frequency, but offset by a quarter cycle. This was achieved by using the setup shown in figure 9.1.

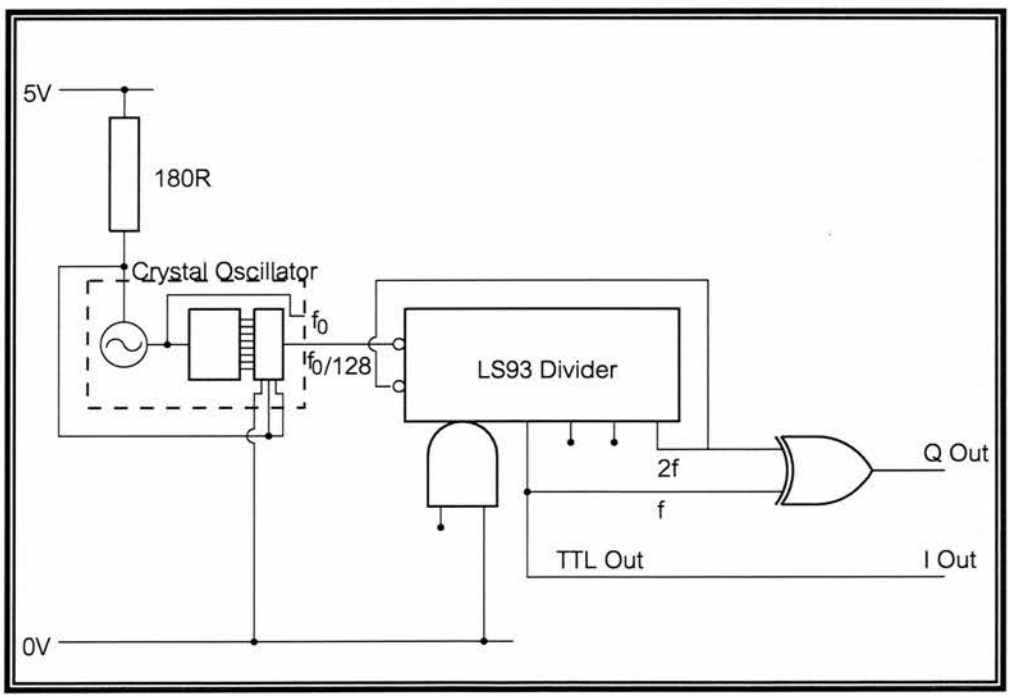

Figure 9.1 Circuit diagram for the reference signal part of the phase sensitive detection circuit

The in-quadrature signal is produced using an XOR logic gate, its inputs tapped from the in-phase output, and the last but one divided stage. That this works for producing a quarter-period-offset waveform can be seen from figure 9.2.

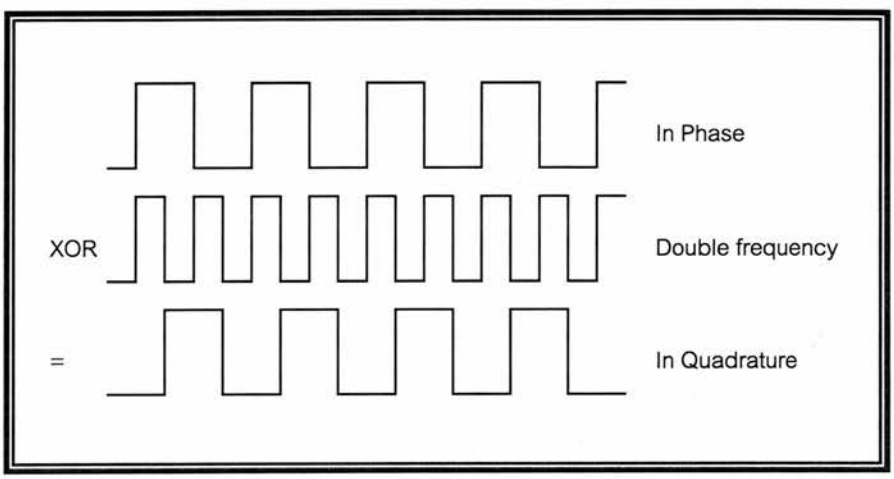

Figure 9.2 Performing an XOR operation on a signal and one at double its frequency will produce a signal offset by a quarter cycle from the original signal

Since only one circuit was going to provide the references for all four channels, it was necessary to make sure that the circuit was capable of producing enough current. For this purpose I used a pair of transistor followers. Before the followers, I also included on each output a low noise Schottky AND gate with the inputs tied to smooth out any slight glitches.

Now that the I_{ref} and Q_{ref} signals have been produced, we need a way of combining them with the signals themselves to retrieve the signal output level from the modulated waveform. The I_{ref} and Q_{ref} reference signals are in TTL form, so cannot be multiplied by the data signal directly. The easiest way of getting round this problem is to use the circuit shown in figure 9.3. The input signal is split into two channels, one of which (the lower one in the diagram) is inverted. A switch fed by the TTL I_{ref} or Q_{ref} signal is used to alternate the

output between the normal and the inverted signals. What this does is effectively the same as multiplying the input signal by a square wave of unit amplitude, having the frequency and phase of the I_{ref} or Q_{ref} signal.

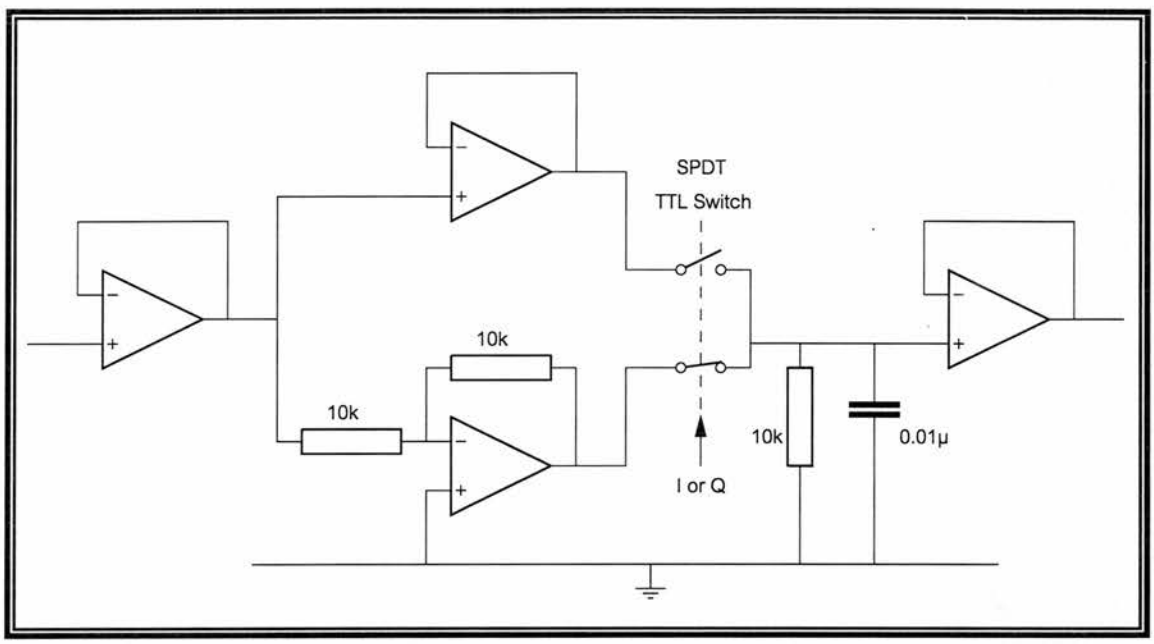

Figure 9.3 Circuit for chopping the input signal at the modulation frequency. One of these circuits is used for the I and Q for each channel

One circuit of the type in figure 9.3 is used for the I and Q for each channel. The incoming signals from the preamp are split and fed into two such circuits. The switch in one is triggered by the I reference (I_{ref}) while the switch in the other is triggered by the Q reference (Q_{ref}), giving two outputs, I_{out} and Q_{out} for each channel.

The outputs still require filtering however, in order to rectify them properly. For this we need a filter with a time constant $\tau \gg 1/f$, where f is the modulation frequency. I had already mentioned using a sampling rate of 200Hz, which would lead to a filter time constant of 10ms, far greater than $1/7.8125$ and therefore perfectly suitable.

In order for the output to be as realistic as possible, we need a filter with a reasonably sharp roll off. This is because if we are sampling at 200Hz, we can see in our output frequencies of 100Hz or less. However, if there are higher frequencies than this present at significant levels, they will still appear in the output, but will be folded down, and appear as levels in the 0-100Hz range. As a rule of thumb therefore, we can say that we need a low pass filter that will result in the level of the signal at 200Hz being 20dB down on the level at the cut off frequency of 100Hz.

I decided to use a second order active filter to perform the cut off at 100Hz. The resistor values were chosen, referring to [HORO89] Chapter 5, to provide a good speed of roll off at the cut off frequency. As an extra precaution, I added in a passive filter with a cut off of 15kHz to remove higher frequencies. One channel of such a filter is shown in figure 9.4.

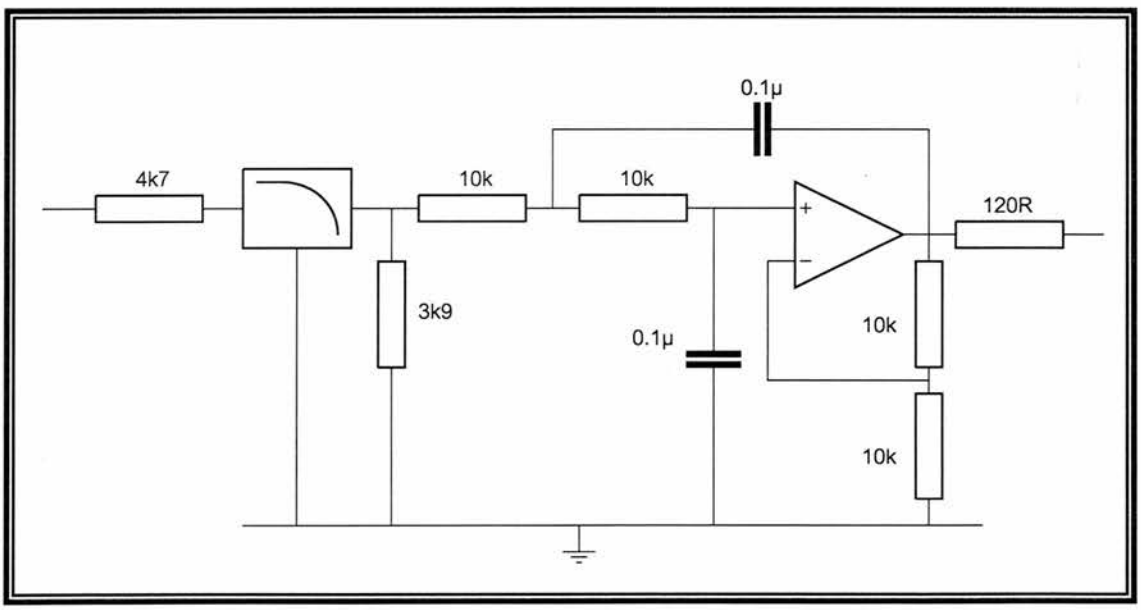

Figure 9.4 A filter circuit. The signal is passed through a passive filter first to remove the highest frequencies, and then through a second order active filter with a 100Hz cut-off frequency

The response of the filter is shown in figure 9.5. We can see quite clearly from the figure the roll off of some 12dB per octave, which is sufficient for this work.

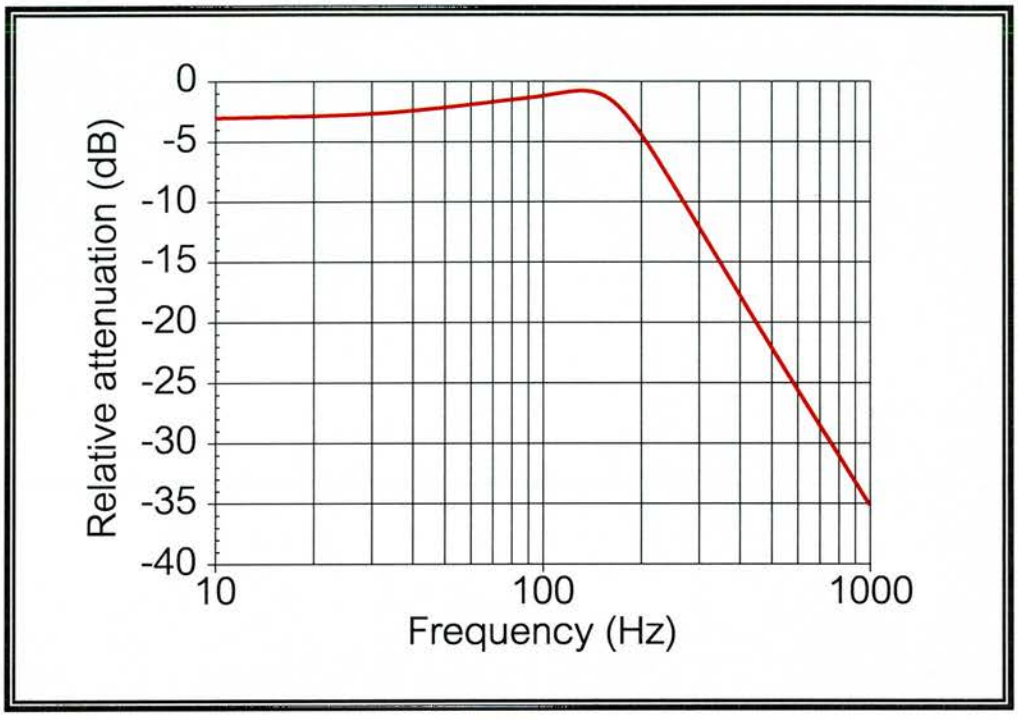

Figure 9.5 Response of the filter shown in figure 9.4

9.2.2 Testing the processing hardware

BEFORE USING the processing hardware in the system itself, I carried out some brief tests to establish that it was working correctly. I used a signal generator to produce a sine wave signal similar to one that would be received from the preamp during a real experiment. In other words, I used a signal of the modulation frequency, with an amplitude of about 1Vpp. Although the frequency of the crystal was supposed to be 7.8125kHz, I found that it was in fact just under half a Hertz away from that value, resulting in a slow oscillation of the output I and Q voltages. I tuned the signal generator until there was no more movement, and then used the oscilloscope to grab traces of the input wave, the I and Q references, the I and Q outputs, and the final filtered

voltages which would be captured by the computer. These are all shown in figure 9.6.

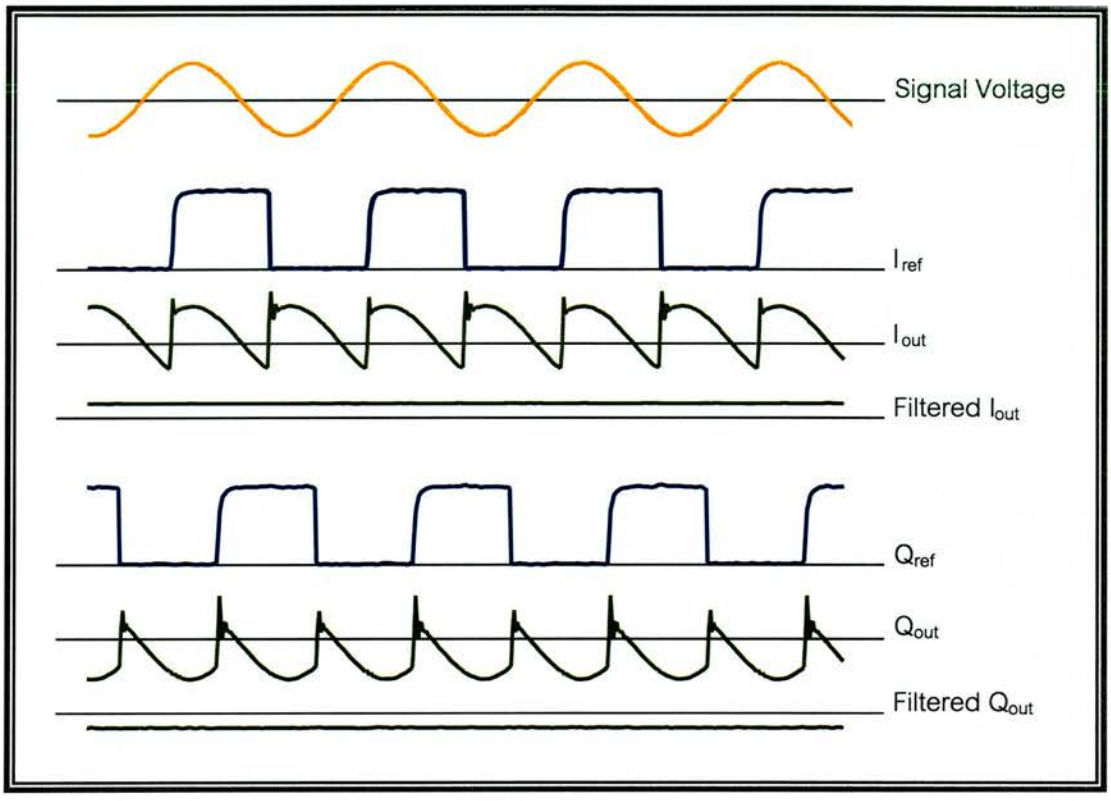

Figure 9.6 Captured traces showing the function of the PSD circuit

From the traces in the figure above, the circuit can be seen to be working as expected. The root mean square amplitude of the input signal voltage can be recovered from the two outputs by squaring, adding and square rooting their values, as predicted.

9.2.3 Modification of software

THE SOFTWARE only required basic modification from the version described in the previous section, in that only the sampling rate needed to be changed. The new sampling rate of about 200Hz per channel means that only one hundredth of the amount of data required previously needs to be saved to disc. This results in a data rate of just over 10Mb per hour, which is clearly much more

manageable if we wish to use the system for continuous atmospheric monitoring. To make the processing easier, and to make the data easier to examine, I have taken advantage of the lower data rate to save the data directly as CSV. This results in a data rate of nearer 30Mb per hour, which, although larger than would be practical for a continuous acquisition system, will be acceptable for initial testing purposes. A final system would probably use the binary format described previously. A transcript of the data capture program is found in Appendix 2, section A2.3.

9.3 Real measurements

IN ORDER to fully test the system, it was necessary to try it with a source in the field. I decided to set up the source on boresight at a distance of about 50m. I set the experiment running for about three hours, and repeated the run on three consecutive days.

9.3.1 Problems with the acquisition card

WHEN IT came to analysing the results, however, it became apparent that the problem with the card outrunning itself had not disappeared. This was noticeable from looking closely at the data file that had been saved during the experiment. The problem would appear to be that every now and then, a few words of sampled data would fail to get transferred from the card memory to main memory for saving to disk. The reason this created a problem was because the number of missing words was not usually a multiple of eight, the number of channels. The effect this had was of 'rotating' the eight channels of data such that, for example, the data from channel 1 might appear on channel 4, channel 2 on channel 5, and so on. The number of channels that the data was shifted by was completely random, though.

The origin of the problem would seem to be in the generation of interrupts. Most of the time, these are of a short enough duration that they don't affect the acquisition of data using the card, but every now and then there will be a number of interrupts in a short space of time.

When running the original data streaming program, sampling the data at about 42kHz, the sheer volume of data being saved to disk would create enough interrupts during saving to make the problem much more obvious. At that stage, the problem was occurring at least a couple of times a minute. Although lowering the sampling rate appeared to cure the problem, in fact it just reduced the regularity of the glitches, meaning that the acquisition process could be glitch free for up to half an hour.

Connecting the computer to the local network aggravated the problem, as did running the acquisition in multi-tasking mode.

9.3.2 Possible workarounds

If we are to recover any of the data, we need to find a way of putting the channels back in the right order. The way I was able to tell that the channels had been rotated in the first place, was that the larger values associated with the power received by the fourth detector were in the wrong column in the output files. This characteristic of the results could therefore be used to recover the full data set. I would need to write a program that searched each line for the largest value, and made sure that it was in the correct column, rotating the columns if it wasn't. This process is made slightly more complicated by the fact that we are now not dealing with the four original channels, but with eight channels of I and Q values. What we would therefore need to do would be to take adjacent pairs of the I and Q values, and square and add them to give eight new values. We could then look for the largest value of these eight numbers, which would be the combination of the I and Q for channel 4.

The ideal, however would be to fix the problem with the card, and then take more data, which is not broken in this way. These experiments were conducted right at the end of my Ph.D., and so further investigation into the operation of the card, and any possible fix, was not possible at the time.

9.3.3 A final note

HOWEVER, SINCE that time, I have found a way of curing the problem. The card uses a crystal oscillator to generate the frequency at which it samples. After consultation with Andy Ray of Intelligent Interfaces, who supply the card, I decided to change the oscillator for one of a lower frequency. Specifically, I changed the original 10MHz oscillator for one of 4MHz. This has cured the problem, and I have been using the card for taking data continuously for periods of several weeks with no glitches.

Chapter 10
A Final Review

In this chapter I present a conclusion to the work carried out for this thesis, and look at possibilities for future work.

10.1 Conclusion

In this thesis I have set out to provide a detailed analysis of a three port millimetre wave quasi-optical spatial interferometer for use in the area of passive ranging, and possibly also in the study of atmospheric fluctuations at W-band.

I started in Chapter 3 by developing a theory of a particular three port quasi-optical spatial interferometer. The theory requires no approximations to be made regarding the derivation of the range and bearing of a source in terms of the phases at the three ports. An approximation is necessary however regarding the received powers, in that to make the calculations feasible, we need to assume all ports receive equal powers.

In Chapter 4, I compared the theory with results that had already been taken with the original interferometer. I found that in order for the data to agree with the theory, it was necessary to introduce a phase offset term into the theory to take account of the fact that not all path lengths within the system are equal.

Chapter 5 described the redesign and testing of a new system which was built with the aim of producing a more stable setup. Of particular concern was the physical rigidity of the system: unlike the original version, the redesigned system had all the components firmly attached to one baseplate, which prevented any movement that might affect the reliability of the results.

In Chapter 6 I presented an argument to justify the use of the equal received powers approximation that I had made when developing the theory in Chapter 3. It was found that the approximation was indeed valid for all but the shortest ranges.

The main experimental results were presented in Chapter 7. Results were taken at a variety of ranges and bearings in order to obtain as comprehensive a data set as possible. Expressions for the theoretical power values were fitted to the data for bearing offsets and the phase offset. The fit was found to have an R^2 value of over 0.97 over all ranges and bearings, implying a very good agreement between theory and experiment. The equations derived in Chapter 3 were used to calculate the phase differences from the received powers. These were then used in turn to calculate theoretical range values. The values of the calculated ranges agreed very well with the actual range values if the source was positioned on boresight, but produced errors in the range at bearings away from the line of sight.

Chapters 8 and 9 presented the case for using the system to study fluctuations in atmospheric refractive index. In Chapter 8 I outlined the general area of atmospheric effects on millimetre wave signals, while in Chapter 9 I presented a redesign of the back end of the system that would enable continuous data streaming. I developed a custom hardware PSD circuit that would process the results, enabling them to be saved at a lower data rate.

Overall, the quasi-optical spatial interferometer described in this thesis has been shown to be a potentially powerful device for obtaining range information on a source by passive means.

10.2 Future work

THE MOST obvious area of future work would be a proper measurement program to investigate the effect of atmospheric fluctuations on the signal. As I mentioned at the end of Chapter 9, the problems with the data acquisition card have been resolved since the work described in this thesis was completed, and it would therefore be possible now to take continuous measurements using the system as it stands. Of course, if we were to do this, it would also be desirable to set up a permanent source to be monitored. The laborious nature of having to set the source up outside every day, and the fact that running off battery power only gives a few hours of operation per day, makes a sustained measurement campaign without a permanent source setup unlikely.

However, since the conclusion of this work, I have been working on a project for the UK Radiocommunications Agency which will use an interferometer for studying atmospheric fluctuations at Ka-band [EVAN01]. The aim is to use existing mobile phone base station transmitters as the sources. The measurement campaign will run in parallel with measurements of precipitation made using a weather radar operated by the Rutherford Laboratories.

The need to run the experiment at Ka-band precludes the use of quasi-optics as a processing technique, because of the awkwardness of constructing such a device, due to the size of the components that would be required. For this reason, we have chosen to downconvert the signal, and do the interferometry at i.f., using off the shelf components.

Appendix 1
Proofs from Chapter 3

In this appendix are contained proofs for three sections of mathematics which appeared in Chapter 3.

A1.1 Proofs from equations (3.12-13) to (3.14-15)

In equations (3.12) and (3.13), we had expressions for the two circles centred on the side ports that passed through the source position.

$$(r \sin\phi - X)^2 + (r \cos\phi)^2 = (r + \lambda\Theta_1)^2; \tag{3.12}$$

$$(r \sin\phi + X)^2 + (r \cos\phi)^2 = (r + \lambda\Theta_2)^2. \tag{3.13}$$

Expanding the brackets and using the relation $\cos^2\phi + \sin^2\phi = 1$, we obtain

$$r^2 + X^2 - 2rX \sin\phi = r^2 + 2r\lambda\Theta_1 + \lambda^2\Theta_1^2; \tag{A1.1}$$

$$r^2 + X^2 + 2rX \sin\phi = r^2 + 2r\lambda\Theta_2 + \lambda^2\Theta_2^2. \tag{A1.2}$$

We can subtract r^2 from each side of the two equations to give

$$X^2 - 2rX \sin\phi = 2r\lambda\Theta_1 + \lambda^2\Theta_1^2; \tag{A1.3}$$

$$X^2 + 2rX \sin\phi = 2r\lambda\Theta_2 + \lambda^2\Theta_2^2. \tag{A1.4}$$

To solve for r first, we add the two equations, obtaining

$$2X^2 = 2r\lambda(\Theta_1 + \Theta_2) + \lambda^2(\Theta_1^2 + \Theta_2^2), \tag{A1.5}$$

which can be seen to be solveable for r to yield

$$r = \frac{2X^2 - \lambda^2(\Theta_1^2 + \Theta_2^2)}{2\lambda(\Theta_1 + \Theta_2)}. \tag{3.14}$$

To solve for $\sin\phi$, we begin by subtracting equation (A1.3) from (A1.4) to give

$$4rX\sin\phi = 2r\lambda(\Theta_2 - \Theta_1) + \lambda^2(\Theta_2^2 - \Theta_1^2); \tag{A1.6}$$

$$\Rightarrow \sin\phi = \frac{\lambda(\Theta_2 - \Theta_1)}{2X} + \frac{\lambda^2(\Theta_2^2 - \Theta_1^2)}{4rX}. \tag{A1.7}$$

Substituting equation (3.14) for r into equation (A1.7), we obtain

$$\sin\phi = \frac{\lambda(\Theta_2 - \Theta_1)}{2X} + \frac{\lambda(\Theta_1 + \Theta_2)\lambda^2(\Theta_2^2 - \Theta_1^2)}{2X(2X^2 - \lambda^2(\Theta_1^2 + \Theta_2^2))}; \tag{A1.8}$$

$$\Rightarrow \sin\phi = \frac{\lambda(\Theta_2 - \Theta_1)(2X^2 - \lambda^2(\Theta_1^2 + \Theta_2^2)) + \lambda(\Theta_1 + \Theta_2)\lambda^2(\Theta_2^2 - \Theta_1^2)}{2X(2X^2 - \lambda^2(\Theta_1^2 + \Theta_2^2))}. \tag{A1.9}$$

By rearranging the numerator to bring the Θ_1 and Θ_2 terms out of the brackets, we see that we obtain the form of the equation expressed in (3.15):

$$\sin\phi = \frac{\lambda\Theta_2(X^2 - \lambda^2\Theta_1^2) - \lambda\Theta_1(X^2 - \lambda^2\Theta_2^2)}{X(2X^2 - \lambda^2(\Theta_1^2 + \Theta_2^2))}. \tag{3.15}$$

A1.2 Proof from equations (3.16-19) to (3.22-24)

Recall equations (3.16) to (3.19)

$$O_1 = N_T H_R C + N_T H_T S; \tag{3.16}$$
$$O_2 = N_R H_R C + N_R H_T S; \tag{3.17}$$
$$O_3 = P_R H_T C + P_R H_R S; \tag{3.18}$$
$$O_4 = P_T H_T C + P_T H_R S; \tag{3.19}$$

where

$$C = KMN_T E_C; \tag{3.20}$$
$$S = P_T M N_T E_2 + N_R M N_T E_1. \tag{3.21}$$

Substituting the modified Jones matrices for each of the elements, we obtain

$$O_1 = \frac{1}{2}\begin{pmatrix}1 & 1\\ 1 & 1\end{pmatrix}\begin{pmatrix}0 & 0\\ 0 & 1\end{pmatrix}C + \frac{1}{2}\begin{pmatrix}1 & 1\\ 1 & 1\end{pmatrix}\begin{pmatrix}1 & 0\\ 0 & 0\end{pmatrix}S; \tag{A1.11}$$
$$O_2 = \frac{1}{2}\begin{pmatrix}-1 & 1\\ -1 & 1\end{pmatrix}\begin{pmatrix}0 & 0\\ 0 & 1\end{pmatrix}C + \frac{1}{2}\begin{pmatrix}-1 & 1\\ -1 & 1\end{pmatrix}\begin{pmatrix}1 & 0\\ 0 & 0\end{pmatrix}S; \tag{A1.11}$$
$$O_3 = \frac{1}{2}\begin{pmatrix}-1 & -1\\ 1 & 1\end{pmatrix}\begin{pmatrix}1 & 0\\ 0 & 0\end{pmatrix}C + \frac{1}{2}\begin{pmatrix}-1 & -1\\ 1 & 1\end{pmatrix}\begin{pmatrix}0 & 0\\ 0 & 1\end{pmatrix}S; \tag{A1.12}$$
$$O_4 = \frac{1}{2}\begin{pmatrix}1 & -1\\ -1 & 1\end{pmatrix}\begin{pmatrix}1 & 0\\ 0 & 0\end{pmatrix}C + \frac{1}{2}\begin{pmatrix}1 & -1\\ -1 & 1\end{pmatrix}\begin{pmatrix}0 & 0\\ 0 & 1\end{pmatrix}S, \tag{A1.13}$$

where

$$C = \frac{1}{2}\begin{pmatrix}-1 & 0\\ 0 & -i\end{pmatrix}\begin{pmatrix}-1 & 0\\ 0 & 1\end{pmatrix}\begin{pmatrix}1 & 1\\ 1 & 1\end{pmatrix}E_C; \tag{A1.14}$$
$$S = \frac{1}{4}\begin{pmatrix}1 & -1\\ -1 & 1\end{pmatrix}\begin{pmatrix}-1 & 0\\ 0 & 1\end{pmatrix}\begin{pmatrix}1 & 1\\ 1 & 1\end{pmatrix}E_2 + \frac{1}{4}\begin{pmatrix}-1 & 1\\ -1 & 1\end{pmatrix}\begin{pmatrix}-1 & 0\\ 0 & 1\end{pmatrix}\begin{pmatrix}1 & 1\\ 1 & 1\end{pmatrix}E_1 \tag{A1.15}$$

Simplifying equations (A1.11) to (A1.13) and substituting simplified forms of (A1.14) and (A1.15) we obtain

$$O_1 = \frac{1}{4}\begin{pmatrix} 0 & 1 \\ 0 & 1 \end{pmatrix}\begin{pmatrix} 1 & 1 \\ -i & -i \end{pmatrix}E_C + \frac{1}{4}\begin{pmatrix} 1 & 0 \\ 1 & 0 \end{pmatrix}\left[\begin{pmatrix} -1 & -1 \\ 1 & 1 \end{pmatrix}E_2 + \begin{pmatrix} 1 & 1 \\ 1 & 1 \end{pmatrix}E_1\right]; \quad (A1.16)$$

$$O_2 = \frac{1}{4}\begin{pmatrix} 0 & 1 \\ 0 & 1 \end{pmatrix}\begin{pmatrix} 1 & 1 \\ -i & -i \end{pmatrix}E_C + \frac{1}{4}\begin{pmatrix} -1 & 0 \\ -1 & 0 \end{pmatrix}\left[\begin{pmatrix} -1 & -1 \\ 1 & 1 \end{pmatrix}E_2 + \begin{pmatrix} 1 & 1 \\ 1 & 1 \end{pmatrix}E_1\right]; \quad (A1.17)$$

$$O_3 = \frac{1}{4}\begin{pmatrix} -1 & 0 \\ 1 & 0 \end{pmatrix}\begin{pmatrix} 1 & 1 \\ -i & -i \end{pmatrix}E_C + \frac{1}{4}\begin{pmatrix} 0 & -1 \\ 0 & 1 \end{pmatrix}\left[\begin{pmatrix} -1 & -1 \\ 1 & 1 \end{pmatrix}E_2 + \begin{pmatrix} 1 & 1 \\ 1 & 1 \end{pmatrix}E_1\right]; \quad (A1.18)$$

$$O_4 = \frac{1}{4}\begin{pmatrix} 1 & 0 \\ -1 & 0 \end{pmatrix}\begin{pmatrix} 1 & 1 \\ -i & -i \end{pmatrix}E_C + \frac{1}{4}\begin{pmatrix} 0 & -1 \\ 0 & 1 \end{pmatrix}\left[\begin{pmatrix} -1 & -1 \\ 1 & 1 \end{pmatrix}E_2 + \begin{pmatrix} 1 & 1 \\ 1 & 1 \end{pmatrix}E_1\right], \quad (A1.19)$$

which when simplified further yield

$$O_1 = \frac{1}{4}\begin{pmatrix} -i & -i \\ -i & -i \end{pmatrix}E_C + \frac{1}{4}\begin{pmatrix} -1 & -1 \\ -1 & -1 \end{pmatrix}E_2 + \frac{1}{4}\begin{pmatrix} 1 & 1 \\ 1 & 1 \end{pmatrix}E_1; \quad (A1.20)$$

$$O_2 = \frac{1}{4}\begin{pmatrix} -i & -i \\ -i & -i \end{pmatrix}E_C + \frac{1}{4}\begin{pmatrix} 1 & 1 \\ 1 & 1 \end{pmatrix}E_2 + \frac{1}{4}\begin{pmatrix} -1 & -1 \\ -1 & -1 \end{pmatrix}E_1; \quad (A1.21)$$

$$O_3 = \frac{1}{4}\begin{pmatrix} -1 & -1 \\ 1 & 1 \end{pmatrix}E_C + \frac{1}{4}\begin{pmatrix} -1 & -1 \\ 1 & 1 \end{pmatrix}E_2 + \frac{1}{4}\begin{pmatrix} -1 & -1 \\ 1 & 1 \end{pmatrix}E_1; \quad (A1.22)$$

$$O_4 = \frac{1}{4}\begin{pmatrix} 1 & 1 \\ -1 & -1 \end{pmatrix}E_C + \frac{1}{4}\begin{pmatrix} -1 & -1 \\ 1 & 1 \end{pmatrix}E_2 + \frac{1}{4}\begin{pmatrix} -1 & -1 \\ 1 & 1 \end{pmatrix}E_1. \quad (A1.23)$$

These equations can now be simplified to provide the four equations

$$O_1 = \frac{1}{4}\begin{pmatrix} 1 & 1 \\ 1 & 1 \end{pmatrix}[E_1 - E_2 - iE_C]; \quad (3.22)$$

$$O_2 = \frac{1}{4}\begin{pmatrix} 1 & 1 \\ 1 & 1 \end{pmatrix}[E_2 - E_1 - iE_C]; \quad (3.23)$$

$$O_3 = \frac{1}{4}\begin{pmatrix} -1 & -1 \\ 1 & 1 \end{pmatrix}[E_1 + E_2 + E_C]; \quad (3.24)$$

$$O_4 = \frac{1}{4}\begin{pmatrix} -1 & -1 \\ 1 & 1 \end{pmatrix}[E_1 + E_2 - E_C]. \quad (3.25)$$

A1.3 Proof from equations (3.38-41) to (3.42-43)

In Chapter 3, after we had substituted expressions for the fields into the above equations, and squared the results to obtain the powers, we were left with the following equations:

$$P_1 = \frac{P_0}{4r^2}\exp\left\{-2\left(\frac{\varphi}{\theta_0}\right)^2\right\}\left[3 + 2\sin\Theta_1 - 2\sin\Theta_2 - 2\cos\Theta_1\cos\Theta_2 - 2\sin\Theta_1\sin\Theta_2\right]; \quad (3.38)$$

$$P_2 = \frac{P_0}{4r^2}\exp\left\{-2\left(\frac{\varphi}{\theta_0}\right)^2\right\}\left[3 - 2\sin\Theta_1 + 2\sin\Theta_2 - 2\cos\Theta_1\cos\Theta_2 - 2\sin\Theta_1\sin\Theta_2\right]; \quad (3.39)$$

$$P_3 = \frac{P_0}{4r^2}\exp\left\{-2\left(\frac{\varphi}{\theta_0}\right)^2\right\}\left[3 + 2\cos\Theta_1 + 2\cos\Theta_2 + 2\cos\Theta_1\cos\Theta_2 + 2\sin\Theta_1\sin\Theta_2\right]; \quad (3.40)$$

$$P_4 = \frac{P_0}{4r^2}\exp\left\{-2\left(\frac{\varphi}{\theta_0}\right)^2\right\}\left[3 - 2\cos\Theta_1 - 2\cos\Theta_2 + 2\cos\Theta_1\cos\Theta_2 + 2\sin\Theta_1\sin\Theta_2\right]. \quad (3.41)$$

In order to be able to use these equations for calculating range and bearing, we need them in the form $\Theta_{1,2} = f(P_1, P_2, P_3, P_4)$. As a starting point, we can use a pair of equations that have been used in the past [LESU96] as range and bearing indicators

$$\rho = \frac{\sqrt{(P_1 - P_2)^2 + (P_3 - P_4)^2}}{(P_1 + P_2 + P_3 + P_4)}; \quad (A1.24)$$

$$\phi = \left(\frac{P_1 - P_2}{P_3 - P_4}\right). \quad (A1.25)$$

Taking the bearing indicator first, and substituting the equations (3.38) to (3.41) for the power values, we obtain

$$\phi = \frac{4\sin\Theta_1 - 4\sin\Theta_2}{4\cos\Theta_1 + 4\cos\Theta_2};$$

$$= \frac{\sin(A + B) - \sin(A - B)}{\cos(A + B) + \cos(A - B)}, \quad (A1.26)$$

where $A = \frac{1}{2}(\Theta_1 + \Theta_2)$ and $B = \frac{1}{2}(\Theta_1 - \Theta_2)$. Simplifying, we obtain

$$\begin{aligned} \phi &= \frac{\cos A \sin B}{\cos A \cos B}; \\ &= \tan B. \end{aligned} \tag{A1.27}$$

Substituting back for ϕ and B, we obtain equation (3.43)

$$\Theta_2 - \Theta_1 = 2 \tan^{-1}\left(\frac{P_1 - P_2}{P_3 - P_4}\right). \tag{3.43}$$

We now take a similar approach using equation (A1.24). Substituting in the power values yields

$$\rho = \frac{\sqrt{(4 \sin\Theta_1 - 4 \sin\Theta_2)^2 + (4 \cos\Theta_1 + 4 \cos\Theta_2)^2}}{12}, \tag{A1.28}$$

which on expanding the terms in the square root becomes

$$\begin{aligned} \rho &= \frac{\sqrt{2(1 - \sin\Theta_1 \sin\Theta_2 + \cos\Theta_1 \cos\Theta_2)}}{3}; \\ &= \frac{\sqrt{2(1 + \cos(\Theta_1 + \Theta_2))}}{3}; \\ &= \frac{\sqrt{4 \cos^2 \frac{1}{2}(\Theta_1 + \Theta_2)}}{3}; \\ &= \frac{2}{3} \cos \frac{1}{2}(\Theta_1 + \Theta_2). \end{aligned}$$

Substituting for ρ and rearranging, we obtain equation (3.42)

$$\Theta_1 + \Theta_2 = 2 \cos^{-1}\left(\frac{3\sqrt{(P_1 - P_2)^2 + (P_3 - P_4)^2}}{2(P_1 + P_2 + P_3 + P_4)}\right). \tag{3.42}$$

Appendix 2
Program Code

This appendix contains code for the !Rangefind application described in Chapter 4, and also code for the filter and modified data capture programs mentioned in Chapter 9.

A2.1 The !Rangefind application

The !Rangefind program was written as proper RiscOS application. The following sections show the various files included in the application. They were all compiled using Make to link them together.

A2.1.1 Header file **program.h**

```
/*
//  Program header for the RangeFind 'main' program
*/

#include <stdio.h>
#include <stdlib.h>
#include <math.h>
#include <assert.h>
#include "IIADCLib.h" /* Contains the routines for using the ADC card *
/
#include "PLOTlib.h"  /* Contains routines written by J.C.G. Lesurf
                         for plotting to the screen */
#include "wimp.h"
#include "kernel.h"
#include "swis.h"
```

```
#define NO_CHANNELS 4
#define NO_SAMPLES_PER_CHANNEL 16384
#define PI 3.141592654
#define CARD 0
#define SAMPLE_RATE_INDEX
#define mod_frequency 7812.5        /* PIN switch modulation frequency *
/
#define sample_length 23.993762E-6 /* Length of ADC card sample */
#define X 0.19799
#define lambda 0.2997/95.0          /* Wavelength */


void make_psd_tables(double *, double *, int);
double psd(double *, double *, double *);
void display(double *, double, double, double, double *, double,
double, double);
void get_data(double *, double *, double *, double *);
void get_powers(double *, double *);
void get_r_and_phi(double *, double *, double *, double);
void introduction(double *, int *);
```

A2.1.2 Main program file **main.c**

```
/*
//  Main program for ranging.  Calls various functions to take in
//  voltages from  ADC card, perform psd, calculate the range and
//  bearing, and display and save the results
*/


#include "program.h"

int main(void)
{
  double channel_1[NO_SAMPLES_PER_CHANNEL];
  double channel_2[NO_SAMPLES_PER_CHANNEL];
  double channel_3[NO_SAMPLES_PER_CHANNEL];
```

```
  double channel_4[NO_SAMPLES_PER_CHANNEL];
  double sine[NO_SAMPLES_PER_CHANNEL];      /* psd tables */
  double cosine[NO_SAMPLES_PER_CHANNEL];
  double psd_channel_[NO_CHANNELS+1];
  double if_power_[NO_CHANNELS+1];
  double r;
  double phi;
  double power_tot;
  int i;
  double offset;
  int no_of_trials;
  FILE *ofp;

  ofp = fopen("RAM::RamDisc0.$.TestFile","wt");
  fclose(ofp);

  introduction(&offset, &no_of_trials);
  make_psd_tables(sine, cosine);  /* make psd tables */

  for (i = 0; i < no_of_trials; ++i){

    get_data(channel_1, channel_2, channel_3, channel_4);


    /* calculate first set of powers and range and bearing */
    psd_channel_[1] = psd(channel_1, sine, cosine);
    psd_channel_[2] = psd(channel_2, sine, cosine);
    psd_channel_[3] = psd(channel_3, sine, cosine);
    psd_channel_[4] = psd(channel_4, sine, cosine);

    get_powers(psd_channel_, if_power_);
    get_r_and_phi(if_power_, &r, &phi, offset);
    power_tot = if_power_[1]+if_power_[2]+if_power_[3]+if_power_[4];
    ofp = fopen("RAM::RamDisc0.$.TestFile","at");
    fprintf(ofp, "%lf,%lf,%lf,%lf,%lf,%lf,%lf,%lf\n", offset,
      if_power_[1], if_power_[2], if_power_[3], if_power_[4],
power_tot, r, phi);
    fclose(ofp);
```

```
    display(if_power_, power_tot, r, phi);
  }

  return 0;
}
```

A2.1.3 Introduction routine `introduction.c`

```
/*
// This routine reads data files, and takes information from the user
/*

#include "program.h"

void introduction(double *offset, int *no_of_trials)
{
  char inputstr[10];
  FILE *fp;
  if (fopen("<obey$dir>.offset", "rt")==0){
    fp = fopen("<obey$dir>.offset", "wt");
    fprintf(fp, "%lf", 0.0);
    fclose(fp);
  }
  fp = fopen("<obey$dir>.offset", "rt");
  fscanf(fp, "%lf", offset);
  fclose(fp);

  printf("Welcome to the RangeFind program\n");
  printf("Enter data:\n");
  printf("Offset = (%lf)", *offset);
  gets(inputstr);
  if (inputstr != "\0")
    *offset = atof(inputstr);
  fp = fopen("<obey$dir>.offset", "wt");
  fprintf(fp, "%lf", 0.0);
  printf("Number of trials = ");
  scanf("%d", no_of_trials);
```

```
  fclose(fp);

}
```

A2.1.4 Data acquisition routine `get_data.c`

```
/*
//  Data acquisition function for the RangeFind 'main' program
*/

#include "program.h"


void get_data(double *channel_1, double *channel_2, double *channel_3,
double *channel_4)
{
  int i;
  double bits_to_volts = 10.0/4096.0;  /* conversion factor for raw
data */
  int buffer[NO_CHANNELS * NO_SAMPLES_PER_CHANNEL];


  IIADC_OneShotConfigConvert(CARD, SAMPLE_RATE_INDEX, NO_CHANNELS,
buffer, NO_SAMPLES_PER_CHANNEL);

  for (i = 0; i < NO_SAMPLES_PER_CHANNEL; ++i){
    channel_1[i] = buffer[4*i + 0] * bits_to_volts;
    channel_2[i] = buffer[4*i + 1] * bits_to_volts;
    channel_3[i] = buffer[4*i + 2] * bits_to_volts;
    channel_4[i] = buffer[4*i + 3] * bits_to_volts;
  }
}
```

A2.1.5 PSD routines in `psd.c`

```
/*
//  psd functions for the RangeFind 'main' program
*/
```

```
#include "program.h"

void make_psd_tables(double *sine, double *cosine)
{
  int i;
  double phase = 0.0;
  double mod_frequency;

  for (i = 0; i <= NO_SAMPLES_PER_CHANNEL; ++i){
    phase += 2*PI*mod_frequency*sample_length;
    sine[i] = sin(phase);
    cosine[i] = cos(phase);
  }
}


double psd(double *channel, double *sine, double *cosine)
{
  int i;
  double sine_ave = 0.0, cosine_ave = 0.0;


  for (i = 1; i <= NO_SAMPLES_PER_CHANNEL; ++i){
    sine_ave += (sine[i - 1]*channel[i - 1] - sine_ave) / i;
    cosine_ave += (cosine[i - 1]*channel[i - 1] - cosine_ave) / i;
  }
  assert(sine_ave != 0.0 && cosine_ave != 0.0);

  return sqrt(pow(sine_ave, 2) + pow(cosine_ave, 2));
}
```

A2.1.6 Calculation of powers `get_powers.c`

```
/*
//  function to calculate powers from raw psd voltage values
*/

#include "program.h"


#define a  1.150E-5      /* coefficients, obtained from crystal  */
#define b  2.466E-2      /* curves, used in program to calculate */
#define c  0.1311        /* powers from voltages                 */

double gain[4] = {1.0, 0.9387, 1.0149, 1.0732};
                         /* experimentally obtained relative gains */

void get_powers(double psd_channel_[], double if_power_[])
{
  int i;
  for (i = 1; i <= NO_CHANNELS; ++i)
    psd_channel_[i] = gain[i-1] * psd_channel_[i];
    if_power_[i] = a*pow(psd_channel_[i], 2) + b*psd_channel_[i] + c;
}
```

A2.1.7 Range and bearing calculation `get_r_phi.c`

```
/*
//  Function to calculate range and bearing from power values
*/

#include "program.h"

#define  radians_to_minutes  21600.0/(2*PI)


void get_r_and_phi(double p[], double *r, double *phi, double offset)
{
  double phase1, phase2;
```

```
  double sum, difference;
  double lambda_bar = lambda/(2*PI);


  /*make sure all power values are positive*/
  assert(p[1] > 0.0 && p[2] > 0.0 && p[3] > 0.0 && p[4] > 0.0);

  /* calculate sum and difference */
  sum = acos((1.5*sqrt(pow((p[1]-p[2]),2) + pow((p[3]-p[4]),2)))/(p[1]+
p[2]+p[3]+p[4]));
  difference = atan2((p[1]-p[2]),(p[3]-p[4]));


  /* calculate phases, introducing the offset (set in program.h) */
  phase1 = sum + difference;
  phase2 = sum - difference;


  /* calculate range r and bearing phi */
  *r = (2*X*X - pow(lambda_bar, 2)*(pow(phase1, 2) + pow(phase2, 2)))/
(2*lambda_bar*(phase1 + phase2));
  *phi = (asin((lambda_bar*phase2*(X*X - pow(lambda_bar, 2)*pow(phase1,
2)) - lambda_bar*phase1*(X*X - pow(lambda_bar, 2)*pow(phase2, 2)))/(X*
(2*X*X - pow(lambda_bar, 2)*(pow(phase1, 2) + pow(phase2, 2))))))*
radians_to_minutes;


  /* make sure that r and phi have reasonable values before they are
     passed back to main*/
  assert(*r > 0.0 && *r < 10000.0);
  assert(*phi > -100.0 && *phi < 100.0);
}
```

A2.1.8 Displaying the results `display.c`

```
/*
//  Prints results to screen
*/

#include "program.h"

void display(double if_power_[], double power_tot, double r, double
phi)
{
  char trial_number_str[64];
  char variable_str[16];

  int height = 20;
  int width = 10;

  plot_set_window_limits(0,0,1400,1400);  /* define graphics window
area */
  plot_clear_window(0);  /* sets background colour and clears to this
colour */
  plot_choose_font("Corpus.Medium\0",height/2,width);
  sprintf(trial_number_str, "Trial number %d\0", count);
  /* print out transmitter data */
  plot_fancy_print(width*5,height*15,trial_number_str);
  plot_fancy_print(width*5,height*13,"First transmitter");
  plot_fancy_print(width*5,height*12,"-----------------");
  plot_fancy_print(width*5,height*11,"     p1     p2     p3     p4
total   range  bearing");
  plot_fancy_print(width*5,height*10,"     --     --     --     --  ---
--   -----  -------");
  sprintf(variable_str, "%7.2lf\0", if_power1_[1]);
  plot_fancy_print(width*5,height*9,variable_str);
  sprintf(variable_str, "%7.2lf\0", if_power1_[2]);
  plot_fancy_print(width*(5+10.5),height*9,variable_str);
  sprintf(variable_str, "%7.2lf\0", if_power1_[3]);
  plot_fancy_print(width*(5+18),height*9,variable_str);
  sprintf(variable_str, "%7.2lf\0", if_power1_[4]);
  plot_fancy_print(width*(5+27),height*9,variable_str);
```

```
  sprintf(variable_str, "%7.2lf\0", power_totl);
  plot_fancy_print(width*(5+36),height*9,variable_str);
  sprintf(variable_str, "%8.2lf\0", rl);
  plot_fancy_print(width*(5+46),height*9,variable_str);
  sprintf(variable_str, "%9.4lf\0", phil);
  plot_fancy_print(width*(5+57),height*9,variable_str);
}
```

A2.2 A filter program

THIS PROGRAM, described briefly in Chapter 9, is a digital filter with a cutoff frequency of 100Hz, which was used to perform a PSD on raw data sampled at about 21000Hz and save it as low frequency data.

A2.2.1 The program

```
#include <stdio.h>
#include <math.h>
#include <string.h>

#define no_channels 4
#define no_samples_per_channel 81920
#define max 1000
#define x 64
#define sample_length 47.983908E-6
#define bits_to_mV 10000.0/4096.0
#define mod_freq 7812.5
#define band 100
#define pi 3.141592654

int main(void)
{
  /* variables */
  double imag, real;
  double imag_ = 0.0, real_ = 0.0;
  double vin;
```

```
double a, b;
int i, j;
int mem_ptr[4];
double phase;
double phi;
double amp;
char outfile[32];
char channel[4];

FILE *ifp, *ofp;

/* calculate filter constants a and b */
a = 1.0/exp(2*pi*band*sample_length);
b = 1.0 - a;

/* open data file */
ifp = fopen("Ranging.16th_march.file", "rb");


/* start filtering process for each channel */
for (j = 3; j < 4; ++j){
  /* reset variables */
  imag_ = 0.0;
  real_ = 0.0;
  /* open output file */
  sprintf(outfile, "Ranging.16th_march.processed");
  sprintf(channel, "%d", j+1);
  strcat(outfile, channel);
  ofp = fopen(outfile, "wt");
  for (i = 0; i <= no_samples_per_channel*max; ++i){
    /* take average of first x points */
    while (i < x){
      /* read file */
      fread(mem_ptr, sizeof(int), no_channels, ifp);
      vin = (double)mem_ptr[j] * bits_to_mV;
      /* generate psd phase */
      phi = 2*pi*mod_freq*sample_length*(double)i;
```

```
        /* get real and imaginary parts by multiplying by sine and cos
*/
        real = sin(phi)*vin;
        imag = cos(phi)*vin;
        ++i;
        imag_ += (imag - imag_) / (double)i;
        real_ += (real - real_) / (double)i;
      }
      /* generate psd phase */
      phi = 2*pi*mod_freq*sample_length*(double)i;
      /* read file */
      fread(mem_ptr, sizeof(int), no_channels, ifp);
      vin = (double)mem_ptr[j] * bits_to_mV;
      /* get real and imaginary parts by multiplying by sine and cos */
      real = sin(phi)*vin;
      imag = cos(phi)*vin;
      /* apply first order filter */
      imag_ = a*imag_ + b*imag;
      real_ = a*real_ + b*real;

      /* print out every 100th point */
      if(i % 100 == 0){
        /* calculate amplitude */
        amp = sqrt(real_*real_ + imag_*imag_);
        /* calculate phase */
        phase = atan2(imag_, real_);
        /* print to file */
        fprintf(ofp, "%lf,%lf\n", amp,phase);
      }
    }
    /* close output file */
    fclose(ofp);
  }
  /* close data file */
  fclose(ifp);

  return 0;
}
```

A2.3 Modified data capture program

THIS IS the code for the data capture program described in Chapter 9. It continuously streams data from the card into main memory, from where it is saved to disk as a CSV file.

A2.3.1 The program

```
#include <stdio.h>
#include <string.h>
#include <stdlib.h>
#include <math.h>
#include <time.h>
#include "IIADCLib.h"

#define card 0
#define no_channels 8
#define no_samples_per_channel 1024 /* x4 for no. of bytes */
#define sample_rate_index 7 /* 1665Hz or 208.13Hz per channel */
#define max 1500 /* total number of iterations (1463? per hour) */

int main(void)
{
  int buf_ptr, buf_flag, error_byte_cnt, convert_flag;
  int buffer[no_samples_per_channel*no_channels];
                /* buffer for captured data to be fed into */
  int *mem_ptr;
  int i, j, k;
  double I, Q;
  char outfile[64]={0};
  int data_capture_start_time, data_capture_stop_time;
  double time_for_capture;
  FILE *ofp;

  sprintf(outfile, "ADFS::HardDisc4.$.Ranging.Big_Data_Run.File\0");
```

```
  /* set up card */
  IIADC_ContinuousConfig(card, sample_rate_index, no_channels, buffer,
no_samples_per_channel);

  /* open large file */
  ofp = fopen(outfile, "wt");

  /* start acquisition */
  printf("Starting data capture...\n(This may take some time...)\n");
  IIADC_ConvertStart(card, 0, 0);
  data_capture_start_time = clock();

  for (i = 0; i < max; ++i){
    /* initialise mem_ptr */
    mem_ptr = buffer;
    /* check if first half of the buffer is still being filled */
    do{
      IIADC_ConvertStatus(card, &buf_ptr, &buf_flag, &error_byte_cnt, &
convert_flag);
      if (error_byte_cnt != 0) printf("Error!\n");
    } while (buf_flag == 0);

    /* save first half of buffer to file */
    for (j = 0; j < no_samples_per_channel/2; ++j){
      for (k = 0; k < no_channels/2; ++k){
        I = *mem_ptr;
        Q = *(mem_ptr + 4);
        fprintf(ofp, "%lf,%lf,", I, Q);
        mem_ptr += 1;
      }
      fprintf(ofp, "\n");
      mem_ptr += 4;
    }

    /* check if second half of the buffer is still being filled */
    do {
      IIADC_ConvertStatus(card, &buf_ptr, &buf_flag, &error_byte_cnt, &
convert_flag);
```

```
      if (error_byte_cnt != 0) printf("Error!\n");
    } while (buf_flag == 1);

    /* save second half of buffer to file */
    for (j = 0; j < no_samples_per_channel/2; ++j){
      for (k = 0; k < no_channels/2; ++k){
        I = *mem_ptr;
        Q = *(mem_ptr + 4);
        fprintf(ofp, "%lf,%lf,", I, Q);
        mem_ptr += 1;
      }
      fprintf(ofp, "\n");
      mem_ptr += 4;
    }
    printf("Done %d...\n", i);
  }

  /* stop data capture */
  IIADC_ConvertStop(card);
  data_capture_stop_time = clock();
  time_for_capture = (double)(data_capture_stop_time-
data_capture_start_time)/CLK_TCK;
  printf("Finished data capture\n");
  printf("data capture took %.2lf seconds\n", time_for_capture);

  /* close large file */
  fclose(ofp);

  return 0;
}
```

References

[ALTS84] Altshuler, E.E., "A Simple Expression for Estimating Attenuation by Fog at Millimeter Wavelength," *IEEE Trans. Ant. & Prop.* **AP-32** (7), Jul. 1984, pp. 757-8.

[BARO82] Baron, A.R. et al, "Passive Direction Finding and Signal Location," *Microwave Journal*, **25** (9), Sep. 1982, p. 59.

[BEAN68] Bean, B.R. and Dutton, E.J., *Radio Meteorology*, Dover Books, 1968.

[BOHL85] Bohlander, R.A. and McMillan, R.W., "Atmospheric Effects on Near-Millimeter-Wave Propagation," *Proc. IEEE*, **73** (1), Jan. 1985, pp. 49-60.

[BOHL88] Bohlander, R.A. et al, "Fluctuations in Millimeter Wave Signals Propagated Through Inclement Weather," *IEEE Trans. Geosciences and Remote Sensing*, **26** (3), May 1988, pp. 343-354.

[BRUS95] Brussaard, G. & Watson, P. A., *Atmospheric Modelling and Millimetre Wave Propagation*, Chapman & Hall, 1995.

[CARL85] Carlström, J.E. et al, "A Continuously Tunable 65-115GHz Gunn Oscillator," *IEEE Trans. Microwave Theory & Techniques*, **MTT-33** (7), Jul. 1985, pp. 610-619.

[DENN97] Dennis, I.R.H., *Passive Ranging of Near-Field Targets in the Audio Frequency Range*, Ph.D. Thesis, St. Andrews, Sep. 1997.

[EVAN01] Evans, M., Pryde, D.M. & Lesurf, J.C.G., "Development of a 3-Port Spatial Interferometer for Studying Tropospheric Refractive Index Fluctuations at Millimetre Wave Frequencies", *CLIMPARA 2001*, May 2001.

[GOLD98] Goldsmith, P.F., *Quasi-optical systems*, IEEE Press, 1998.

[HANB74] Hanbury Brown, R., *The Intensity Interferometer*, Taylor & Francis Ltd, 1974.

[HARV90] Harvey, A.R., *A Millimetre Wave Quasi-Optical Complex Impedance Bridge*, Ph.D. Thesis, St. Andrews, Jul. 1990.

[HAYD83] Haydl, W.H., "Fundamental and Harmonic Operation of

Millimeter-Wave Gunn Diodes," *IEEE Trans. Microwave Theory & Techniques*, **MTT-31** (11), Nov. 1983, pp. 879-889.

[HILL88] Hill, R.J. et al, "Turbulence-Induced Millimeter-Wave Scintillation Compared with Micrometeorological Measurements," *IEEE Trans. Geosciences and Remote Sensing*, **26** (3), May 1988, pp. 330-342.

[HORO89] Horowitz, P. & Hill, W., *The Art of Electronics*, Cambridge, 1989.

[JENK91] Jenkins, H.H., *Small-Aperture Radio Direction-Finding*, Artech House, 1991.

[KASU86] Kasuga, T. & Isiguro, M., "Interferometric Measurement of Tropospheric Phase Fluctuations at 22GHz on Antenna Spacings of 27 to 540m," *IEEE Trans. Ant. & Prop.* **AP-34** (6), Jun. 1986, pp. 797-803.

[KOGE64] Kogelnik, H., "Coupling and conversion coefficient for optical modes," *Proc. Symp. Quasi-Optics.* New York: Polytechnic Institute of Brooklyn, 1964, pp 333-347.

[KONK92] Konkov, E.V. et al, "Investigations of the Near-Millimeter-Wave Propagation on Surface Boundary Layer Path," *Int. J. of Infrared & Millimeter Waves*, **13** (7), 1992, pp. 955-969.

[KRAU66] Kraus, J.D., *Radio Astronomy*, Cygnus-Quasar Books, 1966.

[LOCK89] Lockhart, G.B. & Cheetham, B.M.G., *BASIC Digital Signal Processing*, Butterworths 1989.

[LESU90] Lesurf, J.C.G., *Millimetre-wave Optics, Devices & Systems*, Adam Hilger, 1990.

[LESU94] Lesurf, J.C.G. & Robertson, M.R., "MM-Wave Spatial Interferometry as an Alternative to Radar for Coherent Point Sources", *Int. J. of Infrared & Millimeter Waves*, **15** (11), 1994, pp. 1829-1840.

[LESU95] Lesurf, J.C.G., *Information and Measurement*, IOP Publishing, 1995.

[LESU96] Lesurf, J.C.G., *Ranging Concept Model 1*, Report to DERA R030, 1996.

[LESU97a] Lesurf, J.C.G. & Robertson, D.A., *Ranging Concept Model 2*, Report to DERA R034, 1997.

[LESU97b] Lesurf, J.C.G. & Robertson, D.A., *Final Report on Passive Ranging*, Report to DERA R037, 1997.

[LIEB89] Liebe, H.J., "MPM - An Atmospheric Millimeter-Wave Propagation Model," *Int. J. of Infrared & Millimeter Waves*, **10** (6), 1989, pp. 631-650.

[LIPS87] Lipsky, S.E., *Microwave Passive Direction Finding*, Wiley, 1987.

[MA98] Ma, H. et al, "The Performances of the Antennas in Active/ Passive Compound Guidance. Part 1: Broad-Band Antennas and Direction-Finding Schemes" *Int. J. of Infrared & Millimeter Waves*, **19** (1), 1998, pp. 107-117.

[McMIL97] McMillan, R.W. et al, "Millimeter-Wave Atmospheric Turbulence Measurements: Instrumentation, Selected Results and System Effects," *Int. J. of Infrared & Millimeter Waves*, **18** (1), 1997, pp. 233-258.

[MAY96] May, P.B., *Signal Processing Techniques for Broadband Millimetre Wave Systems*, First Year Report, St. Andrews, Sep. 1996.

[OLMI92] Olmi, L. & Downes, D., "Interferometric Measurement of Tropospheric Phase Fluctuations at 86GHz on ANtenna Spacings of 24m to 288m," *Astron. Astrophys.*, **262**, 1992, pp. 634-643.

[PRES88] Press, W.H. et al, *Numerical Recipes in C*, Cambridge 1988.

[PRYD98] Pryde, D.M. & Robertson, D.A., *Measurement of Loss on Foamex UPVC Panel Across W-Band*, Report to Q-Par Angus, Jan. 1998.

[RAMS85] Ramsay, D.A., "The Evolution of Radar Guidance," *G.E.C. Journal of Research*, **3** (2), 1985, pp. 92-103.

[REED87] Reedy, E.K., "Fundamentals of MMW Radar Systems," *Principles and Applications of Millimeter Wave Radar*, Editors: Currie, N.C. and Brown, C.E., Artech House, 1987.

[ROBE94a] Robertson, M.R. & Lesurf, J.C.G., "Range and Azimuth Measurements of a MM-Wave Coherent Point Source by Spatial Interferometry", *Int. J. of Infrared & Millimeter Waves*, **15** (11), 1994, pp. 1841-1850.

[ROBE94b] Robertson, D.A., *Millimetre Wave Quasi-Optical Signal Processing and Spread Spectrum Techniques*, Ph.D. Thesis, St. Andrews, Nov. 1994.

[SAUV92] Sauvageot, H., *Radar Meteorolgy*, Artech House, 1992.

[SKOL81] Skolnik, M.I., *Introduction to Radar Systems*, McGraw-Hill 1981.

[SMIT90] Smith, G.M., *Transferred Electron Oscillators at MM Wave Frequencies and their Characterisation using Quasi-Optical Techniques*, Ph.D. Thesis, St. Andrews, Mar. 1990.

[STRO68] Strohbehn, J.W., "Line-of-Sight Wave Propagation Though the Turbulent Atmosphere," *Proc. IEEE*, **56** (8), Aug. 1968,

pp. 1301-1318.

[THOM86] Thomson, A. R. et al, *Interferometry and Synthesis in Radio Astronomy*, Krieger, 1986.

[TREB87] Trebits, R.N., "MMW Propagation Phenomena," *Principles and Applications of Millimeter Wave Radar,* Editors: Currie, N.C. and Brown, C.E., Artech House, 1987.

[ULAB81] Ulaby, F.T., Moore, R.K. and Fung, A.K., *Microwave Remote Sensing Fundamentals and Radiometry*, Volume 1, Artech House, 1981.

[VANH90] Vanhoenacker, D. & Vander Vorst, A., "A Multipath Model for Atmospheric Scintillations at Microwaves and Millimeter Waves," *Int. J. of Infrared & Millimeter Waves*, **11** (4), 1990, pp. 519-532.

[VANH91] Vanhoenacker, D. et al, "Simulation of the Effects of Atmospheric Scintillation on Digital Transmission at Centimeter and Millimeter Wavelengths," *Int. J. of Infrared & Millimeter Waves*, **12** (10), 1991, pp. 1215-1224.

[VANV47a] Van Vleck, J.H., "The Absorption of Microwaves by Oxygen," *Phys. Rev.*, **71**, Apr. 1947, pp. 413-424.

[VANV47b] Van Vleck, J.H., "The Absorption of Microwaves by Uncondesed Water Vapour," *Phys. Rev.*, **71**, Apr. 1947, pp. 425-433.

[WELC77] Welch, W.J. et al, "An Interferometer for Millimeter Wavelengths", *Astron. Astrophys.*, **59**, 1977, pp. 379-385.

[WRIG96] Wright, M.C.H., "Atmospheric Phase Noise and Aperture Synthesis at Millimeter Wavelengths," *Publications of the Astronomical Society of the Pacific*, **108**, Jun. 1996, pp. 520-534.

[WYLD84] Wylde, R.J., "Millimetre-Wave Gaussian Beam-Mode Optics and Corrugated Feed Horns," *IEE Proc.*, **131-H** (4), Aug. 1984, pp. 258-262.